UNIVERSITAT DE BARCELONA

VIPPIX: A readout ASIC for the next generation of human brain PET scanners

José Gabriel Macías Montero

VIPPIX: A readout ASIC for the next generation of human brain PET scanners

Doctoral Thesis

José Gabriel Macías Montero

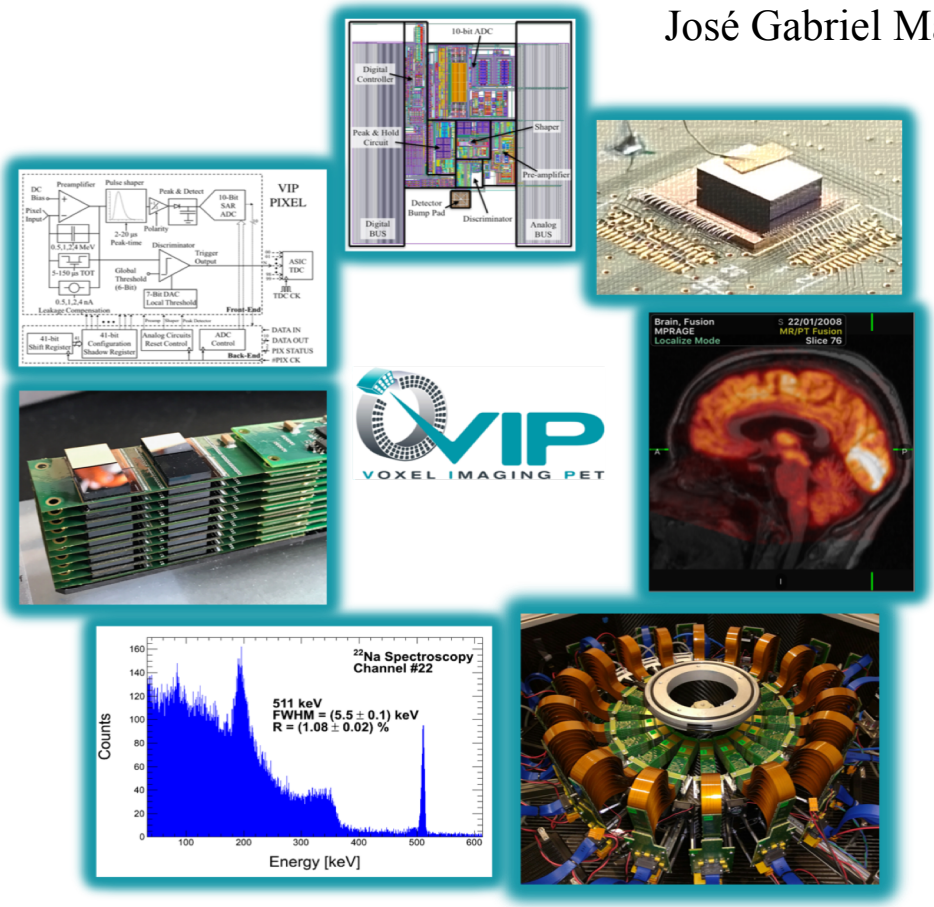

Supervisors

Mokhtar Chmeissani Raad

Ángel Diéguez Barrientos

UNIVERSITAT DE BARCELONA

VIPPIX: A readout ASIC for the next generation of human brain PET scanners

Memòria presentada per optar al grau de doctor per la

Universitat de Barcelona

Programa de doctorat en Enginyeria i Ciències Aplicades

Autor: José Gabriel Macías Montero

Director: Dr. Mokhtar Chmeissani Raad

Director i Tutor: Dr. Ángel Diéguez Barrientos

Institut de Física d'Altes Energies (IFAE)

Departament d'Enginyeria Electrònica i Biomèdica, Facultat de Física, Universitat de Barcelona

UNIVERSITAT DE BARCELONA

a mi família

Resumen

La tomografía por emisión de positrones (PET) es una técnica de imagen molecular usada en las últimas décadas en medicina nuclear. En combinación con resonancia magnética (MRI) o tomografía computarizada (CT) que proporcionan los coeficientes de atenuación del volumen escaneado, las cámaras PET proporcionan información fisiológica precisa del cuerpo humano, lo que es crucial en oncología, cardiología, y neuro-psiquiatría.

El diagrama de flujo para obtener una imagen PET se muestra en la Figura 1. Los radionucleidos que emiten positrones se producen en un ciclotrón y deben poseer una vida media relativamente corta para aplicaciones clínicas, como Flúor-18 con 110 minutos de vida media. Una vez generados los isótopos, estos se integran en trazadores del metabolismo biológico a través de un proceso de síntesis química. Para aplicaciones en oncología, se utiliza glucosa como trazador principal debido a la relación entre su consumo y el metabolismo de las células. La dosis prescrita que se inyecta al paciente mediante inyección intravenosa depende del tipo de examen y del tejido a escanear.

La toma de imágenes se inicia una vez la dosis inyectada se ha distribuido en el cuerpo del paciente de forma estacionaria. El consumo de glucosa libera el radionucleido y éste emite un positrón que se aniquila cuando interacciona con un electrón del entorno. Como resultado de la aniquilación, se emiten dos fotones en dirección opuesta de energía equivalente a la masa del electrón, 511 keV. La detección simultánea de ambos fotones en dos puntos del detector PET genera una trayectoria en la que está localizado el origen de la aniquilación. La adquisición y combinación de millones de trayectorias se usan en algoritmos de reconstrucción de imagen 3D para identificar los orígenes de cada aniquilación. La imagen PET se genera como mapa tridimensional de la concentración del consumo de glucosa que se normaliza con la densidad de los tejidos obtenidas con técnicas de resonancia magnética o tomografía computarizada en momentos inmediatamente anteriores o posteriores a la toma de imágenes con el escáner PET.

Debido al movimiento libre del positrón dentro del cuerpo y al momento cinético del electrón antes de la aniquilación, la mejor resolución espacial de la tomografía por emisión de positrones es de aproximadamente de 1 mm para cámaras PET de cerebro humano. Con dicha limitación, no es posible la detección precoz de tumores de tamaño inferior a 1 mm de diámetro. Desafortunadamente, el tamaño mínimo de detección de las mejores cámaras PET para cerebro humano está lejos de 1 mm de diámetro debido a limitaciones tecnológicas.

Idealmente, un escáner PET debería estar basado en detectores de radiación con sección eficaz infinita, es decir, densidad infinita para absorber todos los fotones de rayos gamma dentro del campo de visión (FOV). Además, los detectores deberían tener una resolución espectral excelente para descartar todos aquellos fotones que han desviado su trayectoria antes de alcanzar el detector y una resolución temporal suficiente para identificar de forma precisa el tiempo de impacto de los fotones procedentes de la misma aniquilación

y evitar el apilamiento de eventos y la consecuente pérdida de eficiencia. Finalmente, una resolución espacial precisa determinará exactamente la trayectoria de los dos fotones de cada aniquilación.

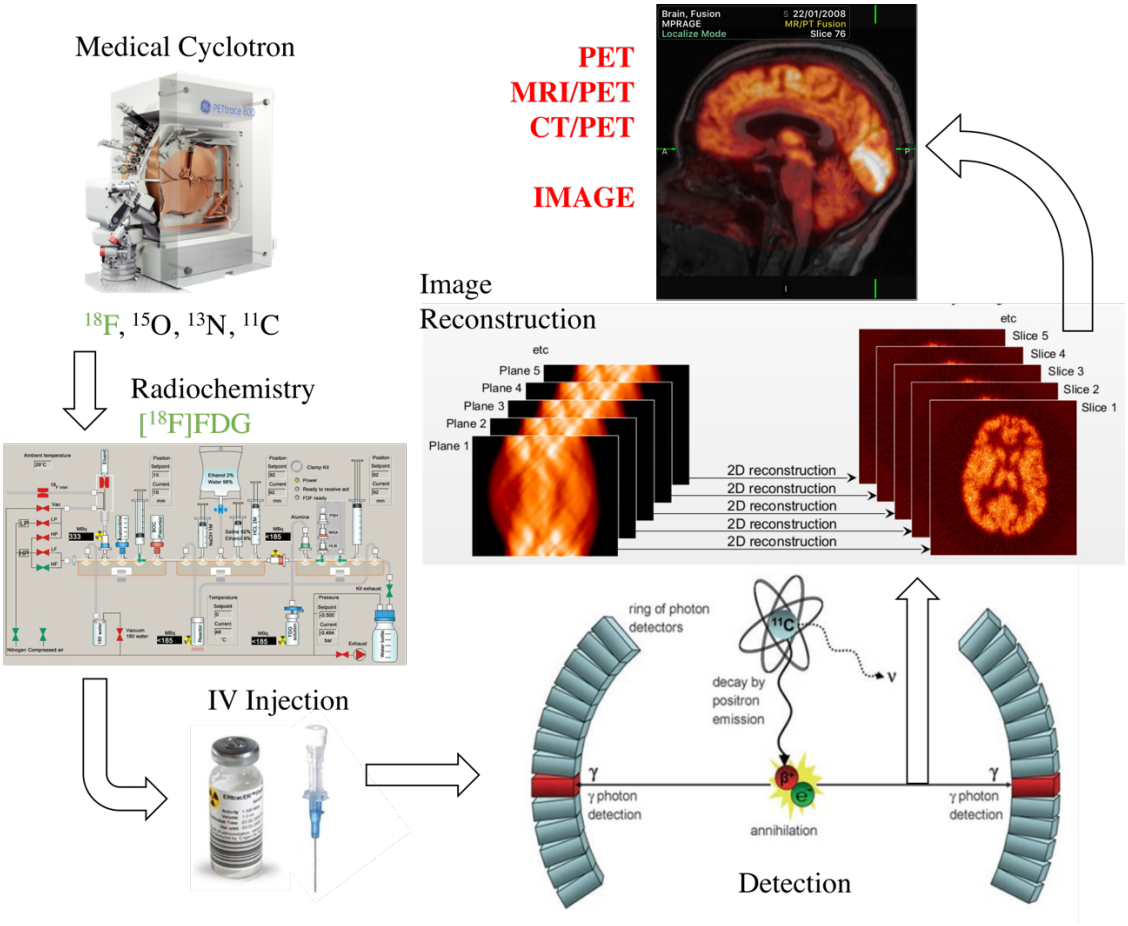

Figura 1. Diagrama de flujo para la realización de una tomografía por emisión de positrones.

En esta tesis, se presenta un circuito integrado de aplicación específica (ASIC) para leer la energía y el tiempo de impacto de un detector de estado solído pixelado de alta densidad para un nuevo diseño de escáner PET. La investigación presentada aquí se ha realizado en el marco del proyecto "*Voxel Imaging PET pathfinder*" del *European Research Council* (ERC). El propósito de la investigación era desarrollar un prototipo de módulo detector de rayos gamma de uso en aplicaciones de tomografía por emisión de positrones y alcanzar los límites físicos en términos de calidad y resolución de imagen, en un tiempo de escaneo mucho más corto que las cámaras PET comerciales actuales.

Este trabajo está dividido en varios capítulos que describen las actividades realizadas durante el proyecto y presentan sus resultados. Adicionalmente, se incluyen los cinco artículos publicados en revista más relevantes asociados a dichas actividades como la simulación de las prestaciones del nuevo diseño de escáner PET, la caracterización experimental de los detectores de estado sólido utilizados en el proyecto, el diseño de la electrónica de los píxeles y el diseño del ASIC completo, y finalmente la caracterización de

varios módulos detectores fabricados en términos de resolución espectral y precisión temporal.

La Figura 2 muestra la geometría del escáner PET del proyecto VIP. El nuevo diseño está compuesto de módulos detectores basados en el apilamiento de detectores híbridos de Telurio de Cadmio (CdTe) segmentados en 100 píxeles. Con esta geometría se consigue un volumen de CdTe segmentado en múltiples canales con electrónica de lectura independiente. El CdTe tiene un número atómico equivalente elevado lo que proporciona una sección eficaz elevada para los fotones de rayos gamma de 511 keV de energía. Con una longitud de detección de 4 cm, se espera que el 80% de los fotones que atraviesan el detector sean absorbidos.

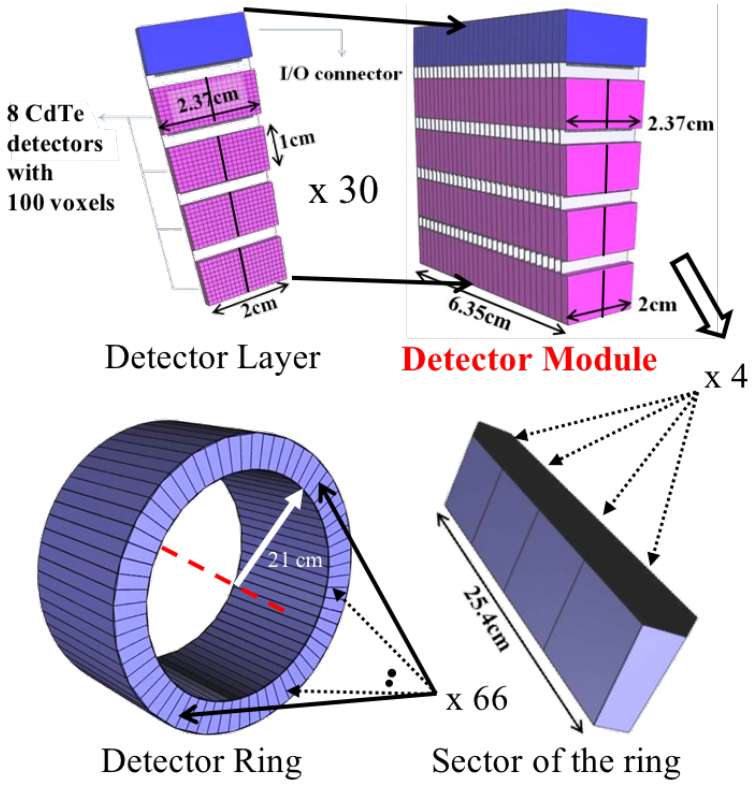

Figura 2. Descripción de la geometría del escáner PET VIP.

Cada detector tiene un grosor de 2 mm, está segmentado en una matriz de 10 x 10 píxeles de un tamaño de 1 mm x 1 mm, y está conectado a un ASIC de lectura con 100 canales. De esta forma, el volumen completo de detección del escáner PET está dividido en más de seis millones de píxeles con lectura independiente de la energía y el tiempo de impacto. Esta resolución espacial permitiría alcanzar el límite de tamaño de detección de la tomografía por emisión de positrones en el cerebro humano. Adicionalmente, una resolución espectral del 1-2 % FWHM de los detectores de Telurio de Cadmio permite descartar fotones desviados y el porcentaje de trayectorias correctas detectadas será muy elevado. Como consecuencia, la adquisición de pocos millones de trayectorias detectadas es suficiente para generar imágenes PET de calidad excelente.

A pesar de que la resolución temporal de detectores de Telurio de Cadmio no es suficiente para aplicaciones que requieren gran precisión como cámaras PET basadas en el tiempo de vuelo de los fotones, sí lo es para el escáner VIP PET ya que puede trabajar con dosis radioactivas muy inferiores lo que reduce enormemente las necesidades de resolución temporal en la identificación del tiempo de impacto de los fotones.

Las prestaciones del escáner VIP PET obtenidas con GAMOS, una arquitectura basada en GEANT-4 para simulaciones orientadas a la medicina, han sido publicadas y se exponen en este trabajo. En las simulaciones se ha utilizado la resolución espectral y temporal de detectores de CdTe comerciales de 2 mm de grosor. La fracción de dispersión del escáner PET obtenida es de un 4% con una resolución espectral de los detectores de CdTe de 1.6 % FWHM. Utilizando modelos estándar internacionales para la caracterización de cámaras PET de alta resolución se consigue una resolución espacial de 1 mm de diámetro con un set de datos de 10 a 20 millones de coincidencias detectadas. Estas prestaciones se consiguen con una actividad óptima de 32 MBq distribuidos en un volumen de 6 litros equivalente al cerebro humano adulto.

Como consecuencia de los excelentes resultados obtenidos, se ha publicado y presentado en esta tesis la comparación con escáneres PET de cuerpo completo y cerebro, así como, con escáneres de alta resolución para investigación. El escáner VIP PET presenta, para un tamaño de cerebro humano, la alta resolución de escáneres para animales pequeños. Esta mejora en la resolución puede ser de vital importancia para la investigación de enfermedades neuronales como el Alzheimer o el Parkinson, así como para la detección muy precoz de tumores cerebrales.

Todas las simulaciones mencionadas están basadas en las prestaciones experimentales de detectores de Telurio de Cadmio de 2 mm de grosor. Su caracterización con electrónica comercial de bajo ruido y gran ancho de banda para un único canal ha sido publicada en la revista *Journal of Instrumentation* y se detalla en esta memoria. La resolución espectral del pico a 511 keV y la resolución temporal de fotones en coincidencia han sido caracterizados con una fuente radioactiva de Sodio-22. Para interacciones fotoeléctricas, se obtiene una resolución espectral de 1.6 % FWHM y una resolución temporal de 6 ns FWHM manteniendo los detectores a -8 grados centígrados con tensión de polarización de -2000 V.

Una revisión de los ASICs más relevantes para la lectura de detectores de radiación disponibles en la literatura se ha presentado en este trabajo. Las tres aplicaciones principales son imagen 2D por medio de contaje de fotones, espectroscopia, y medición del tiempo de vuelo para detección de distancias. La aplicación VIP PET precisa de medidas simultáneas de la energía y del tiempo de impacto en cada píxel con excelente resolución. Así pues, el ASIC VIPPIX combina circuitería de las tres diferentes aplicaciones y es el primer circuito integrado de lectura capaz de leer de forma precisa la energía y el tiempo de interacción de cada detección.

El chip VIPPIX se describe en el capítulo 6 y en dos artículos publicados en la revista del *IEEE Transactions of Nuclear Science*. Su arquitectura se muestra en la Figura 3 y está basada en una matriz de 10 x 10 píxeles independientes conectados a un controlador digital global y un conversor digital del tiempo de impacto (TDC). La arquitectura del TDC está basada en un esquema de primera generación con un integrador de señal y un conversor analógico digital. El circuito proporciona la medida de la duración de un pulso temporal digital generado a partir de la activación del disparador de uno de los píxeles de la matriz y finalizado síncronamente con una señal de reloj de 10 MHz. De esta forma, se obtiene un rango dinámico de 100 ns y una precisión de 100 ps aproximadamente.

Las referencias de tensión y corriente, un sensor de temperatura, y un circuito de identificación se encuentran junto con el controlador digital y el TDC en la periferia del ASIC.

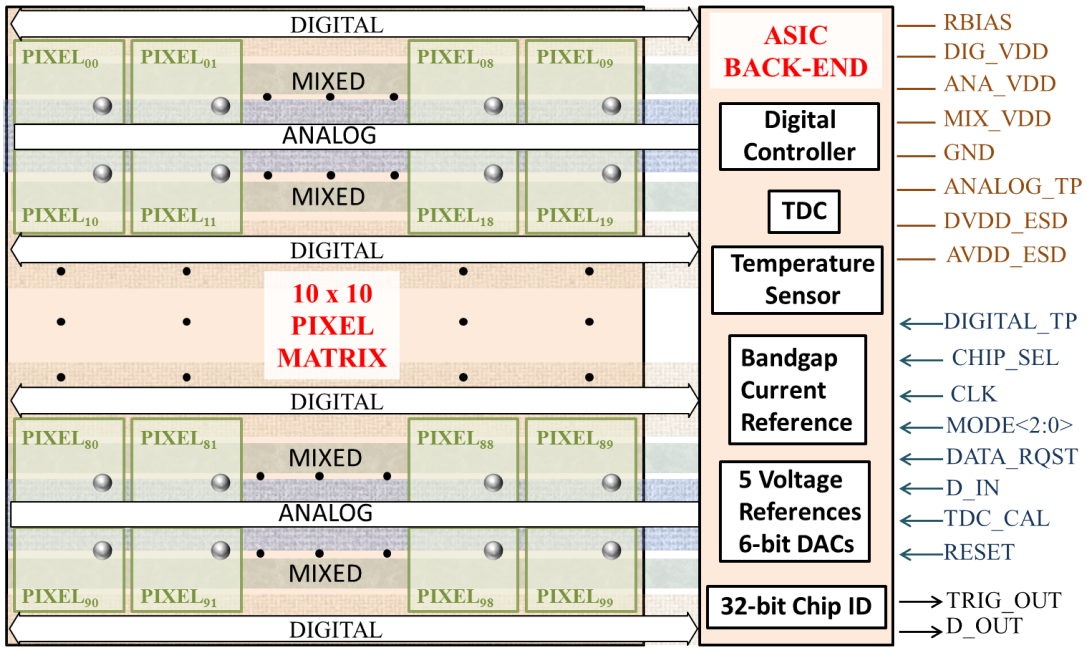

Figura 3. Diagrama de bloques del ASIC VIPPIX.

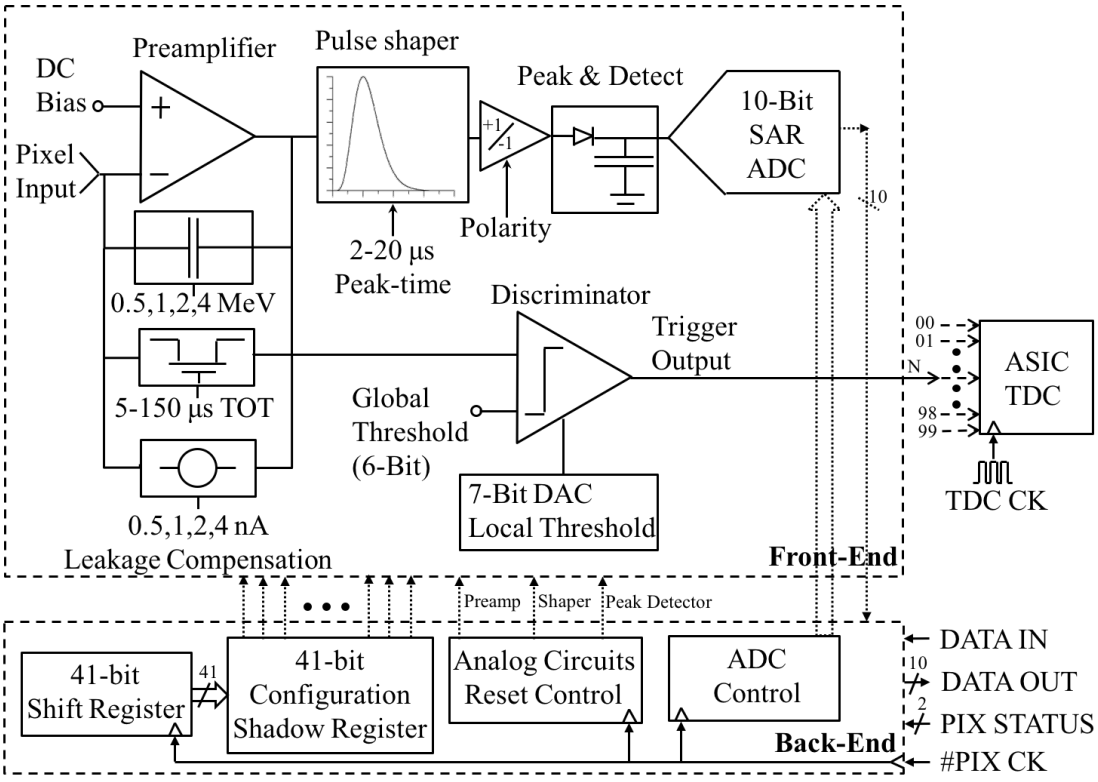

Figura 4. Diagrama de bloques de la electrónica del pixel del ASIC VIPPIX.

La arquitectura del pixel está ilustrada en la Figura 4. Cada píxel está compuesto por un preamplificador de ganancia programable con compensación dinámica de la corriente de fugas del detector, un circuito acondicionador del pulso para limitar el ancho de banda del ruido conectado a un detector de pico, un conversor analógico-digital (ADC) de 10 bits basado en una arquitectura de aproximaciones sucesivas, un comparador con compensación individual del offset, y un controlador digital local.

La arquitectura del sistema de control del ASIC está diseñada para que la señal de reloj necesaria para la conversión analógico-digital y la programación del registro de desplazamiento de 41 bits de los píxeles se realice individualmente y únicamente durante la adquisición de un evento y la programación del píxel respectivamente. De esta forma, se reducen las interferencias dentro de la matriz de píxeles y se puede trabajar con tensiones umbral limitadas únicamente por el nivel de ruido de salida del preamplificador.

Para obtener las mejores prestaciones de la electrónica conectada a los sensores de CdTe, la ecualización y la calibración con fuentes radioactivas deben realizarse en paralelo a todos los píxeles del escáner en condiciones de trabajo. Debido a que las prestaciones de los sensores basados en semiconductores varían enormemente con la temperatura y la tensión de polarización, los algoritmos de calibración y ecualización deben aplicarse cuando dichas condiciones cambien.

El diseño y la fabricación del ASIC VIPPIX se ha realizado en diferentes etapas. Primero la electrónica analógica más sensible y el ADC fueron fabricados y caracterizados de forma independiente. El ruido equivalente a la entrada de la electrónica del píxel es de 133 electrones RMS para ajustes de polaridad positiva del sensor, y 150 electrones RMS para ajustes de polaridad negativa. La dispersión temporal del tiempo de impacto es de aproximadamente 1 ns para deposiciones de energía mayores a 200 keV y la resolución temporal del TDC es de 600 ps FWHM.

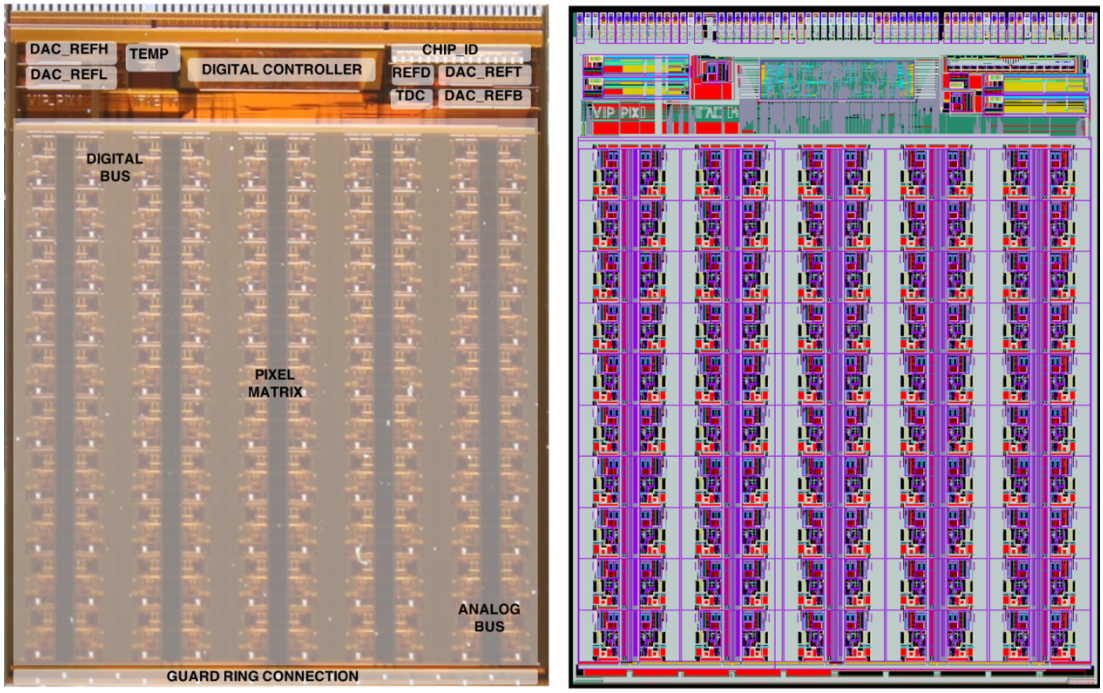

Figura 5. Fotografía ilustrada y layout del ASIC VIPPIX fabricado.

Para verificar el diseño de la matriz de píxeles una versión reducida con una matriz de 4 x 4 píxeles ha sido fabricada y caracterizada con un detector segmentado de igual forma previamente a la integración final del ASIC VIPPIX. La primera espectroscopia obtenida con un detector de CdTe polarizado a -1000 V conectado a un mini-ASIC VIPPIX a temperatura ambiente muestra una resolución espectral de 3.6 % FWHM para el pico de 122 keV del Cobalto-57.

La Figura 5 muestra una ilustración del layout y una fotografía del ASIC VIPPIX. Doce obleas con el diseño de VIPPIX se han fabricado, post-procesado, y caracterizado con sondas de testeo específicas. Los ASICs de mejor calidad se han montado en 720 detectores de Telurio de Cadmio y se han apilado en 18 módulos detectores para construir el prototipo de escáner PET del proyecto VIP. La fotografía del primer módulo ensamblado de detección de rayos gamma con 40 detectores de CdTe conectados a 40 chips VIPPIX se muestra en la Figura 6.

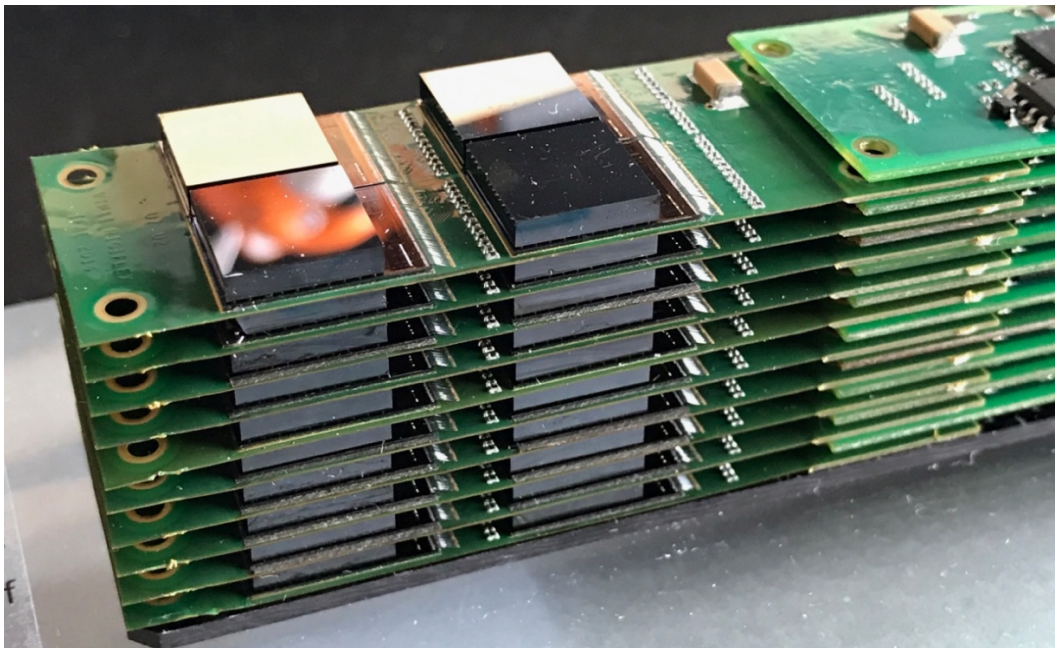

Figura 6. Primer módulo ensamblado con 40 detectores conectados a 40 ASICs VIPPIX.

Una vez ecualizados y calibrados, cinco de los módulos han sido conectados en el anillo del escáner PET y caracterizados con una fuente radioactiva de Sodio-22. Las prestaciones de aproximadamente 18000 píxeles muestran una resolución espectral para el pico de 511 keV de 2.2 % FWHM y una resolución temporal de 60 ns FWHM a -250 V/mm y una temperatura media de 35 grados centígrados. Adicionalmente, la reconstrucción del pico de 511 keV sumando la energía de dos eventos provenientes del mismo fotón muestra una resolución de 3.2 % FWHM lo que ha sido publicado en la revista Physics in Medicine and Biology.

El objetivo principal de la investigación presentada en esta tesis se ha conseguido con éxito. Se ha desarrollado un nuevo escáner PET basado en detectores de Telurio de Cadmio (Figura 7) y se ha caracterizado parcialmente con resultados excelentes. Se ha diseñado un nuevo ASIC de lectura específico para el proyecto, procedimientos de

ecualización y calibración específicos para el gran número de píxeles, así como algoritmos de reconstrucción de imagen optimizados para la nueva geometría del escáner PET. El ASIC VIPPIX es el único circuito integrado de lectura de detectores de estado sólido pixelados capaz de medir **simultáneamente** la energía depositada con una resolución de 10-bit y el tiempo de impacto con precisión inferior a 1 ns.

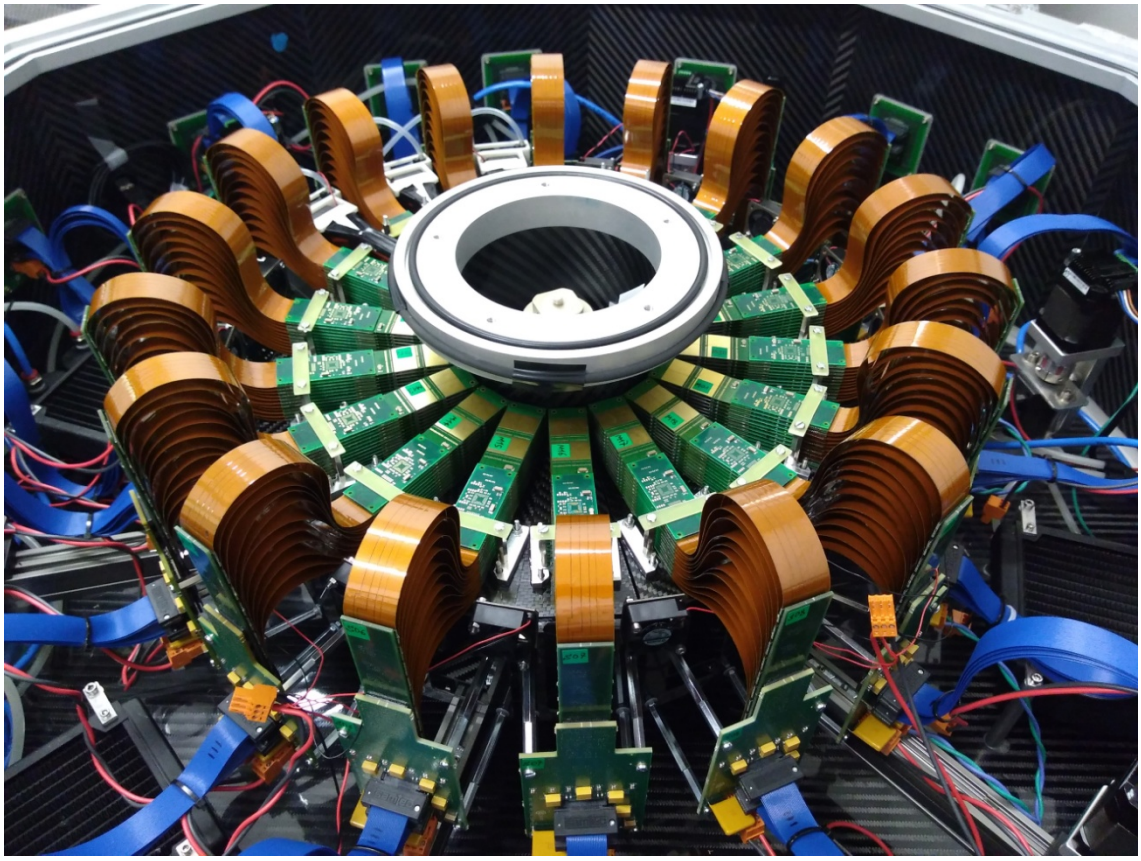

Figura 7. Fotografía del primer prototipo de escáner PET del proyecto VIP con 18 módulos detectores, 720 detectores de CdTe conectados a 720 ASICs VIPPIX, y 72000 píxeles independientes.

Summary

Positron emission tomography (PET) is a molecular imaging technique used for several decades in nuclear medicine. In combination with magnetic resonance imaging (MRI) or computed tomography (CT), PET scanners provide precise physiological information of the human body, what is crucial in oncology, cardiology, and neuropsychiatry. Due to the limited free-path of positrons inside the body and the momentum of electrons before annihilation, the best spatial resolution of PET is approximately 1 mm for human brain scanners. With such limitation, early detection of tumours smaller than 1 mm diameter is not achievable with positron-emission tomography technique individually. Unfortunately, best human brain size PET scanners show much larger minimum detectable tumour sizes than 1 mm diameter due to technological limitations.

An ideal PET scanner should be based on radiation detectors with infinite cross-section, i.e. infinite density, to absorb all gamma-ray photons in the field of view (FOV), an excellent energy resolution to discard all photons that undergo a Compton scattering outside the detector and modify their trajectory, a very precise time stamp generation of the detection to identify back-to-back photons and avoid pile up, and finally very precise spatial resolution to identify exactly the line of response (LOR) of back-to-back photons.

In this thesis, an application specific integrated circuit (ASIC) to readout the energy and the time stamp of a high-density and highly-granulated semiconductor detector for a novel PET scanner design is presented. The research carried out and presented here was realized within the framework of *Voxel Imaging PET pathfinder* ERC project. The aim of the research was to develop detector modules prototype that could be used in positron emission tomography applications and reach their actual physical limits in terms of image quality and resolution in much shorter scanning times than commercially available scanners.

This work is divided into several chapters with the description and the results of the research activities realized in the project. Additionally, it is complemented with the five most relevant published papers that describe the simulated performance of the novel PET scanner, present the measured performance of the semiconductor detectors, detail the pixel electronics and the ASIC, and finally present the energy and timing resolution of the completed prototype detector modules.

The VIP PET scanner is composed of detector modules based on the stacking of hybrid pixelated Cadmium Telluride detectors. CdTe has a high equivalent atomic number and so a high cross section for gamma rays of 511 keV. Provided a minimum radial detection length of CdTe, very good efficiency is expected.

Every CdTe detector has a thickness of 2 mm, is pixelated into an array of 10 x 10 voxels of 1 mm x 1 mm x 2 mm size and is connected to a pixelated ASIC to readout independently the energy and the time stamp of every photon detection in any of the 100 pixels. The full detection volume of the PET ring is divided into more than 6 million voxels with independent energy and timing readout. Such an extreme detection spatial resolution

allows to reach 1 mm diameter physical limitation of PET. Additionally, since the energy resolution of Cadmium Telluride detectors can reach 1-2 % at full width half maximum (FWHM), a very high percentage of detected lines of response are correct since scattered photons are discarded naturally. In consequence, a small set of few millions of acquired LORs is sufficient to generate excellent quality PET images.

Although the time resolution of CdTe detectors at room temperature is still low for high precision applications as time of flight PET, it is sufficient for the VIP PET design due to the excellent purity and resolution of the LORs data set.

The simulated performance of the VIP PET scanner based on realistic performance of CdTe detectors in terms of energy and time resolution has been published and is reported here. As mentioned above, a scatter fraction of 4 % approximately is expected due to an energy resolution of 1.6 % FWHM of the CdTe detectors. This feature allows excellent spatial resolutions of sub 1-mm with reduced data set of 10-20 million coincidences. Due to the limited time resolution of the detectors, best working activity of VIP PET is 32 MBq approximately. The comparison with human brain and body PET scanners as well as with small-animal high resolution PET scanners is presented. VIP PET gets the high resolution of an small-animal PET for human brain diameter size. Such an achievement could potentially boost the research of human brain diseases like Alzheimer and Parkinson.

All simulations are based on experimental performance of 2-mm thickness Cadmium Telluride detectors. The characterization of such detectors using commercially available single-channel readout electronics is reported here and has been published in Journal of Instrumentation. Using a Sodium-22 radioactive source, the 511 keV photopeak resolution and the coincidence time resolution of back-to-back photons were measured with – 1000 V/mm detector bias voltage at -8 Celsius degree. An energy resolution of 1.6 % FWHM and a time coincidence resolution of 6 ns FWHM were obtained for photoelectric interactions.

Prior to the description of the ASIC for VIP PET scanner, the VIPPIX ASIC, a review of available readout ASICs for radiation detectors for three main applications is presented. VIP PET application requires precise simultaneous measurement of energy and timing in pixelated format. The performance of a small sample of ASICs is summarized. VIPPIX ASIC combines the architecture of different applications. Therefore, it is the first ASIC to provide simultaneously excellent energy resolution and precise time stamp of detected events.

The VIPPIX ASIC is described in chapter 6 and two complementary papers published in IEEE Transactions of Nuclear Science. The architecture of the readout integrated circuit (ROIC) is based on an array of 10 x 10 independent pixel electronics controlled by a global controller and a common time to digital converter (TDC). Additional voltage and current references are generated in the ASIC's back-end with a temperature sensor and a chip-ID cell. Every pixel electronics composes of a programmable gain preamplifier with detector's leakage dynamic compensation, a tuneable peak-time pulse shaper connected to a peak-and-detect circuit, a 10-bit successive approximation register (SAR) analog-to-digital converter (ADC), a pulse discriminator with adjustable offset, and a local pixel digital controller.

The design and the fabrication of the ASIC have been realized in several stages. First the analog front-end of the pixel and the SAR ADC were fabricated and characterized standalone. The pixel's equivalent noise charge (ENC) is 133 e- RMS for positive polarity detector bias settings and 150 e- RMS for negative ones. Electronics time jitter is approximately 1 ns for energy depositions larger than 200 keV and the time resolution of the integrated TDC is 600 ps FWHM.

Prior to the integration of the 10 x 10 pixel array ASIC, a mini VIPPIX with a 4 x 4 pixel array was fabricated and characterized with a dedicated CdTe detector matching the pixel array geometry of the mini ASIC. First spectroscopy results using pixelated CdTe with VIP dedicated ASIC were published. For Cobalt-57, the photopeak at 122 keV showed an energy resolution of 3.6 % at -500 V/mm and at room temperature.

A full engineering run with 12 wafers of VIPPIX ASIC has been fabricated, post-processed, and characterized. Best quality ASICs were mounted on 720 CdTe detectors and stacked in 18 detector modules with 40 hybrid detector each to build the VIP PET prototype. Five modules were inserted into the VIP ring and characterized with a Sodium-22 radioactive source after an equalization and calibration procedure. The performance of approximately 18000 pixels shows a 511 keV photopeak resolution of 2.2 % FWHM and a coincidence time resolution of 60 ns FWHM at -250 V/mm and 35 Celsius degree average temperature. Additionally, the reconstruction of 511 keV peak adding a Compton scattering and a photoelectric interaction shows a 3.2% FWHM resolution and has been reported in Physics in Medicine and Biology peer reviewed journal.

The main goal of the research presented in this thesis has been accomplished. A new PET design based on pixelated Cadmium Telluride detectors using dedicated readout ASICs, equalization and calibration procedure, and image processing algorithms has been fabricated and partly characterized. The new developed ASIC is the only available readout integrated circuit able to provide energy resolution with 10-bit accuracy and generate trigger time stamp with sub-nanosecond precision.

Acknowledgements

I would like to thank my supervisors along my research career Prof. Peter Weger, Dr. Norbert Fiebeg, Prof. Josep Samitier, Dr. Santiago Marco, Prof. José María López Villegas, Prof. John R. Long, Prof. Joachim N. Burghartz, Dr. Leo C. N. de Vreede, and Dr. Slobodan Mijalkovic for sharing their knowledge with me during the past years at the Institute of Microelectronics in Frankfurt an der Oder (Germany), at the Delft University of Technology (The Netherlands), and at the University of Barcelona (Spain).

I would like also to thank Dr. Mokhtar Chmeissani, my supervisor at IFAE, for trusting me for the design of the VIPPIX ASIC, ERICA ASIC, and for the coming integrated circuits.

I am very grateful to Dr. Ángel Diéguez for accepting my Ph.D. supervision and sharing his inspiring ideas with me. I am sure in the coming future we will develop a project together.

To all my colleagues at DIMES and Delft University of Technology, Atef Akhnoukh, Dr. Huang Cong, Dr. Han Yan, Dr. Koen Buisman, and Prof. Lis Nanver thank you all for your support, coffee breaks, barbecues, and wonderful years I could share with you in Delft.

I am immensely grateful too to my colleagues at the Department of Electronics of the University of Barcelona Dr. Albert Cornet, Dr. Atilà Herms, Dr. Mauricio Moreno, Dr. José Bosch, Dr. Javier Sieiro, Dr. Anna Vilà, Dr. Manel López, Dr. Óscar Alonso, and Dr. José María Gómez for their continuous support in research and teaching.

I would like to thank my colleagues at the Institut de Física d'Altes Energies, Dr. Ramon Miquel, Dr. Matteo Cavalli, Dr. Federico Sánchez, Dr. Thorsten Lux, Dr. Sebastian Grinstein, for their support and courage since I joined IFAE.

I am very grateful too to the VIP project team members, Dr. Maher Sarraj, Dr. Machiel Kolstein, Thomas Moore, Dr. Katya Mikhaylova, Dr. Yonatan Calderón, Carles Puigdengoles, Jorge Garcia, Xavier Prats, and Ricardo Martínez for their support in design, layout, coding, and analysis of data.

Finally, I thank my family, my parents Juan and Rosa, my brother Rafa and his family, my wife Bing and her family, and my daughter Ela for being so patient and supportive with me.

Contents

Resumen i

Summary ix

Acknowledgement xiii

Contents xv

List of Figures xvii

List of Tables xix

List of Acronyms xxi

1. Introduction 1

2. PET fundamentals, technologies, and scanners 3

2.1 Fundamentals of Positron Emission Tomography 3

2.2 PET detector technologies 5

2.3 Future PET detectors 9

3. The Voxel Imaging PET pathfinder project and scanner 13

3.1 Summary of article "Simulation of the Expected Performance of a Seamless Scanner for Brain PET Based on Highly Pixelated CdTe Detectors" 13

3.1.1 Description of the VIP scanner 13

3.1.2 Simulations 16

3.1.3 Results 17

3.1.4 Conclusions 18

4. Cadmium Telluride Detectors for PET 19

4.1 Summary of article "Energy and coincidence time resolution measurements of CdTe detectors for PET" 23

4.1.1 Energy resolucion measurement results 25

4.1.2 Coincidence time measurements results 25

5. Readout ASICs for radiation detectors 27

5.1 Photon Counting Readout ASICs 28
5.2 Spectroscopic Readout ASICs 32
5.3 Time of Flight Readout ASICs 35
6. Design of the VIPPIX ASIC 41
6.1 Specifications of VIPPIX ASIC from the operating conditions of the VIP detector ring 41
6.2 Specifications of VIPPIX ASIC from the geometrical specifications of the CdTe detector 42
6.3 Specifications of VIPPIX ASIC from the electrical specifications of the CdTe detector 43
6.3.1 Architecture of the pixel front-end 43
6.3.2 Detector Leakage compensation 44
6.3.3 Preamplifier baseline restore time 44
6.3.4 Peak time of shaper 45
6.4 Summary of article "Toward VIP-PIX: A Low Noise Readout ASIC for PIxelated CdTe Gamma-Ray detectors for Use in the Next Generation of PET Scanners 45
6.4.1 Introduction to VIPPIX 46
6.4.2 Measurement results 47
6.4.3 Conclusions 49
6.5 Summary of article "A 2D 4x4 Channel Readout ASIC for Pixelated CdTe Detectors for Medical Imaging Applications" 49
6.5.1 VIPPIX ASIC and Pixel architecture 50
6.5.2 Pixel electronics measurement results 52
6.5.3 Back-end circuits measurements 52
6.5.4 First spectroscopy results and conclusions 53
7. Fabrication and assembly of VIP PET prototype 55
8. Equalization and first results of the VIP detector module 63
8.1 Summary of article "First results of a highly granulated 3D CdTe detector module for PET" 65
8.1.1 Materials and methods 65
8.1.2 Results 66
8.1.3 Conclusions and future work 67
9. Conclusions and future work 69
Bibliography 75
Collection of papers 83

List of Figures

Figure 1. Basic block diagram of PET imaging 4

Figure 2. Two detector solutions based on scintillating crystals and photomultiplier and SiPM array 8

Figure 3. Comparison of the performance of some scintillator based and semiconductor based small animal PET scanners. 12

Figure 4. Geometry of Voxel Imaging PET Scanner. 14

Figure 5. NEMA NU4-2008 phantom geometry 18

Figure 6. Reconstructed Images of NEMA NU4-2008 phantom 18

Figure 7. Standard metallization and readout electrical schemes of CdTe sensor. 20

Figure 8. Mobility of Electrons and Holes versus temperature plots 21

Figure 9. Charge injection performance of a CdTe detector with four different depth of interaction impact points. 21

Figure 10. Detector Bias and Temperature dependency of CdTe Leakage current 22

Figure 11. Weighting potential along the interaction depth for three ratios of pixel size over detector thickness 23

Figure 12. ^{241}Am spectroscopy obtained with a CdTe planar detector and a CdTe pixelated detector 23

Figure 13. Dimensions and photography of the 2-mm thickness CdTe planar detector used 24

Figure 14. Electrical block diagram of the spectroscopy setup based on Amptek PC250 and PC275 readout electronics. 25

Figure 15. Illustration of the coincidence time measurement setup with two identical readouts in a face-to-face configuration 26

Figure 16. Generic block diagram of a first amplification stage for semiconductor detectors and corresponding current and output voltage waveforms 28

Figure 17. Electrical scheme of the pixel electronics of Medipix3 chip 29

Figure 18. XPAD3-S pixel front-end electronics 29

Figure 19. PILATUS3 pixel block diagram 30

Figure 20. Simplified block diagram of pixel of ChromAIX2 ASIC 31

Figure 21. Block diagram of pixel electronics of ERICA ASIC 32

Figure 22. Architecture of one front-end channel of VATA64-HDR16 ASIC 33

Figure 23. Block diagram of a pixel electronics of HEXITEC ASIC 33
Figure 24. Timepix pixel's electronics block diagram..... 34
Figure 25. Analog pixel scheme diagram of FE-I4B ASIC 35
Figure 26. Block diagram of IDeF-X ASIC..... 36
Figure 27. Block diagram of Triroc ASIC..... 37
Figure 28. One channel pixel electronics block diagram of TOFPET2 ASIC 37
Figure 29. Block diagram of PETIROC-2A ASIC from Weeroc SAS 38
Figure 30. Difference in trigger time of electron and hole collection versus the percentage of full charge injection and different shaper's peak time. 44
Figure 31. Block diagram of the VIPPIX ASIC..... 46
Figure 32. VIPPIX pixel electronics block diagram. 47
Figure 33. Testing PCB of VIPPIX individual parts and detailed photography of a packaged ADC in a 48-Pin CLCC chip carrier. 48
Figure 34. VIPPIX Pixel's operation modes and Input/Outputs. 50
Figure 35. VIPPIX's operation modes and digital Input/Outputs..... 51
Figure 36. Photography of a hybrid pixelated CdTe detector on a VIPPIX 4x4 pixel matrix readout ASIC. 53
Figure 37. Illustrated photography of the VIPPIX ASIC and its layout. 56
Figure 38. Flow diagram of the construction of the VIP PET scanner 56
Figure 39. Layout and photography of the 10 x 10 pixel fabricated CdTe detector..... 57
Figure 40. Flex PCB with 4 CdTe hybrid detectors based on pixelated CdTe bump-bonded to a VIPPIX ASIC, without CdTe detector, and FPGA PCB..... 58
Figure 41. Layout of the 16-bit Chip-ID cell and detailed photography of 4 bits with two open circuits and two shorted pads equivalent to '1001' 58
Figure 42. Quality wafer maps of ASIC total current consumption..... 59
Figure 43. First assemble VIP detector module with 40 hybrid detectors..... 59
Figure 44. 3D CAD design of the full VIP PET scanner prototype 60
Figure 45. Photography of the completed VIP PET scanner..... 61
Figure 46. Flow diagram of the pixel's equalization algorithm. 64
Figure 47. Distribution of the 5 VIP detector modules in the VIP PET ring. 66

List of Tables

Table I. Summary of properties of Scintillating crystals 7

Table II. Comparative table of photodetectors properties.....8

Table III. Main features of commercial PET and PET/CT scanners 9

Table IV. Summary of properties of some semiconductors for gamma-ray detection [56-59].....10

Table V. Photon cross sections in semiconductor detectors and BGO scintillator crystal at characteristic energies for PET [70]. 11

Table VI. VIP detector ring parameters used in GAMOS simulations. 16

Table VII. Measurement results of individual parts of VIPPIX pixel front-end.....48

Table VIII. Specifications of the 4x4 pixel readout ASIC. 54

Table IX. Summary of the published results of VIPPIX ASIC and VIP detector module. 71

List of Acronyms

ADC	Analog-to-Digital Converter
APD	Avalanche Photo-Diode
ASIC	Application Specific Integrated Circuit
BJT	Bipolar Junction Transistor
CCD	Charge Coupled Device
CMOS	Complementary Metal Oxide Semiconductor
CT	Computed Tomography
CZT	Cadmium Zinc Telluride
DAC	Digital-to-Analog Converter
DICOM	Digital Imaging and Communications in Medicine
DOI	Depth Of Interaction
ENC	Equivalent Noise Charge
FBP	Filtered Back Projection
FDG	18F-FluoroDeoxyGlucose
FIFO	First-In First-Out
FOM	Figure Of Merit
FOV	Field Of View
FPGA	Field Programmable Gate Array
FWHM	Full Width at Half Maximum
GAMOS	GEANT4-based Architecture for Medicine-Oriented Simulations
GEANT	Geometry And Tracking
IC	Integrated Circuit
LM	List Mode
LM-OSEM	List-Mode Ordered Subset Expectation Maximization
LOR	Line Of Response
LSB	Least Significant Bit
LSO	Lutetium Oxyorthosilicate
LUT	Look-Up-Table
LYSO	Lutetium-Yttrium Oxyorthosilicate
MC-PMT	Multi-Channel PMT
MiM	Metal-in-Metal
MOS	Metal Oxide Semiconductor
MOSFET	Metal Oxide Semiconductor Field Effect Transistor
MPW	Multi-Project Wafer
MRI	Magnetic Resonance Imaging
MTF	Modulated Transfer Function
MSB	Most Significant Bit

NEC	Noise Equivalent Count
NEMA	National Electrical Manufacturers Association
NF	Noise Figure
NPS	Noise Power Spectrum
NTF	Noise Transfer Function
OE	Origin Ensemble
OSEM	Ordered Subset Expectation Maximization
PCB	Printed Circuit Board
PEM	Positron Emission Mammography
PET	Positron Emission Tomography
PMT	Photomultiplier Tube
PSF	Point Spread Function
PS-PMT	Position-Sensitive PMT
PTAT	Proportional To Absolute Temperature
QE	Quantum Efficiency
RC	Recovery Coefficient
RF	Radiofrequency
ROIC	Readout Integrated Circuit
ROI	Region Of Interest
SAR	Successive Approximation Register
SF	Scatter Fraction
SiPM	Silicon Photomultiplier
SNDR	Signal-to-Noise and Distortion Ratio
SNR	Signal-to-Noise Ratio
SOR	Spill-Over Ratio
SPECT	Single Photon Emission Computed Tomography
STD	Standard Deviation
TDC	Time-to-Digital Converter
TOF	Time Of Flight
TOT	Time-Over-Threshold
UBM	Under Ball Metal
USB	Universal Serial Bus
VIP	Voxel Imaging PET
WB	Whole Body

Chapter 1

Introduction

Positron Emission Tomography (PET) scanner is one of the most practical applications of translation of know-how used in fundamental physics, in this case high energy particle physics, to one modality of medical imaging. Nowadays, the physiological properties of the human body can be obtained in less than one hour, what is of crucial relevance in oncology, cardiology, and neuropsychiatry. Nevertheless, despite the potentials of the PET, as molecular imaging tool, the technological limitations, at the level of the detectors and image reconstruction, have limited the image quality and so the use of PET scanners. In the 1990´s, with the introduction of dual imaging modality PET/CT and PET/MRI, the PET scanner become a viable molecular imaging modality. Since past decade, with new and better detection technologies, high resolution and high sensitivity PET scanners have been developed to provide more precise metabolic images and allow earlier diagnosis of tumours. Thought the improvements, whole-body and human-brain PET scanners are still far from the physical limits of ideal PET imaging.

The research presented here was carried out within the framework of a project funded by a European Research Council (ERC) advanced grant to develop the next generation of human brain PET scanners based in pixelated solid-state detectors which should reach the physical limits of positron emission tomography [1,2]. Such a complex project was developed by an interdisciplinary team with physicists, mechanical engineers, and electrical engineers. This thesis presents the development of the application specific integrated circuit (ASIC) as fundamental part of the PET scanner. Additionally, the characterization of the pixelated solid-state detectors and the fabricated PET detection modules are reported.

The simulation results of the presented novel PET scanner show a potential spatial resolution of 1 mm at full width half maximum in all directions with much lower number of collected events than currently available PET scanners. This characteristic can be used to either reduce the scan time to tens of seconds, or to decrease the injected dose per patient. Such a feature is a consequence of a scatter fraction of 4 % obtained with high Z detector material with energy resolution of 1.6 % FWHM for PET events.

The design of the presented ASIC was realized in three steps: design of individual blocks, integration of a small array, and final integration of full ASIC. Every prototype has been properly characterized and the experimental results were used to improve the design of the integrated versions. The complete readout ASICs have been fabricated and assembled to the detectors successfully. The detector modules that compose the full PET

scanner prototype have been characterized and first experimental results have been published recently and are presented here. An energy resolution of 2.2 % FWHM is achieved based on the performance of approximately 18000 pixels.

This thesis is presented as a collection of five published articles accompanied of nine chapters that help the reader to understand the state of art and the challenges of developing a new PET scanner and completes the description of the fabricated ASIC and PET scanner prototype.

A description of the thesis, chapter by chapter, follows:

- Chapter 2: The fundamentals of Positron Emission Tomography from a physical perspective are introduced from the radiotracer selection to the image reconstruction algorithms. The available detector technologies and the future ones are reviewed as well.
- Chapter 3: ERC project “Voxel Imaging PET pathfinder” and the novel VIP PET scanner are presented. The original architecture is detailed and justified in terms of expected performance. First article with the simulation results of VIP PET scanner is summarized.
- Chapter 4: As fundamental part of the VIP detector module, Cadmium Telluride detectors are analysed in this chapter. The types of metallization, the charge collection efficiency, the polarization, the pixel effect, and the leakage current are discussed. Additionally, the summary of the second article with the experimental results of planar CdTe detectors is included.
- Chapter 5: PET application demands high spatial resolution, excellent energy resolution and precise time stamp generation. Since no available ASIC provided all three features simultaneously, a review with the available readout ASICs for radiation detector for photon counting imaging, spectroscopy, and time of flight applications is presented to identify the best performance of each application.
- Chapter 6: As mentioned above, the specifications of PET application set the requirements of the electronics. Additionally, the physical and electrical properties of the Cadmium Telluride detector establish the trade-offs in the design of the ASIC. The VIPPIX ASIC has been designed specifically for PET applications using CdTe pixelated detectors. The architecture of the pixel electronics and the ASIC are discussed. The performance of the ASIC prototypes is shown in the third and fourth articles. Therefore, their summaries are included in this chapter.
- Chapter 7: The successful development of the VIPPIX ASIC lead to the fabrication of the VIP detector modules. The post-processing steps and the fabricated modules are presented in this chapter.
- Chapter 8: Prior to the completion of the full VIP PET prototype, five detector modules were properly equalized, calibrated, and characterized with Sodium-22 radioactive source in terms of energy and coincidence time resolution. The summary of the last article with the first results of these five modules is included.
- Chapter 9: This final chapter deals with the conclusions which are drawn from this work. The main results are summarized, and their significance are analysed. Additionally, since the characterization of the full VIP scanner is not presented in this work, the next steps and future improvements of the electronics are also discussed.

Chapter 2

PET fundamentals, technologies, and scanners

2.1 Fundamentals of Positron Emission Tomography

Positron emission tomography is a non-invasive nuclear medical imaging technique for in vivo quantitative measurements of physiologic parameters of tissues and organs. Unlike computed tomography (CT) or Magnetic Resonance Imaging (MRI), which look at anatomy or body form, PET shows metabolic activity or function and physiology in cardiology, neurology, and oncology. In particular, it has been used to assess the benefits of coronary artery bypass surgery versus heart transplant, identify causes of childhood seizures and adult dementia, and detect and distinguish between benign and malignant tumours [3].

PET is based on the detection of very small quantities of biological substances which are labelled with a positron emitter. Most commonly used are carbon- 11, oxygen-15, nitrogen-13, and fluorine-18 [4]. Advantages of positron labelled substances are their very high molecular targeting, the possibility of using biological active substances without changing their behaviour by the label, and fulfilment of the tracer principle. Thus, the process of interest remains unchanged during the measurement [5]. Target structures of these molecules are e.g. glucose metabolism, receptor binding potential, catecholamine transport, amino acid transport, or protein synthesis [6]. All the mentioned nuclides have very short radioactive half-lives (2 min for O-15, 109 min for F-18), which necessitates a nearby cyclotron and radiochemistry facility [7].

Imaging of regional tracer concentration is accomplished by the unique properties of positron decay and annihilation. Proton-rich isotopes can undergo a beta+ decay and proton changes to a neutron inside the nucleus and a positron. The positron traverses freely the tissue after the emission from the parent nucleus slowing down until it interacts with a free electron inside the body [8]. The positron decays by annihilation, generating a pair of gamma rays which travel in nearly opposite directions with an energy of 511 keV each [9]. The opposed photons from positron decay can be detected by using pairs of collinearly aligned detectors in coincidence. The detector pairs of a PET system are installed in a ring-like pattern as shown in Figure 1, which allows measurement of radioactivity along lines through the organ of interest at a large number of angles and radial distances. Subsequently, this angular information is used in the reconstruction of tomographic images of regional radioactivity distribution. State-of-the-art positron emission tomography scanners consist of multiple, closely packed rings of detectors that enable simultaneous imaging of several image planes. Coincident events between rings of the camera are acquired to generate

cross-data, which minimizes data gaps between imaging planes. Such data acquisition allows almost complete data sampling in three dimensions (3D PET). The raw data are integrals along the line-of-coincidence over the activity distribution. If the timing resolution of the detectors is good enough and time-of-flight information is included in the measurement, the region of interest is limited along the line of response (LOR) [10].

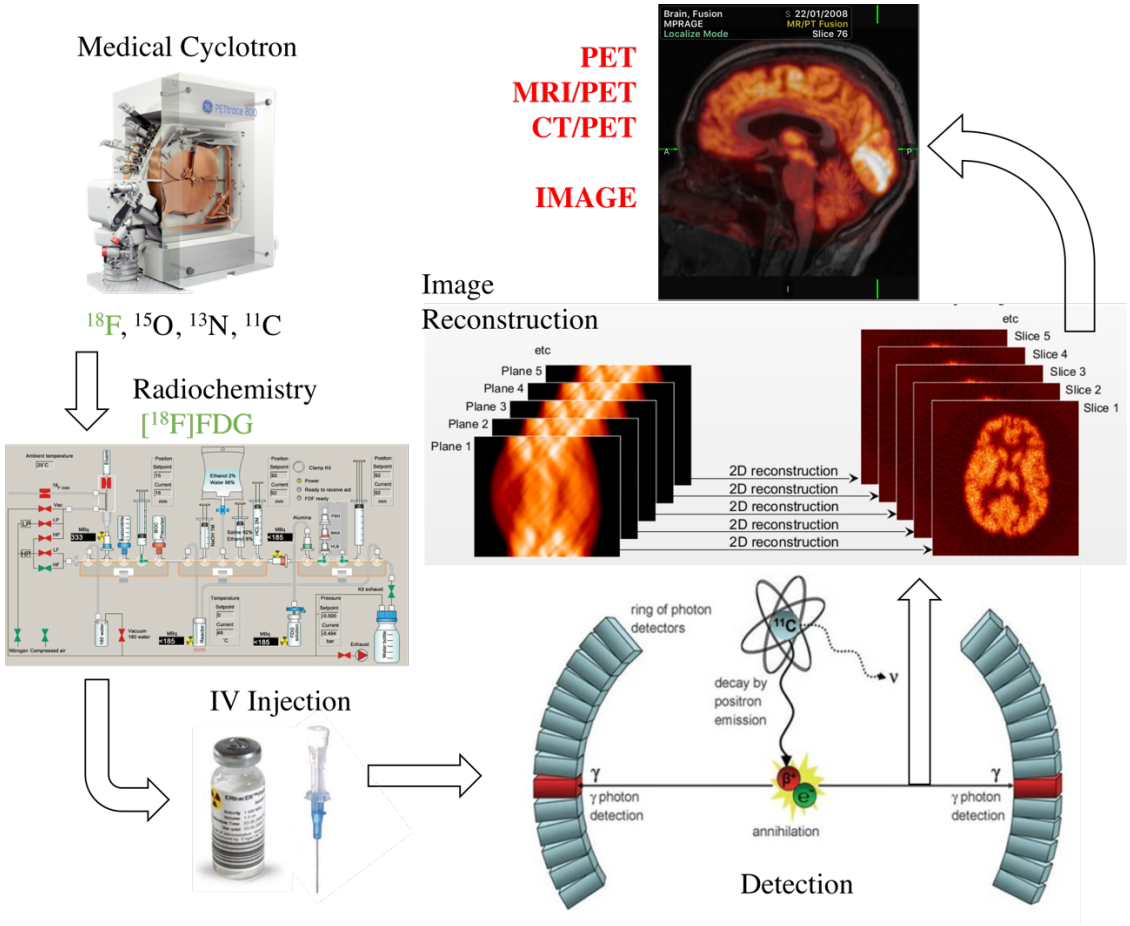

Figure 1. Basic block diagram of PET imaging

Reconstruction algorithms are used to calculate the underlying activity distribution. Statistical, iterative reconstruction algorithms have become the method of choice in many cases because of their superior image quality compared to traditional filtered back-projection methods [11-13].

The spatial resolution which can be achieved in a PET image is principally limited by positron range and gamma ray non-collinearity which set a 1-mm spatial resolution limit for a human brain scanner [14]. In addition to that, the width of the detection elements in the scanner determines the width of the coincidence response function and thus the image resolution [15].

The working flow for a PET scanning is shown in Figure 1. The radioisotopes are produced in a cyclotron. Most common radiotracer, the 2-deoxy-2-(^{18}F)fluoro-D-glucose or

fluorodeoxyglucose (^{18}F-FDG) is obtained by a radiochemistry process labelling deoxyglucose with ^{18}F. The proper dose is injected to the patient which must wait from 30 to 60 minutes before the scanning for a complete absorption of the radiopharmaceutical. The total dose injected depends on the type of test, the properties of the tissues to scan, the PET scanner, and mostly the radioisotope and its half-life time. For FDG, the dose range goes from 185 MBq for Philips-ADAC CPET PET/CT system to 740 MBq for the General Electric Advance NXI system [16]. The scanning of the patient takes from 30 minutes to 90 minutes depending on the length of the part of the body to be examined [17]. The simultaneous detection of the back to back photons coming from every annihilation is recorded in a coincidence processing unit. Usually, coincidence windows of 10 ns are used in commercial PET systems [18]. The processing unit defines the line of response (LOR) of every pair of photons based on the position of the triggered detectors. The set of all lines of response detected by the PET scanner are used by one or various image reconstruction algorithms to obtain the 3D map of physiological activity of the scanned organs.

After all corrections (e.g. for scattered photons, random coincidences and the effects of attenuation) have been applied to data acquired in the PET camera, the number of counts assigned to an LOR joining a pair of detector positions is proportional to a line integral of the activity along that LOR. Parallel sets of such line integrals are known as projections. Reconstruction of images from projections is a problem to which much attention has been paid over the last 30 years, and many analytical and iterative reconstruction schema exist. For 2D reconstruction, the most commonly used algorithm is the analytical method called Filtered Back-projection (FBP) [19]. FBP is straight-forward to implement but does have the property of amplifying statistical noise in the signal. Recently, considerable interest has been shown in iterative reconstruction schema, such as the Ordered Subsets - Expectation Maximisation (OSEM) algorithm [12], which possess different noise properties to FBP. For 3D reconstruction, the Reprojection and Filtered Back-projection (3D-RP) method has been the most popular, in part because of the significant computational burden of newer 3D iterative reconstruction methods [20]. 3D-RP itself is computationally expensive, and this has led to the development of approximate 3D reconstruction algorithms. Of these, Fourier Rebinning reduces the 3D problem to a series of 2D problems without significantly distorting the image and results in a significant reduction in the computational burden, so it is stimulating interest [21].

Every PET scanner manufacturer develops its own graphic user interface to display the reconstructed PET images. Usually, they are displayed as a PET with MR or CT fusion image due to the lack of resolution in the PET image compared to Magnetic resonance or computer tomography. The CT and MRI scan images are also used to reconstruct a 3D map of attenuation factor to correct for 511 keV detected photons. PET image files must be exported following a well-established standard to facilitate data base sharing among medical doctors [22].

2.2 PET detector technologies

Since the invention of first PET detectors in 1955 [16] the fundamental principle of PET scanners remains unchanged: Detectors should provide the energy, the impact position, and the time stamp of the interaction with the highest resolution to approach the physical limitations of positron emission and annihilation processes inside the body [23]. Such limits depend on the density and the chemistry of the media. For brain PET, angular uncertainty

and the movement of the positron inside the brain introduces a minimum spatial resolution of 1-mm approximately [24].

Unfortunately, since 1955 the image resolution of all developed PET scanners for brain or full body, commercialised or in prototype phase, is far from 1-mm at full width of half maximum (FWHM) resolution. This means basically that a 1-mm diameter tumour anywhere in the body can't be distinguished from background noise in oncology applications. Compared to the resolution achievable by computer tomography and magnetic resonance imaging developed in the 70s and the 80s respectively, PET technology was on a second place until the implementation of the 18F-FDG radiotracer. Due to the intrinsic marking of glucose in biology metabolism, and relatively long half-life time (110 min) which means that the cyclotron does not need to be next to PET scanner, the positron emission tomography re-gained importance and many different research lines targeted the improvement of the spatial resolution and thus the image resolution, as well as, the energy and timing resolution of the detectors [25]. Many publications about the history of PET devices and detectors are available in the literature [26-28].

Photons interact with matter by means of Rayleigh scattering, Compton scattering, photoelectric absorption or pair creation. Particles or radiation detectors should not only stop the particle and absorb its energy but also deliver this energy as a linear amount of charge, light, heat, or any other magnitude that can be quantised by the detector readout. So originally in the 50s, the detection of the gamma-ray photons was performed by scintillator crystals as indirect measurement of the energy of the photons due to the high stopping power of scintillating material such as Sodium Iodine (NaI) and its easy processing and manufacturing [29]. Scintillator crystals absorb the energy of the photons and convert it partially into visible light. Their most interesting properties for PET scanners are the following [30]:

- they have very high detection efficiency, i.e., the percentage of photons absorbed in the crystal versus the total number of photons crossing the scintillator. The stopping power depends on the atomic number such as the larger Z, the higher detection efficiency.
- they are very linear, i.e., the amount of light emitted is linearly proportional to the deposited photon energy. Depending on the material, a crystal emits different number of photons per unit of absorbed energy, thus shows a different photon yield (photons/keV) from one crystal to another.
- they have a very low time jitter, sub nanosecond, due to a very fast light emission mechanism.

Since all the figures of merit depend strongly on the row material and the type and concentrations of the dopants, plenty of research has been published, and many different types of scintillating crystals are available nowadays. Table I summarises some properties of most common inorganic scintillating materials [31-33].

Along the decades, also the geometry of the scintillators has experienced great improvements always seeking smaller form factors with better detection efficiencies. Nowadays, one can find scintillator arrays with 14 x 14 lutetium oxyorthosilicate elements of 13 mm length with a crystal size of 0.43 x 0.43 mm at the front end and 0.80 x 0.43 mm at the back end [34-36]. These solutions provide the PET scanning with better axial and tangential spatial resolutions.

Once the crystal provides the flux of visible light photons, coupling the crystal to a photodetector is necessary to obtain a linear measurement of the original energy of the

gamma photon. Note that the maximum photon transmission from the scintillating crystal to the photodetector will occur when both devices have the same refractive index. If this is not the case, additional loses must be considered in the calculation of the detector's overall gain which a priori is the product of the photon yield of the scintillator, and the quantum efficiency and the gain of the photodetector.

Table I. Summary of properties of Scintillating crystals obtained from [31-33].

Crystal	Density [g/cm3]	Effective Z	Decay time [ns]	Photon Yield /keV
LSO / LYSO	7.40	65	47	25
BGO	7.13	75	300	8.2
GSO	6.71	59	56-400	15
$LaBr_3(Ce)$	5.29	46	26	63
BaF_2 fast	4.89	53	0.6	1.4
CsI(Na)	4.51	54	460 – 4180	39
CsI(Tl)	4.51	54	680 – 3340	65
NaI(Tl)	3.67	51	230	38
CaF_2	3.18	17	900	24
Plastic	1.03	12	2	10

As in the case of scintillating materials, a very wide number of photodetector technologies are available in both, the market and the literature [37,38]. Nevertheless, for PET applications, photodetectors must have high gain, and specially should work at very high speeds. Therefore, only three main solutions are considered traditionally for PET detectors: photomultiplier tubes (PMT), avalanche photodiodes (APD), and Silicon photomultipliers (SiPM). PMTs are part of PET scanners since the very first PET detector was realised with two scintillator crystals connected to a photomultiplier tube each in face-to-face configuration in 1950. They are based on the multiple acceleration and multiplication of photoelectrons generated at the cathode. Total gain is achieved by a cascade of strong electric fields in vacuum such as the total applied voltage from cathode to anode might be of several hundreds of Volt. Due to the intrinsic operation principle, they are not suitable for very small geometry. Therefore, APDs and SiPMs are being used in latest PET scanner prototypes [39-43]. Table II summarises some figures of merit of PMTs, APDs, and SiPM [39-42].

Most avalanche photodiodes are based in Silicon, GaAs, InGaAS, Germanium, Gallium-Nitride, or HgCdTe semiconductor material depending on the application wavelength. They are built using microelectronics photolithography technology with specific doping profiles. The detection mechanism is based on electro-hole pair creation through the photoelectric effect. Their gain is obtained with high electric field in a low doped p-type region [44]. Note that due to the strong dependency with Temperature of semiconductor devices, the gain and linearity can change dramatically within few Celsius degree range as shown in Table II. Therefore, precise temperature control is necessary if certain energy resolution is required. Additionally, since drifting is the transport mechanism, they suffer of larger jitter than PMTs because the first electron-hole is created at different depth inside the devices while in PMTs the photoelectron generation is well defined in the cathode.

Silicon photomultipliers are basically 2D arrays of small avalanche photodiodes connected in parallel and biased with a voltage larger than the p-n junction breakdown voltage such as they work in Geiger mode [45]. They require a quenching resistor to stop forward current pulses and restore DC bias condition. As any APD, DC restore time can take

from few hundreds of nanoseconds to some microseconds. Note that working in Geiger mode requires higher control of the gain of the SiPM to maintain the energy resolution and linearity but decreases dramatically the jitter of the pulses. Therefore, they are being used in PET designs where excellent time resolution is needed such as the time-of-flight (TOF) PET [46].

Table II. Comparative table of photodetectors properties [39-42].

	PMT	**APD**	**SiPM**
Gain	10^5-10^7	50-1000	10^5-10^6
Time Jitter [ns]	> 0.3	> 1	> 0.1
Efficiency (@ 420nm) [%]	25	70	25-75
Bias [V]	≥ 1000	300 – 1000	15-100
Temperature Coefficient [%/°C]	< 1	2-3	1-8
Magnetic Field Compatibility	No	Yes	Yes
Active Area	1-2000 mm²	1-100 mm²	1-10 mm²
Price/channel [USD]	> 200	~100	~50

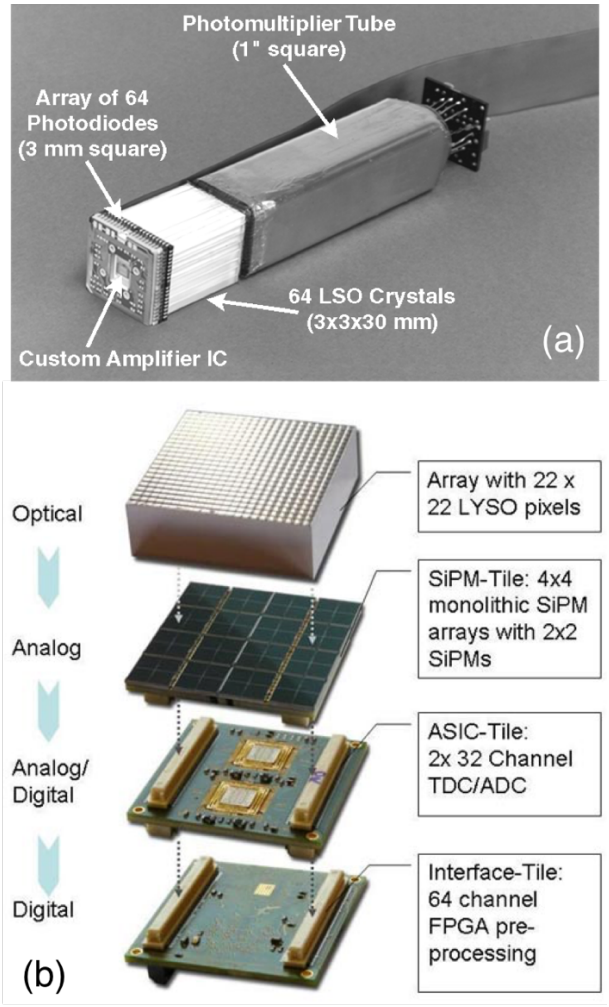

Figure 2. Two detector solutions based on scintillating crystals and photomultiplier (a) and SiPM array (b) [47,48].

Figure 2 shows two available PET detector solutions used in pre-clinical PET scanners. Figure 2a illustrates a classical LSO scintillator crystal connected to a photomultiplier tube with an extra photodiode layer in the front to improve spatial resolution with the measurement of the position of the impact inside the LSO crystal, and Figure 2b illustrates the composition of recent LYSO crystal connected to a SiPM from Phillips [47,48].

Detectors from clinical PET scanners are based on scintillators coupled to PMTs and SiPMs so far. Such detectors are used as well in dedicated-organ scanners such as the Positron Emission Mammography (PEM) scanners [49,50]. In the world, the leading manufacturers, such as General Electric Corporation, Siemens Medical Solutions, and Philips Healthcare, offer complete PET, PET/CT, PET/MR solutions. In Table III, the properties of the main models of PET scanners and PEM scanners are summarized [49-51].

Table III. Main features of commercial PET and PET/CT scanners [49-51].

	Phillips		Siemens		GE Healthcare	
	GEMINI TF Big Bore	GEMINI TF 64 (PET/CT)	Biograph mCT	Biograph TruePoint	Discovery VCT	Discovery PET/CT 600
Sensitivity 3D (cps/kBq/cc)	7.2	7.2	9.5	7.6	9.1	9.1
Transverse Resolution At 1cm / 10cm (mm)	4.7 / 5.2	4.7 / 5.2	4.4 / 5.8	4.2 / 4.8	5.0 / 5.4	5.1 / 5.6
Axial Resolution At 1cm / 10cm (mm)	4.7 / 5.2	4.7 / 5.2	4.5 / 4.8	/ 5.5	5.0 / 5.6	5.6 / 6.3
Peak Noise Equivalent Count Rate (kcps) (3D)	94	110	100	165	78	76
Scatter Fraction (%)	31	30	< 36	< 36	36	38

2.3 Future PET detectors

The aim for high quality images with better spatial resolution and contrast obtained with a significantly lower dose intake pushes for new gamma-ray detectors with higher energy discrimination, smaller jitter, and higher detection efficiency. Certainly, small form-factor scintillating crystals connected to silicon photomultipliers are a promising technology for time-of-flight positron emission tomography (TOF-PET) scanners [52]. The idea to use time-of-flight (TOF) information in PET image reconstruction was originally proposed in the 1960's at a very early stage in the development of positron imaging. By the early 1980s, fully functional TOF PET systems had been built, not long after the first conventional PET systems were completed.

The concept of time-of-flight is simple: for every back to back photon detection, the time of arrival difference is measured from detector A to detector B. Ideally, time of arrival with zero uncertainty would provide the exact point along the line of response formed from A

to B where the annihilation of the positron occurred. Nevertheless, with limited time precision, the ideal annihilation point extends to a region along the LOR. Nowadays, due to faster scintillators and faster photodetectors, time resolutions in the order of 600 ps at FWHM are available [53]. The region of the LOR is then limited to approximately 9 cm which reduces dramatically the noise introduced in the image reconstruction process because just 9 cm of LOR is back projected instead of the full LOR length. In 2017, Philips announced Philips Astonish TF, a 495 ps FWHM resolution ToF PET with full body resolution of 2 mm using point spread function image reconstruction algorithms [54].

In parallel to scintillating mechanism, an old gamma-ray detection technology used for astronomy and cosmology landed into the gamma-ray detection for PET applications. In nuclear physics, the electron-hole pair generation in solid-state detectors was performed by the first time in 1951 with a relatively thin surface barrier germanium device to detect short-range particles. [55]. Since then, different materials have been used for different applications and energy bands. Table IV summarizes some properties of available semiconductor detectors [56-59].

The principle of operation of solid-state detectors is based on the electron-hole pairs creation in the valence band of the semiconductor after the ionization of the atoms, and the proper drift of the electrons to a positive biased electrode and the holes to a negative biased cathode due to the application of relatively high DC voltage from anode to cathode. Measuring the charge collected in both electrodes, the total number of electron-hole pairs might be obtained. Ideally, in absence of recombination inside the detector, this number is proportional to the total energy deposited by the photon in the solid-state detector. Since the ionization energy necessary to create an electron-hole pair is material specific, the energy deposited by the photon could be calculated multiplying the number of generated electron-hole pairs by the energy of ionization [56-59].

In the recent years appeared new materials such as hybrid lead triiodide perovskites and Thallium bromide (TlBr) as promising materials for use as a direct gamma-ray detector for nuclear medicine applications, especially for PET. Due to their massive and cheap production capabilities of perovskites and the very high detection efficiency of TlBr, they are getting the interest of researchers for big areas X-ray detection applications and small animal PET scanners respectively [60,61].

Table IV. Summary of properties of some semiconductors for gamma-ray detection [56-59].

Semiconductor	Density [g/cm^3]	Z_{eff}	E_{gap} [eV] @ 300 K	X_0 [cm]	Mobility [cm^2/Vs] (e^- / h^+) @ 300 k
Si	2.33	14	1.12	9.37	1350 / 480
Ge	5.33	32	0.67	2.30	3900 / 1900
CdTe	5.85	48,52	1.44	1.52	1100 / 100
CdZnTe	5.81	48,30,52	1.6	-	1000 / 50
HgI2	6.36	80,53	2.13	1.17	88 / 4.1
GaAs	5.3	31,33	1.43	2.29	8500 / 400

The use of solid-state detectors for hard X-ray and soft gamma ray imaging cameras and spectrometers has exploded since early 2000 [62-65]. From Compton cameras for nuclear security [66], to anisotropic dosimeters based on pixelated silicon detectors [67]. In the case of PET, and more specifically human brain PET scanners, the results of a first pre-clinical PET scanner based entirely in planar CdTe detectors are presented in [68]. The scanner is based on the stack of single planar CdTe detectors of 2 x 4 x 7.5 mm^3 with a

trans-axial size of 2 x 4 mm^2. Under tests, the timing resolution was 6.0-6.8 ns FWHM (450 keV threshold), and the best energy resolution for the 511 keV energy range was 4.1 % FWHM, which is considerably better than the scintillator plus photodetector PET counterparts which ranges from 10 to 20 %. In fact, it shows a spatial resolution of 2.6 mm FWHM for a 1-mm diameter ^{18}F point source moved axially through the field of view (FOV).

Additionally, a PET prototype based on CdZnTe detectors for high resolution mouse brain imaging was presented at [69]. Although energy resolution was originally of 6 % at FWHM, it could be improved to 2% with a detector bias of 2000 V/mm after depth-related corrections. Moreover, another interesting feature of this design is that the electric field inside the detectors is tangential to the circular field of view of the scanner which makes the detectors orientation fully compatible with magnetic resonant imaging systems.

For PET scanners, the quality (resolution and contrast) of the images and the sensitivity are the most important figures of merit since both are related to the health of the patients. The better image quality, the higher the chances of early tumour detection, and the higher the sensitivity, the lower the radiopharmaceutical dose to be injected to the patient. Therefore, to compete with scintillator crystals, moreover much better image resolution, semiconductor-based PETs should provide a reasonable efficiency compared to current scintillating crystals. Table V summarizes the radiation absorption properties of some solid-state detectors and compares with a BGO crystal.

Total sensitivity of the full scanner depends on several factors such as the semiconductor material, the total field of view, the total detector volume and axial length, and the energy threshold for image reconstruction among others. Figure 3 shows a comparison plot of sensitivity versus spatial resolution of some scintillator-based and semiconductor-based small animal PET scanners for spatial resolutions below 2 mm [71-82].

Table V. Photon cross sections (linear attenuation coefficients) in semiconductor detectors and BGO scintillator crystal at characteristic energies for PET [70].

Material	Energy [keV]	Compton [cm^{-1}]	Photoelectric [cm^{-1}]	Total attenuation [cm^{-1}]	Mean free path [mm]
Si	27.5	0.347	3.542	4.241	2.4
Si	140.5	0.310	2.0E-2	0.350	28.6
Si	511	0.200	4.1E-4	0.202	49.5
CdTe	27.5	0.570	154.4	159.7	0.06
CdTe	140.5	0.614	3.223	4.148	2.4
CdTe	511	0.415	9.1E-4	0.534	18.7
CdZnTe	27.5	0.570	150.3	155.5	0.06
CdZnTe	140.5	0.613	3.052	3.965	2.52
CdZnTe	511	0.413	8.6E-2	0.525	19.0
Ge	511	0.402	1.8E-2	0.433	23.1
$Bi_4Ge_3O_{12}$	511	0.509	0.396	0.963	10.4

Left-top corner of the plot allocates the best spatial resolution and sensitivity scanners. Most of the semiconductor small animal PET have a spatial resolution below 1 mm and a comparable sensitivity compared to scintillator-based PET counterparts. Therefore, these results for most-demanding resolution PET scanners show that semiconductor detectors, specially Cadmium Telluride and Cadmium Zinc Telluride detectors, are solid

alternatives for PET detectors, for whole body, human brain, or small animal hybrid PET/CT and PET/MR scanners.

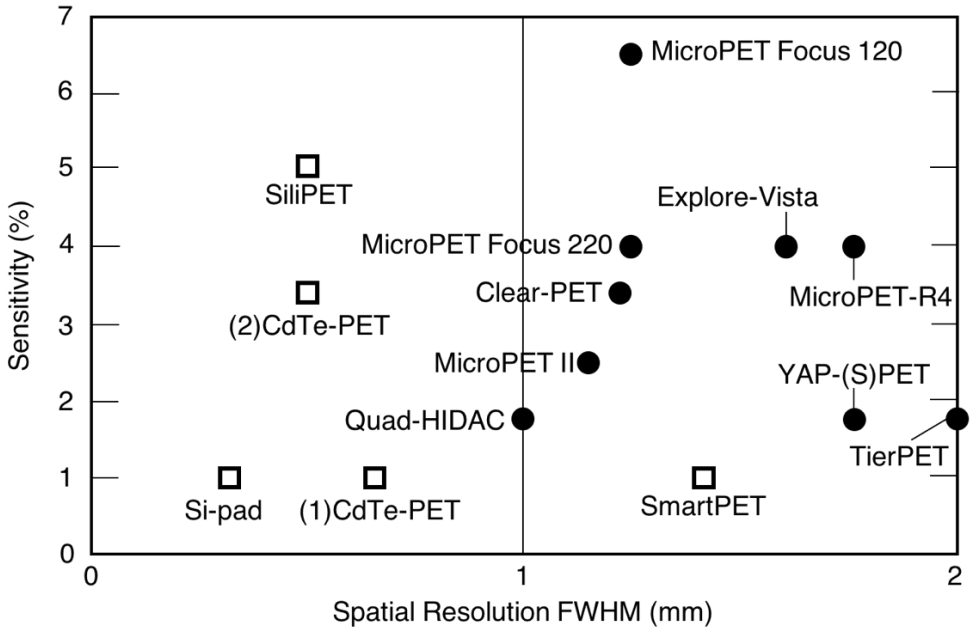

Figure 3. Comparison of the performance of some scintillator based (solid circle) and semiconductor based (hollow square) small animal PET scanners with spatial resolution below 2 mm. Data from CdTe-PET (1) and (2), Si-pad, SmartPET, SiliPET, YAP-(S)PET, Quad-HIDAC, TierPET, Clear-PET, Explore-Vista are obtained from [71-80] respectively. Data from MicroPET models are obtained from [81] and research MicroPET II from [82].

Additionally, the potential drawback of the semiconductor detectors – their limited quantum efficiency at medium (140 keV) and high (511 keV) gamma-ray energies, for thin detector substrates – can be bypassed by using detectors in geometries like the Voxel Imaging PET (VIP) where 4 cm of radiation detector offers 80 % absorption of all photons inside the FOV [83]. The design of the human brain VIP PET scanner would overcome the sensitivity limitation and improve the spatial resolution due to small detector voxel size and superb scattered photons rejection.

Chapter 3

The Voxel Imaging PET pathfinder project and scanner

An ideal PET detector should provide the following information: the exact position of the interaction of the 511 keV gamma photon inside the detector, the energy deposited in that point-like voxel, and the time stamp when the event occurred. With these three basic data, the line of response reconstruction algorithm can match back-to-back photons and generate "golden" LORs, assuming no scatter process has occurred. The image resolution would be limited by the collinearity of the positron annihilation process inside the organ under evaluation.

In real scanners, the loss in the image quality is due to uncertainties in the generated LORs. If detectors have a limited energy resolution, photons which have undergone a Compton scattering before reaching the radiation detector are accepted for the LOR reconstruction algorithm and slightly deviated LORs are obtained. Consequently, the image of a point-like source will be spread to a sphere of a radius that depends on the detector's energy resolution. Additionally, the spatial resolution due to the voxel size of the detector adds in quadrature to this spreading.

In PET scanners with no need of time-of-flight information, the accuracy of the time stamp of the detector is used to discard detected uncorrelated photons. Due to the intrinsic limited time resolution, a coincidence time window should be established and any photon detection inside the window might be considered back to back photons. The probability to evaluate erroneous LORs due to random coincidences increases with the width of the window and the activity of the radioactive source (or dose injected to the patient). As indicated, random coincidences will degrade the quality of the image by increasing the noisy background and reducing the contrast of high and low activity regions over average activity background.

The aim of Voxel Imaging PET pathfinder project is to overcome all these limitations by a novel geometry design of a PET scanner based on pixelated Cadmium Telluride detectors. The original geometry proposed for VIP PET is shown in Figure 4. The complete detector ring has an inner radius of 21 cm and an axial length of 25.4 cm for human brain static scanning. It is filled with Cadmium Telluride material segmented into voxels of 1x1x2 mm^3 approximately that are connected to an independent pixel readout electronics each. The trans-axial length of the detection ring is 40 mm which captures 70 % of the 511 keV single photons. The ring is composed of 66 trapezoidal sectors such that the design is seamless so better image and sensitivity will be available. Every sector is realized with four

detector modules which consists on 30 detection layers stacked as shown in Figure 4. Note that the trapezoidal shape of the sectors comes from the trapezoidal design of the CdTe detectors in every detector layer. Every detector has a thickness of 2 mm and is connected to a dedicated VIPPIX readout ASIC via flipchip process. The physical CdTe detector is segmented into 100 pixels electrically at the anode such as that every pixel is connected to an individual and independent readout pixel front-end electronics to achieve best spatial, timing, and energy resolution.

Every layer has 800 independent CdTe equivalent detectors of an approximate size of 1x1x2 mm^3. With 120 layers per sector and 66 sectors, the complete detector ring composes of 6.336.000 of these independent equivalent CdTe detectors. Such an extreme granularity in such small volume provides sufficient spatial resolution to approach the physical limits of PET detectors.

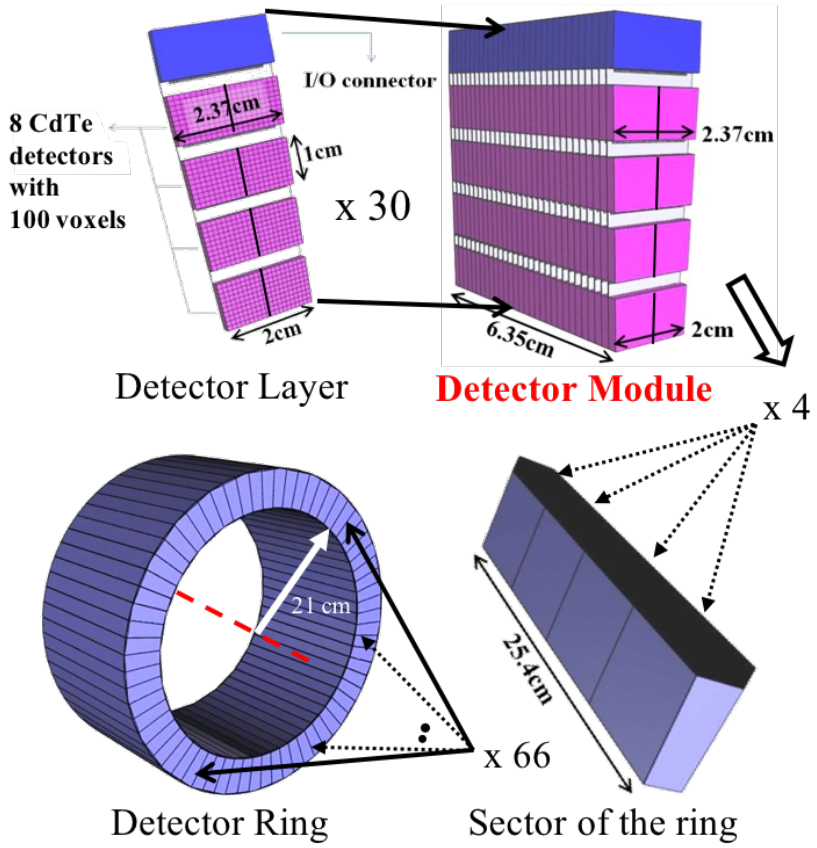

Figure 4. Geometry of Voxel Imaging PET Scanner [148].

Cadmium Telluride detectors can provide excellent energy resolution at room temperature [84]. Provided a proper high voltage bias, 2 mm-thick detectors can achieve 1-2 % FWHM resolution for 511 keV peak. This limit sets the acceptance energy window within which photons did not suffer any Compton scattering prior to the detection. For 511 keV photons, an energy loss of 1% in the interaction deviates the photon by 8 degree approximately [85]. A rough calculation assuming that in all the annihilations one of the photons undergoes a Compton scattering of 8 degree shows that the upper limit of VIP's

spatial resolution is 10 mm FWHM approximately. The expected effective error on the spatial resolution for human brain size scanner is in the order of 1 mm according to physical simulations in [148].

The design of VIP PET was first presented at [83] with initial simulation results based on particle physics-oriented software [86]. Further simulations in terms of counting capabilities and image quality have been performed to identify the limits and the advantages of the VIP geometry versus scintillator crystals-based human brain PET and small animal high resolution PET scanners [146].

3.1 Summary of article "Simulation of the Expected Performance of a Seamless Scanner for Brain PET Based on Highly Pixelated CdTe Detectors"

The aim of this work is the evaluation of the design of a non-conventional geometry PET scanner, the Voxel Imaging PET scanner, based on pixelated room-temperature Schottky Cadmium Telluride detectors that fill seamlessly a detection ring with a volumetric density of approximately 450 channels/cm^3 completing a total of 6336000 independent pixels what provides more than 2x10^{13} potential lines of response.

The sensitivity, the scatter fraction, the counting rate capabilities, the spatial resolution, and the image quality have been evaluated by computer simulation using the Geant4-based Architecture for Medicine-Oriented Simulations (GAMOS) [86], following recommendations of the NEMA NU 2-2001 standard for whole body and brain scanners [87], and the NEMA NU 4-2008 standard for small animal high resolution and small field of view PET scanners [88].

3.1.1 Description of the VIP scanner

The geometry of VIP scanner based in Figure 4 is explained. Every Cadmium Telluride detector of 10 x 10 x 2 mm^3 with 100-pixels are bump-bonded to a pixelated readout ASIC to form a hybrid detector with 100 independent CdTe voxels of 1 x 1 x 2 mm^3 in the inner radius and 1 x 1.185 x 2 mm^3 in the outer radius due to the trapezoidal shape of the detector module as shown in Figure 4. Original design contemplates a thinning process of the ASICs down to 50 μm thickness to reduce Silicon dead material in the path of the gamma rays. The ASIC-CdTe hybrid detector is glued to a multilayer flexible printed circuit board of 50 μm thickness with a 15 μm thickness double-side tape. An attenuation of less than 2 % of CdTe's absorption is due to all dead material in the path of gamma radiation.

Detector module is obtained by stacking up to 30 detection layers. The bottom side of every layer is provided with high voltage pads to bias the CdTe detectors right underneath. On this way, the electric field in the detectors is parallel to the detector ring axis. In a potential PET/MR system, such electric field would be parallel to the magnetic field of the MRI system what makes this geometry theoretically 100 % compatible with simultaneous PET and MRI scanning.

The original specifications of the ASIC for VIP detectors were the following: the ASIC should be composed of 100 independent self-triggered pixel readouts, or "smart pixels", that should provide the energy of the photon interaction with 10-bit resolution with a minimum

energy trigger equivalent to 20 keV. Pre-amplification and shaping should be applied in the front-end to lower the noise, and analog-to-digital conversion should start after the peak time of the shaper. After digitalizing the energy, a pixel reset must be applied with a dead time no longer than 130 μs. Additionally, the time information should be provided by the ASIC digital controller with a resolution smaller than 1 ns.

Although the ROIC can provide excellent time stamp and energy resolution for a given charge injection, the multiple variables in the CdTe detector such as biasing voltage, mobility of electrons and holes, charge sharing, trapping limit both energy and time resolutions. At room temperature and at 1000 V/mm bias, an energy resolution of 1.57 % FWHM was obtained with 2 mm thickness planar detectors with an active area of 2 x 2 mm^2 surrounded by a 1 mm wide guard ring [89]. Additionally, a direct measurement of the coincidence time resolution in [90], shows that for energy close to the 20 keV energy trigger threshold, a time coincidence window of 20 ns is needed to detect 70 % of the photon pairs.

Considering the working principle of the ROIC and the performance of CdTe detectors at room temperature and -1000 V/mm bias, the specifications of the VIP detector ring used for simulations are summarized in Table VI.

Table VI. VIP detector ring parameters used in GAMOS simulations.

Material	Cadmium Telluride
Axial length	25.4 cm
Inner radius	21 cm
Outer radius	27 cm
CdTe interaction radial length	40 mm
Energy resolution	1.57 % FWHM
Dead time per voxel	130 μs
Measuring time per voxel	20 μs
Coincidence time	20 ns
CdTe voxel size	1 x 1 x 2 mm^3
Readout Chip thickness	50 μm
Printed circuit board thickness	50 μm
Glue thickness	15 μm

3.1.2 Simulations

Hit entries of the data are characterized by the (x, y, z) position of the center of the corresponding voxel, the collected energy, and the time stamp. The coincidence searching algorithm processes the list mode data to group consecutive hits lying inside a coincidence time window of 20 ns. Charge sharing, and secondary particles generated in the detector are considered by grouping energies of hits whose reciprocal distance is below 1.45 mm and assigning the energy-weighted centroid as the new position of the grouped hits.

The high granularity and high energy resolution of the VIP scanner allows the reconstruction of events where one of the photons undergoes one Compton scattering inside the detector ring before the final photoelectric detection [91]. Additionally, with more than one Compton interaction it is possible to estimate the right line of response with certain level of confidence that depends on the number of hits, the energy deposited per hit, and the applied

algorithm. Five different algorithms are evaluated to choose the right algorithm to use in the analysis aiming for the maximization of the purity of the Compton reconstructed sample and the selection efficiency. The best trade-off is obtained by choosing the pixel with the smallest radius (pixel closer to the source) as the first interaction so the one defining the LOR.

VIP scanner has been simulated in two conditions to study its robustness: based on the predicted performance as nominal condition, and lowering the performance of the detectors by reducing the energy resolution to 5 % FWHM, doubling the amount of dead material, and "killing" 1 % of the total number of channels randomly distributed. Additionally, to validate the simulation method, the ECAT high resolution research tomograph (HRRT) has been simulated and results are compared to the published data [92].

3.1.3 Results

Scatter Fraction: The purpose of the Scatter Fraction test is to measure the relative system sensitivity to the scattered radiation. The NEMA document defines the SF as the ratio of scattered events to total events, which are measured at a sufficiently low counting rate such that random coincidences, dead-time effects, and pileup are negligible. The scatter fraction of nominal VIP design is **3.95 %** and **0.73 %** for NEMA NU 2-2001 and NEMA NU 4-2008 standards respectively. The VIP design with 5 % FWHM energy resolution CdTe detectors shows a scatter fraction of 11.26 % for human brain standard due mostly to the dramatic increase of energy resolution.

Counting Rate: The purpose of the counting rate performance test is to measure the effect of the system dead time and the amount of random coincidence events at several levels of source activity. Main figure of merit, the noise equivalent count (NEC) rate, provides the count rate at which the signal-to-noise ratio with and without scatter and random events match. The values of the peak NEC rate and the true events count rate of nominal VIP design are presented for both standards. Due to the very efficient scatter rejection and the high granularity, counting results are excellent.

Sensitivity: The sensitivity of VIP scanner is simulated as well following both NEMA standards. The activity of the sources is 5 MBq and 1 MBq for NU 2-2001 and NU 4-2008 respectively to assure counting losses due to pile up below 1% and random event rate lower than 5% of true coincidence rate. The resulting sensitivities are **14.37 cps/kBq** and **21 cps/kBq**, compatible with the average performance of commercial PET scanners.

Spatial Resolution: Spatial resolution is simulated with point sources in different locations inside the field of view to estimate the radial, tangential, and axial resolution separately. At least 105 coincidences must be collected in every measurement and single-slice re-binning technique (SSRB) and filtered back-projection image reconstruction algorithms must be used. Following the instructions of human NEMA NU 2-2001 standard, the spatial resolutions FWHM of the reconstructed images at 10 cm radial offset are **0.7 mm**, **0.9 mm**, and **1.9 mm** approximately for radial, tangential and axial measurements. Following small-animal PET standard, at 10 cm radial offset and at ¼ axial FOV, the resolutions are 0.7 mm, 1.5 mm, and 1.5 mm approximately for radial, tangential, and axial measurements.

Image Quality: The image quality of VIP PET scanner is evaluated following NEMA NU 4-2008 standard since results are closer to small-animal PET than current scintillator-based commercial PETs. The standard requires placing a special image quality phantom (Figure 5)

in the center of the FOV of the scanner with no surrounding material. Additionally, since the scatter fraction of VIP scanner is one order of magnitude lower than current high-resolution PET, we performed simulations where the image quality phantom is immersed in a 150-mm radius water sphere mimicking human brain scattering. Images were reconstructed with FBP algorithm without attenuation, scatter, nor random corrections. The quantification parameters proposed by NEMA are calculated and presented. Figure 6 shows the reconstructed image of the phantom in air (left), and in water (right) where we have hot rods (a,d), cold inserts (b,e), and uniform regions (c,f).

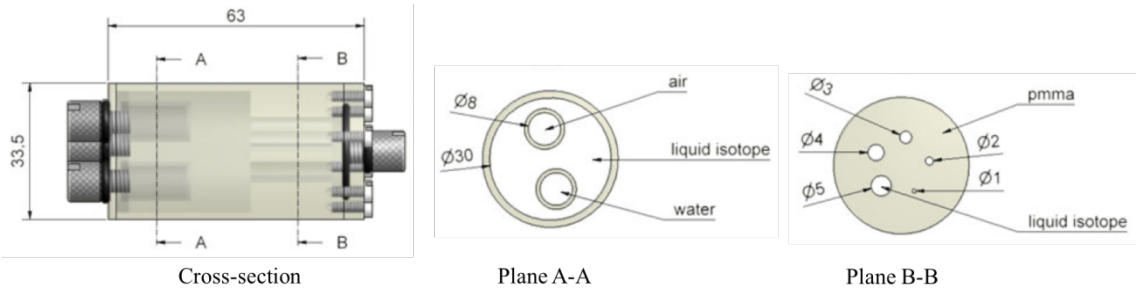

Figure 5. NEMA NU4-2008 phantom geometry (all dimensions are in mm) [88].

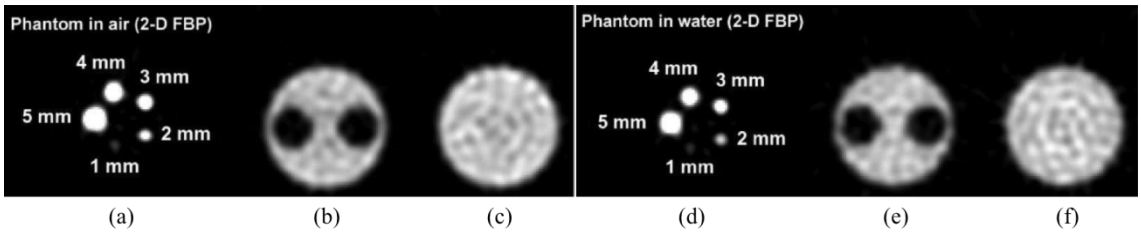

Figure 6. Reconstructed Images of NEMA NU4-2008 phantom in air (left) and inside a 150-mm radius sphere filled with water (right) [148].

3.1.4 Conclusions

The crack-free geometry of the VIP scanner provides a sensitivity of 14.37 cps/kBq, a scatter fraction of 3.95 %, a calculated NEC rate peak of 122 kcps at 5.3 kBq/mL, a 0.7 mm FWHM radial and tangential resolution, and a 1.3 mm FWHM axial resolution for human brain size standard. Due to the high purity acquired data, the number of millions of coincidences to reconstruct high signal to noise ratio images is significantly smaller than the needs of actual PET scanners. Therefore, with the counting capability, the high sensitivity, and the low volume of scanned data, VIP PET scanner could work either with one order of magnitude lower intake dose to the patients and traditional scan times of tens of minutes, or with scan times of tens of seconds using the peak activity of 5.3 kBq/mL.

Compared to high resolution small-animal PET scanners, similar performance is obtained despite the much larger field of view of VIP PET. Obtained results encouraged the challenging development of a VIP scanner prototype to validate such excellent performance.

Chapter 4

Cadmium Telluride Detectors for PET

The theoretical energy resolution of CdTe can be calculated from statistical fluctuations in the number of electron-hole pairs and the Fano factor (F)[30]. By using = 4.5 eV and F = 0.15, the theoretical limit (FWHM) is 200 eV at 10 keV, 610 eV at 100 keV, and 1.5 keV at 600 keV [93], if we could neglect electronic noise. These resolutions are very attractive for applications in astrophysics, where precise determinations of the central energy and the profile of X-ray and γ-ray lines are crucial. For obtaining the ultimate energy resolution from the CdTe and CdZnTe detectors, collecting full charge and the information given by the transit of both electrons and holes is important. In order to obtain a FWHM of 700 eV at the 122 keV line from ^{57}Co, a bias voltage of 1400 V should be applied for a detector with a thickness of 0.5 mm for $\mu_h\tau_h = 1 \times 10^{-4}$ cm^2/V [93]. The thin CdTe device has an advantage over the thick one because sufficient bias voltage for full charge collection can be easily applied. Detectors with very low leakage current that allow such a high bias voltage have been developed by several groups thorough the use of diode structure either by a blocking electrode or PIN structure [93-95].

Nowadays, two different type of CdTe detectors are available technologically: detectors with different electrode metal work function that form a Schottky barrier; and detectors with the same electrode metallization, thus having a pure ohmic behaviour. Figure 7 shows two biasing configurations (holes collection through the cathode, and electrons collection through the anode), and three different electrode metallization (Indium – CdTe – Platinum, Platinum – CdTe – Aluminium, Platinum – CdTe – Platinum) of commercially available Cadmium Telluride detectors [96].

Schottky CdTe detectors perform much better than ohmic detectors in terms of leakage current (also known as dark current) and energy resolution since they can be biased with much higher voltage. Nevertheless, due to the high electric field, a time-dependent space charge buildup occurs at the blocking contact that decreases the detector's charge collection efficiency [97-99]. A common solution to depolarize Schottky detectors is cyclic bias reset. The detector's bias voltage is reset to zero or even in forward bias region during certain time window from consecutive active high voltage pulses. The width of the reset window must be optimized for the application, the applied voltage, and the required resolution.

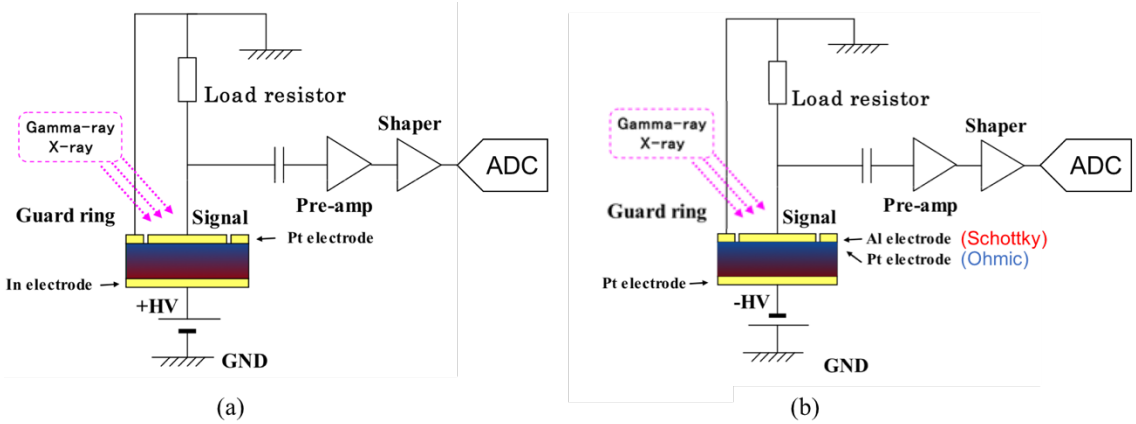

Figure 7. Standard metallization and readout electrical schemes of CdTe sensor: Schottky with holes collection (a), Schottky with electrons collection (red b), and Ohmic with electrons collection (blue b) [96].

Although ohmic detectors have a leakage current under control with low bias voltages, it is usually still some orders of magnitude higher than Schottky detector counterparts. For given detector thickness, such small bias introduces a wide uncertainty in the collected charge due to the low electric field and the associated long collection time. Charge collection efficiency depends strongly on the depth of the photon interaction inside the detector, especially when low bias voltage is applied. Therefore, for high resolution applications that require continuous operation with ohmic CdTe detectors, a depth of interaction (DOI) correction algorithm should be implemented. In [100], reaching resolution limits are demonstrated using DOI corrections in charge measurements.

The carrier transport performance of CdTe detectors has been reported in numerous publications due to the interest in high energy resolution and high stopping power room temperature solid-state detectors since the 70's [101-104 Mobility Tau in CdTe]. The mobility of electrons and holes depend strongly with Temperature in CdTe. Figure 8 shows the dependency of hole mobility (right) and electron mobility (left) with temperature of CdTe detector [105]. Note that electrons mobility decreases with temperature while holes mobility remains constant in the range of temperatures down to 230 Kelvin approximately. This effect in CdTe is mostly due to the different mobility limitation mechanism since electrons' mobility is limited by scattering while holes' mobility is limited by trapping [105].

It is well known that the lower the temperature, the lower the leakage current of the detector and the noise associated for a given bias voltage. Nevertheless, according to the mobility of Figure 8, the ratio of electron/hole mobility at lower temperatures is larger than at higher temperatures. This fact might result in a problem for timing and high energy resolution requirements where the charge of both carriers must be collected. The collection time and the associated electrical current provided by the CdTe sensors depend upon the depth-of-interaction. Figure 9 illustrates the detector response and the integrated charge in four different depths of interaction at room temperature (298 Kelvin) assuming electron and hole mobility of 1000 and 90 $cm^2/V{\cdot}s$ respectively, and a 2-mm thick detector biased at -2000 V.

Note that the charge collection curves reflect the dramatic change of the response of the planar detector with the DOI. In the case that a pulse shaping needs to be used after the

charge integration for higher energy resolution, a very long shaping time should be used in the shaper to avoid the distortion of the pulse.

As mentioned above, leakage current increases with temperature and bias voltage geometrically [106]. Figure 10 shows the leakage current of a planar detector for different bias voltages versus temperature. Small variations from room temperature to few Celsius degree might decrease the leakage of Schottky detectors two orders of magnitude while the mobility ratio increases a small percentage.

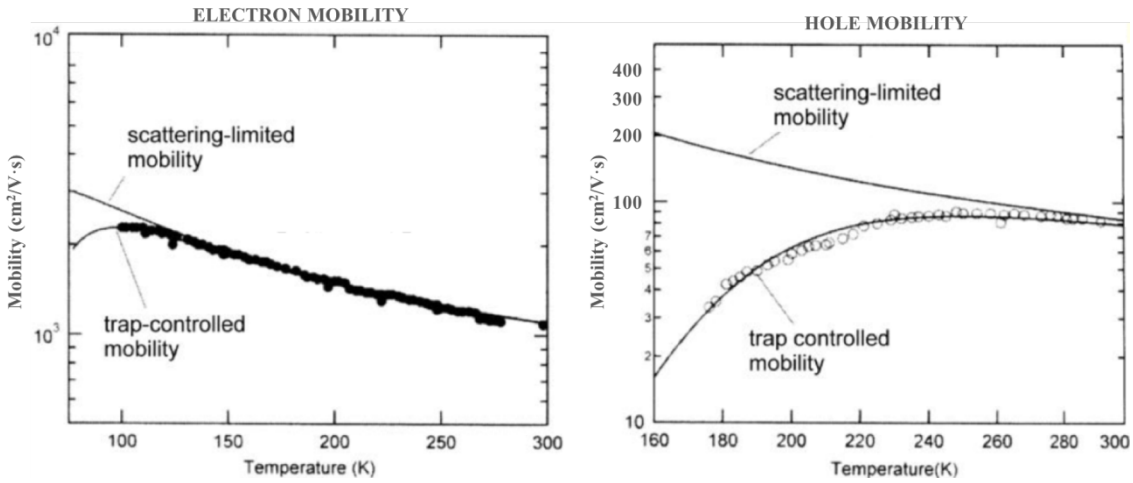

Figure 8. Mobility of Electrons (left) and Holes (right) versus temperature plots [105]. Straight lines follow theoretical scattering mechanism and fill circles and hollow circles represented measured data of electron and hole mobility respectively.

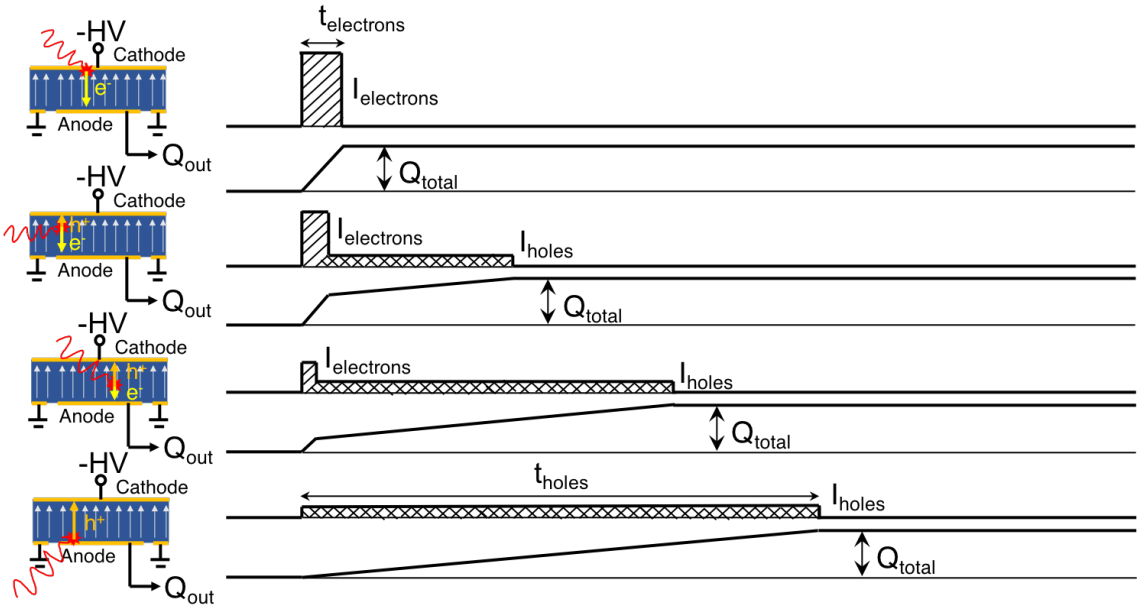

Figure 9. Charge injection performance of a CdTe detector with four different depth of interaction impact points.

Considering the performance of the CdTe detectors in terms of leakage current and charge collection ratio with the temperature, a desired temperature range of the VIP detector ring would be from -10 to +10 Celsius degree. In order to evaluate the actual performance of commercial CdTe planar detector with guard ring in such temperature range, energy and time resolution measurements were obtained and published in the second article of this thesis “Energy and coincidence time resolution measurements of CdTe detectors for PET”.

VIP scanner is based on pixelated Cadmium Telluride detectors. In semiconductor pixelated detectors a very interesting effect caused by the geometrical confinement of the electric fields with neighbouring pixels occurs. It is called “pixel effect” and it tends to shape the weighting field in the direction of the electric field such way that the contribution of electrons and holes versus the depth of interaction is no longer linear [107]. Figure 11 shows the dependency of the weighting field with the normalized depth for different pixel area and detector thickness ratio. The pixel effect is more acute with smaller ratios.

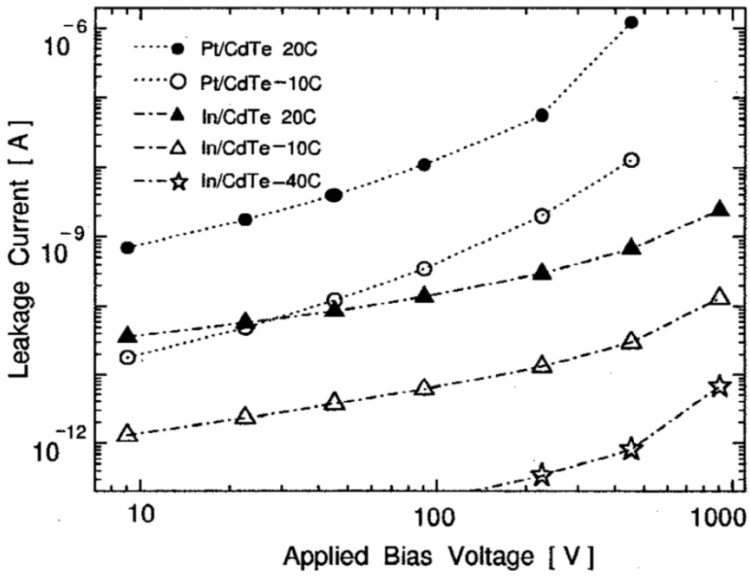

Figure 10. Detector Bias and Temperature dependency of CdTe Leakage current [106].

The consequence of the effect is an improvement of the spectroscopic resolution of the detector since electron transport is favoured for larger depth of interaction, as shown in Figure 12 where the spectroscopy of ^{241}Am is obtained with planar CdTe detector (a) and multiple electrode CdZnTe detector (b) of the same thickness with the same electronics [108]. Note that since the electron and hole mobility of CdTe (1100 and 100 cm^2/V·s respectively) and CdZnTe (1350 and 120 cm^2/V·s respectively) are similar, and both detectors have the same thickness and bias conditions, the comparison in Figure 12 and [108] stands. The reduction of the asymmetric long tail in the photopeaks of the measured spectra using multiple electrodes leads to better energy resolution in this case.

The performance of a pixelated CdTe detector of the same type, thickness and pixels size of VIP detector has been characterized at [109]. The energy resolution obtained with a commercial multichannel readout electronics show a spectroscopic resolution of 3.03 % at room temperature and -500 V/mm for the 122 keV peak of ^{57}Co. Such results are in

accordance with other published measurements that indicate a great potential of pixelated detectors for PET [110].

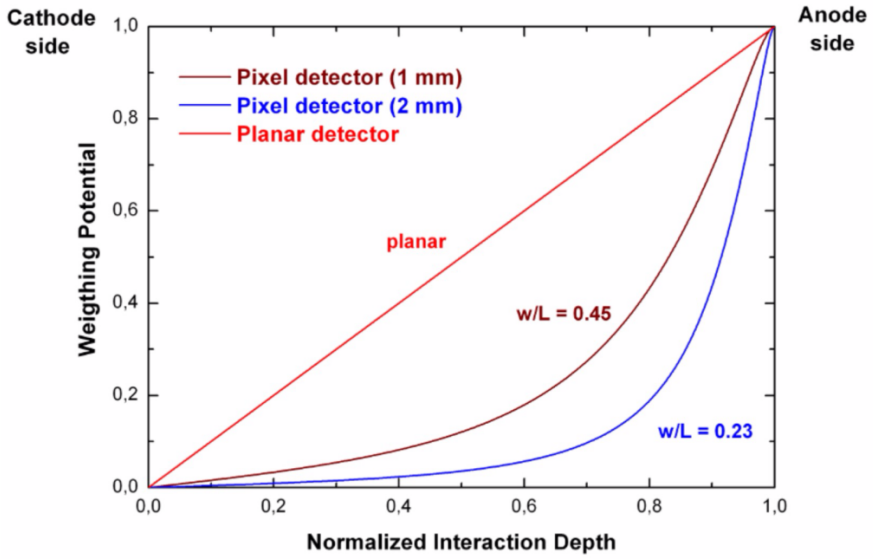

Figure 11. Weighting potential along the interaction depth for three ratios of pixel size over detector thickness [108].

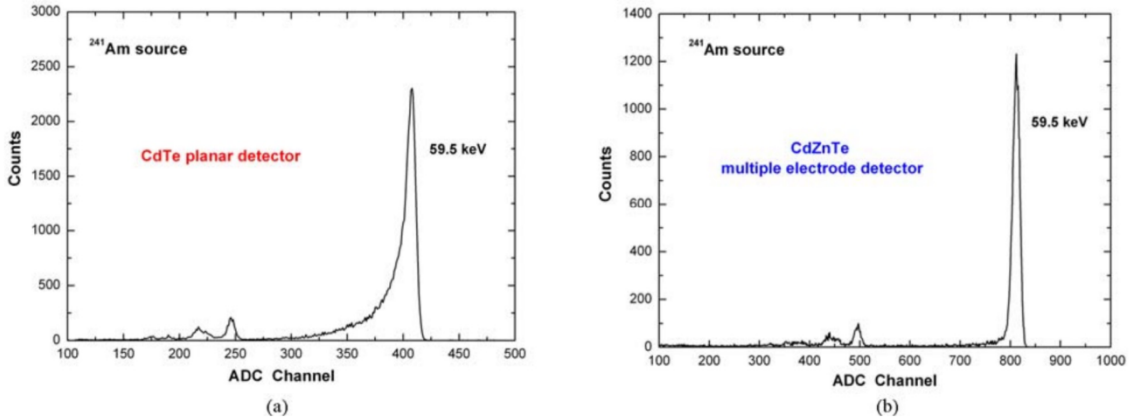

Figure 12. ^{241}Am spectroscopy obtained with a CdTe planar detector (a), and a CdZnTe detector with multiple electrodes (b) of the same thickness and biasing conditions obtained with the same electronics [108].

4.1 Summary of article "Energy and coincidence time resolution measurements of CdTe detectors for PET"

Based on the published excellent detection properties of Cadmium Telluride detectors [111-116], the design of VIP PET scanner was proposed, and simulations performed with GAMOS confirmed the great potential of VIP detector ring in terms of sensitivity, scatter fraction, image quality, spatial resolution, and counting capabilities.

To evaluate the limits of 2-mm thickness planar detectors in terms of time and energy resolution, a characterization setup based on commercial solutions was assembled. Electron collection Schottky CdTe detectors with Aluminium and Platinum contacts were used. The size of the single-channel detectors was 4 x 4 x 2 mm^3. The anode electrode is surrounded by a 0.95-mm width guard ring separated by 50 μm while the cathode covers completely the detector. Figure 13a illustrates the dimensions of the detector and Figure 13b shows a photography of the detector inside the commercial package.

Detectors are connected to a readout electronics using a small variation of the electrical scheme of Figure 7b. The anode electrode is directly connected to the input terminal of the charge sensitive amplifier without decoupling capacitor and load resistor since the DC bias condition is provided by the Pre-amplifier.

A commercial front-end solution from AMPTEK Inc. for particles detector readout is used [117]. The anode of the detectors was connected to an A250 pre-amplifier. The amplified output was doubled and connected to a commercial discriminator for trigger generation and to a A275 pulse shaper configured in a 5 poles configuration for superior energy resolution. The advertised energy resolution of the combination A250-A275 is 100 e^- RMS at room temperature and the rise time of the output of the preamplifier is 2.5 ns with 0 input capacitance. In theory, such a high bandwidth is almost one order of magnitude higher than the minimum collection time of electrons in the 2-mm thickness detector biased at -2000 V, which is approximately 20 ns considering a room-temperature mobility of 1000 cm^2/Vs. The peak time of the pulse shaper is designed to be 2.3 μs by the manufacturer. Assuming a hole collection at -2000 V, a total collection time of approximately 220 ns is expected. Having the peak time at one order of magnitude from the maximum rise time of the preamplifier ensures charge integration losses below 1% in a 5^{th} order pulse shaper [118]. The impact of this conversion gain in the spectroscopic resolution is much lower since only small percentage of events are based in full hole collection, losses due to trapping will dominate the energy resolution.

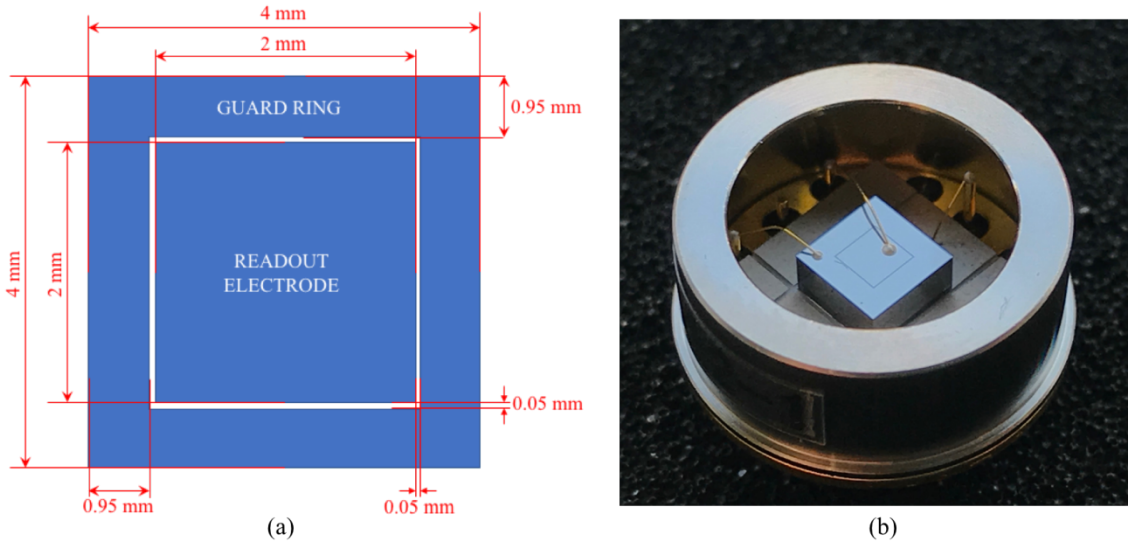

Figure 13. Dimensions and photography of the 2-mm thickness CdTe planar detector used.

4.1.1 Energy resolution measurement results

To evaluate the energy resolution of the planar detectors, a ^{22}Na radioactive source was used. The electrical scheme of the measurement setup is illustrated in Figure 14. Detectors are biased at -2000 V at -8 Celsius degree to lower the leakage current and improve the resolution. The charge from the detector is integrated in the AMPTEK pc250 board that integrates a preamplifier A250 with a gain of 36 mV/MeV for CdTe or 0.16 μV/electron. The output voltage is fed into two branches: a trigger generation branch composed by a 9 times amplification stage and a commercial pulse discriminator with 4 μs output pulse width with a threshold of 25 keV; and an energy measurement branch composed by a 2 times amplification stage and the AMPTEK pc275 board that composes of three pulse shapers with fifth order transfer function and a baseline restore IC. The shaped pulse is then fed into a peak sensing ADC enabled only during the duration of the discriminator pulse width.

Spectroscopy of sodium-22 shows a 511 keV peak with a FWHM width of 6 keV or 1.2 %. This result is compatible with state of art CdTe detectors and the manufacturer data.

4.1.2 Coincidence time measurements results

To measure the time difference of the detection of back to back photons of positron annihilation in PET, two identical detectors with identical readout electronics in a face to face configuration have been used. Figure 15 shows a photography of the measurement setup. Note that the radioactive source is placed in the middle of both boxes at the same distance of each detector.

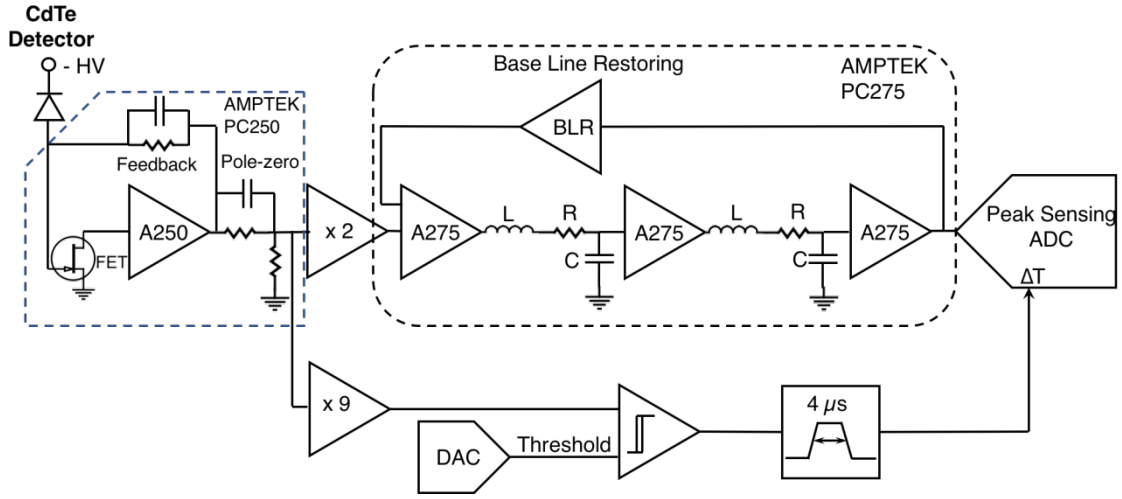

Figure 14. Electrical block diagram of the spectroscopy setup based on Amptek PC250 and PC275 readout electronics.

In this setup, the width of the output pulse of the signal discriminators is set to 200 ns to mimic the coincidence window to be considered a back to back coincidence. The

coincidence logic allows to measure both, the time difference with a commercial TDC, and the energy of both detectors with the peak sensing ADC used for spectroscopy. Coincidence energy discrimination was used to discard photons that underwent a Compton scattering.

A coincidence resolution of 6 ns FWHM was obtained for coincidence photons of minimum energy of 500 keV, i.e., basically only photoelectric interactions.

The measured energy resolution and coincidence time resolution are compatible with the state of art and outperforms some previous measurements with planar CdTe detectors [119 – 121].

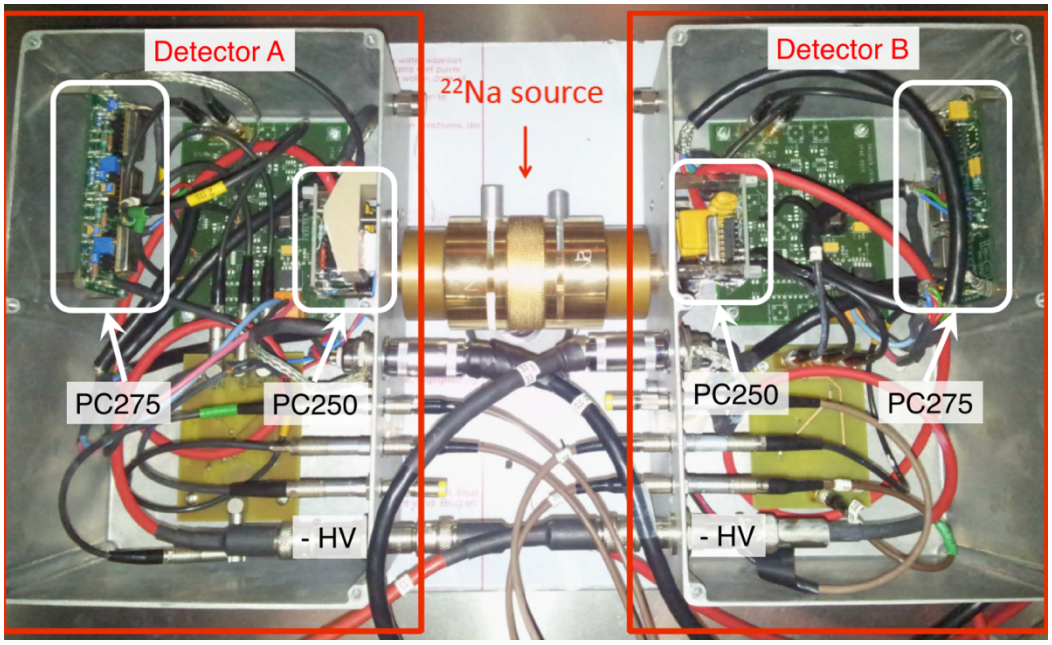

Figure 15. Illustration of the coincidence time measurement setup with two identical readouts in a face-to-face configuration [149].

Chapter 5

Readout ASICs for radiation detectors

The purpose of any radiation detector readout integrated circuit is to acquire the charge injected by the detector and to provide the magnitude required by the application. There are three main applications: imaging, spectroscopy, and time identification. Additionally, the combination of two of them is needed in specific applications.

In most of readout electronics, a charge sensitive amplifier is used as the first amplification stage where the charge – voltage conversion is accomplished. Figure 16 shows a generic electrical scheme of a charge sensitive amplifier (top) with the shape of the signals in every node (bottom). The current pulse from the detector is injected into the feedback capacitor since it offers the lowest impedance path compared to the feedback resistor and the equivalent input impedance of the amplifier - provided that the bandwidth of the amplifier is sufficiently high to follow the collection time of the detector. The pulse current integrated in the feedback capacitor generates a voltage pulse with a peak amplitude proportional to the deposited energy that can be used for any application, i.e., trigger generation and thus time stamp identification, photon interaction counting through pulse discrimination for imaging, or spectroscopic applications using the peak information of the pulse.

Readout ASICs for semiconductor detectors are divided into four main types: charge integration readouts and photon counting readouts for X-Ray imaging applications, readouts for spectroscopy applications, and ASICs for time of flight measurement applications.

Positron emission tomography scanners require readout electronics that provide, with excellent resolution, all three magnitudes from the sensor, i.e., the energy deposited by the photon, the interaction time stamp, and the interaction position inside the detector. Additionally, they must be based on self-triggered electronics due to the intrinsic random process of the positron emission inside the body. Based on the three different applications, i.e., imaging, spectroscopy, and timing, a review of available ASIC solutions for radiation detectors based on self-triggered electronics was performed and is reported here. The design of the VIPPIX ASIC combines features of all three types of readout ASICs optimized for just one application.

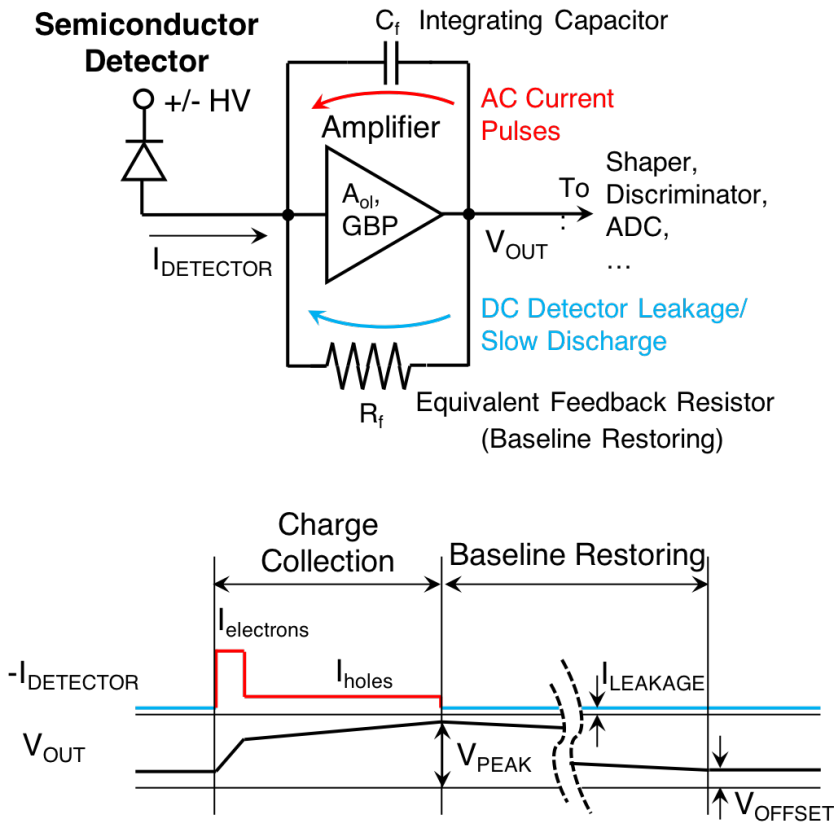

Figure 16. Generic block diagram of a first amplification stage for semiconductor detectors(top) and corresponding current and output voltage waveforms (bottom).

5.1 Photon Counting Readout ASICs

In photon counting readouts, the collected charge produced by each photon interaction is compared to a threshold. If the detected charge is above the threshold the counter is incremented. Since they perform a single bit analog to digital conversion, i.e., they register the validity of an event without energy information readout, they show perfect linearity and ideally unlimited dynamic range. Having more than one pulse discriminator allows to provide energy classification of the photon interactions. A small sample of most popular photon counting readout ASICs follows:

MEDIPIX2/3: Medipix chips family is developed at CERN in the framework of the Medipix collaborations (Medipix4 Collaboration just started in 2016). It is a readout ASIC for pixelated semiconductor detectors with a pixel pitch of 55 μm and 65536 pixels (256 rows and 256 columns). Figure 17 shows the block diagram of a Medipix3 pixel electronics. Every pixel is provided with a charge sensitive amplifier, two discriminators with adjustable offset compensation, two independent pseudo-counters, and a charge summing circuit to compensate the charge sharing in the detector. Additionally, it can operate in spectroscopic mode where counting is classified in different energy bins [122].

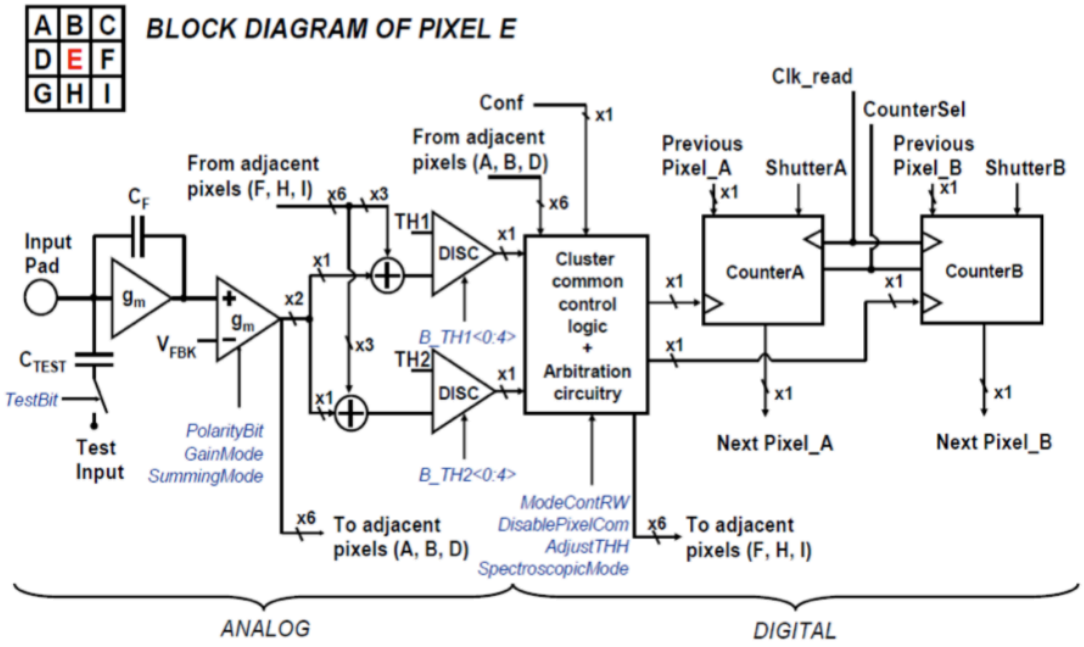

Figure 17. Electrical scheme of the pixel electronics of Medipix3 chip [122].

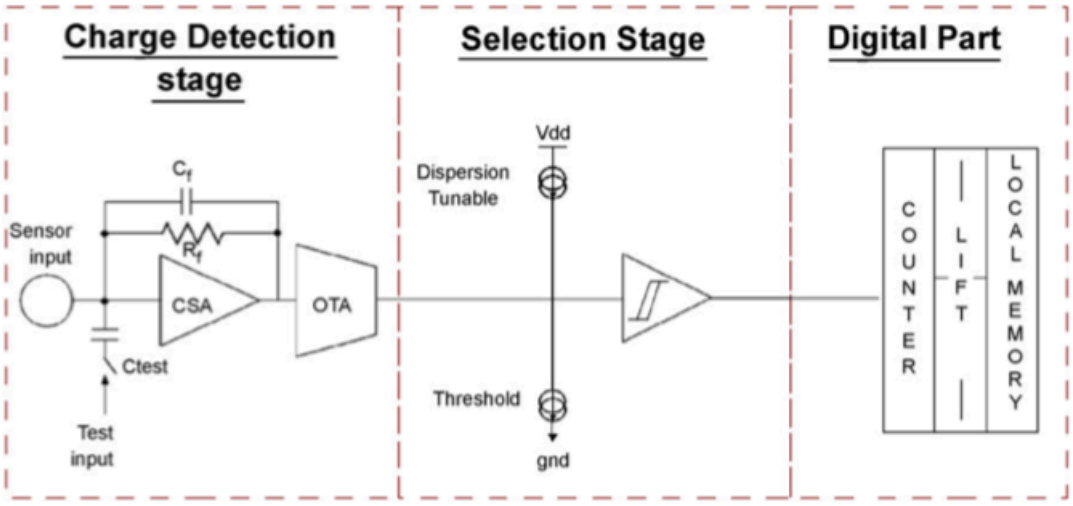

Figure 18. XPAD3-S pixel front-end electronics [123].

XPAD3: XPAD3 is a pixelated photon detector based on hybrid pixel technology that provides low noise data readout at high speed for synchrotron applications. It is designed in 0.25 µm IBM technology and contains 9600 pixels (130 µm×130 µm) distributed into 80 columns of 120 elements each. Its features have been optimized to fulfill a count rate capability up to

10+6 photons/pixel/s, a high dynamic range over 35 keV, a very low noise of 130e⁻ RMS, and a threshold adjustment well below 4 keV. Fast data readout below 2 ms/frame is achieved with an innovative architecture that makes possible the readout of the circuit during acquisition while preserving the precise setting of the thresholds all over the pixel array. The XPAD3 circuit can be bump-bonded with Si, CdTe, or GaAs sensors to optimize its detection efficiency at high X-ray energies and it can be tiled together to form big area detectors with an 8 cm×12 cm sensitive area [123]. Figure 18 shows the block diagram of a pixel front-end electronics of XPAD3-S ASIC.

PILATUS: In 1998, the Swiss Light Source (SLS) synchrotron detector group and the Paul Scherer Institute (PSI) chip design core team joined efforts to develop a large area photon counting chip for X-ray experiments at SLS. The Pilatus II chip was a 60 x 97 pixel matrix with a 172 μm pitch, using a commercial 0.25 μm CMOS process. As shown in Figure 19, each pixel cell comprises a preamplifier, with high and low gain setting, a shaper, and 6-bit adjustable single threshold discriminator, followed by a 20-bit counter. The most recent update is Pilatus III chip with retriggering technology with adjustable dead time to detect successive photons arriving within the same readout cycle and decrease the pile-up effects [124]. At PSI, an Extremely high rate detector (EIGER) and a Microstrip system for time resolved experiments (MYTHEN) have been developed for synchrotron applications [125].

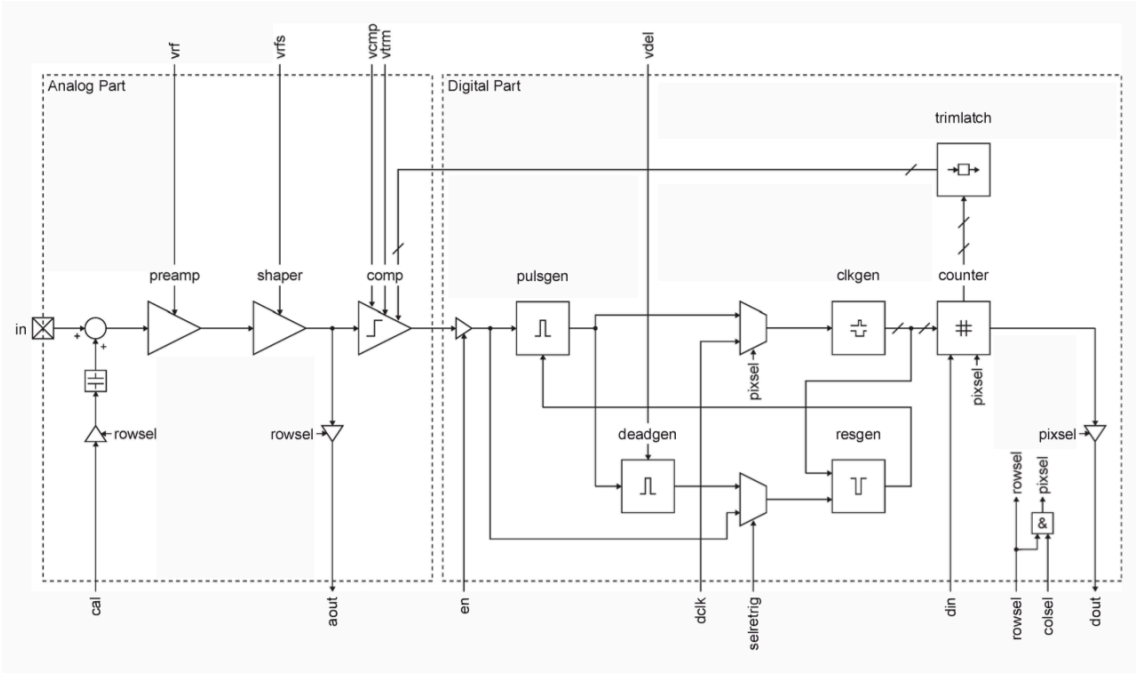

Figure 19. PILATUS3 pixel block diagram [125].

ChromAIX2: The ChromAIX readout ASIC family is developed at Philips Research Europe. The new version ChromAIX2 delivers count-rates exceeding 15 Mcps/pixel with a noise performance of approximately 260 e⁻ RMS. It has an isotropic pixel pitch of 500 μm in an array of 22 x 32 pixels and is tile-able on three of its sides. The pixel topology is illustrated in Figure 20 and consists of a two-stage amplifier (CSA and Shaper) and a number of test

features allowing to thoroughly characterize the ASIC without a sensor. A total of 5 independent thresholds are also available within each pixel, allowing to acquire 5 spectrally distinct measurements simultaneously. The ASIC also incorporates a baseline restorer to eliminate excess currents induced by the sensor (e.g. dark current and low frequency drifts) [126].

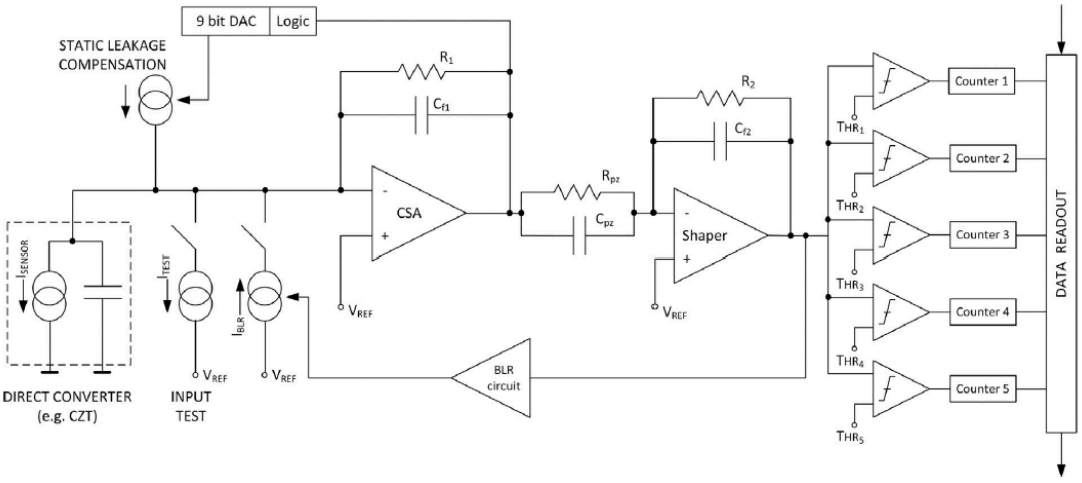

Figure 20. Simplified block diagram of pixel of ChromAIX2 ASIC [126].

ERICA: ERICA is an energy-resolving photon-counting readout ASIC for in-line cameras for non-intrusive inspection applications and potentially spectral CT imaging systems implemented in a commercial 0.25 µm CMOS process at IFAE, Spain. The ASIC is composed of a matrix of 8 × 20 pixels controlled by a global digital controller and biased with 7 independent digital to analog converters (DACs) and a band-gap current reference. The pixel analog front-end includes a charge sensitive amplifier with 16 mV/ke- gain and dynamic range of 45 ke-.

As shown in Figure 21, every pixel has programmable pulse width, an adjustable constant current feedback resistor, a linear test pulse generator, and six discriminators with 6-bit local threshold adjustment. The pixel digital back-end includes the digital controller, 8 counters of 8-bit depth, half-full buffer flag for any of the 8 counters, a 74-bit shadow/shift register, a 74-bit configuration latch, and charge sharing compensation processing to perform the energy classification and counting operations of every detected photon in 1 µs. The pixel size is 330 µm × 330 µm, consumes 150 µW, and performs an equivalent noise charge (ENC) of 90 e- RMS connected to a 1-mm thickness matching CdTe detector biased at -300 V with a total leakage current of 20 nA [127].

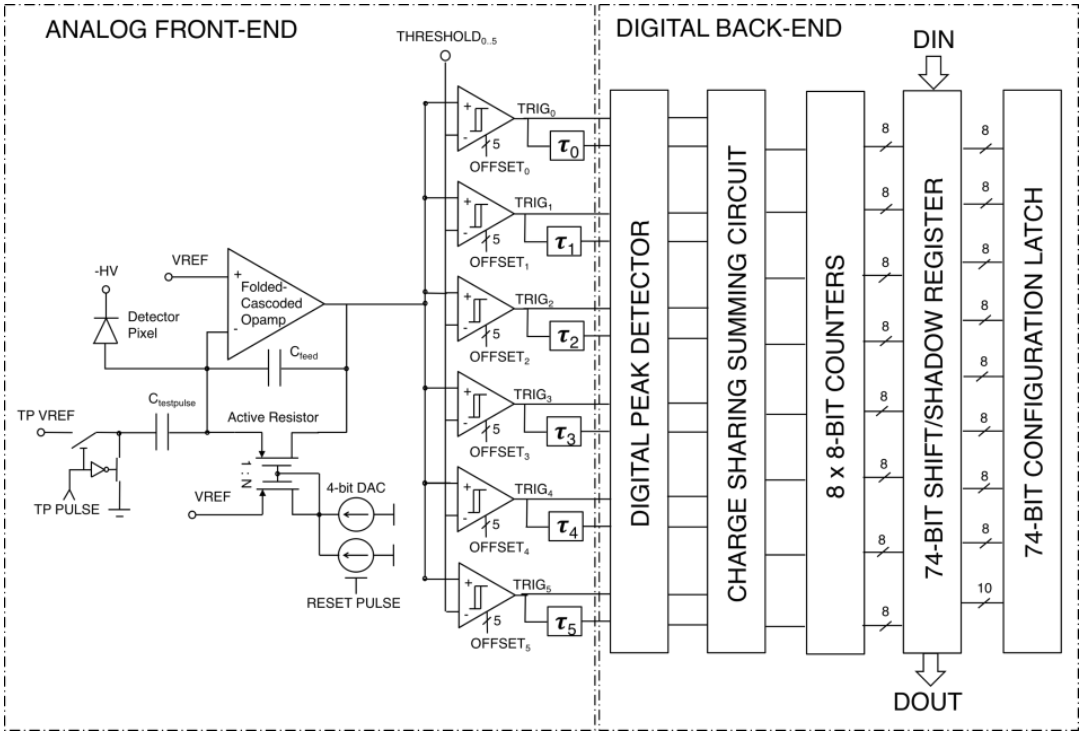

Figure 21. Block diagram of pixel electronics of ERICA ASIC [127].

5.2 Spectroscopic Readout ASICs

Spectroscopic front-end electronics are designed to provide excellent spectral resolution independent of the operating conditions of the radiation detectors such as their leakage current and their charge collection efficiency. Therefore, in combination with the detectors, they should have a very low equivalent noise charge (ENC). Common architectures include pulse shaping of the preamplifier's output voltage pulse to reduce the contribution of high frequency noise due to the wide bandwidth of the amplifiers and low frequency noise from the leakage current of the detector. Since the energy information of every photon interaction must be readout and the nature of the application is random, a trigger generation is available for most of the ROICs. The energy of the photon is obtained using two different approaches: in most accurate front-ends the value of the peak of the shaped signal is measured either internally or with external ADCs; a simpler approach is to measure the time-over-threshold of the output signal from the preamplifier which is linear with the injected charge to a first order of approximation. A set of most popular readout ASICs used for spectroscopy applications follows:

VATA: The VATA ROICs are applications specific (ASICs) originally designed for satellite instrumentation in space for X-ray and Gamma-ray spectroscopy. VATA family offer ICs with analog outputs but also with integrated analog-to-digital converters (ADCs) for fully digital readout of x-ray and gamma-ray detectors. The VATAs are ideal for the readout of cadmium zinc telluride (CZT), cadmium telluride (CdTe), silicon pads and strips, and large area avalanche photodiodes (APDs) with scintillators. The VATAs contain 32 and 64 pre-amplifiers each followed by pulse shaping circuits and level comparators for triggering and address encoding. Solutions with analog to digital conversion, contains a Wilkinson ADC in

every channel that generates a 10-bit digital word proportional to the amplitude of the input pulse. Upon interaction of radiation in the sensor the VATA delivers digital signals proportional to the energy of the photon as well as a digital address corresponding to the point of interaction and an output common trigger signal. The power dissipation is as low as 0.2 mW per channel during normal operation and an equivalent noise charge of 179 e- RMS at 0pF input capacitance [128]. Figure 22 illustrates the block diagram of one channel electronics of recent VATA65-HDR16 ASIC.

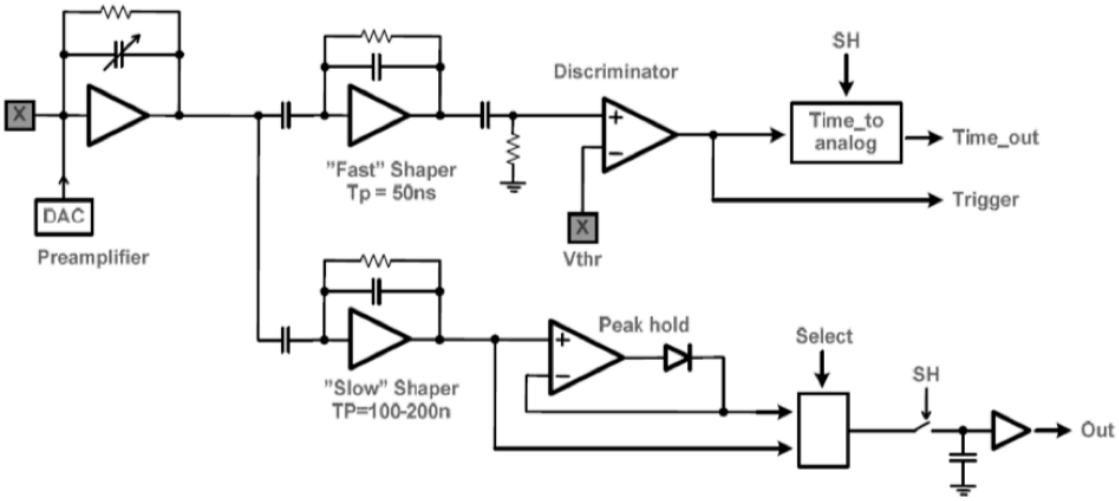

Figure 22. Architecture of one front-end channel of the VATA64-HDR16 ASIC [128].

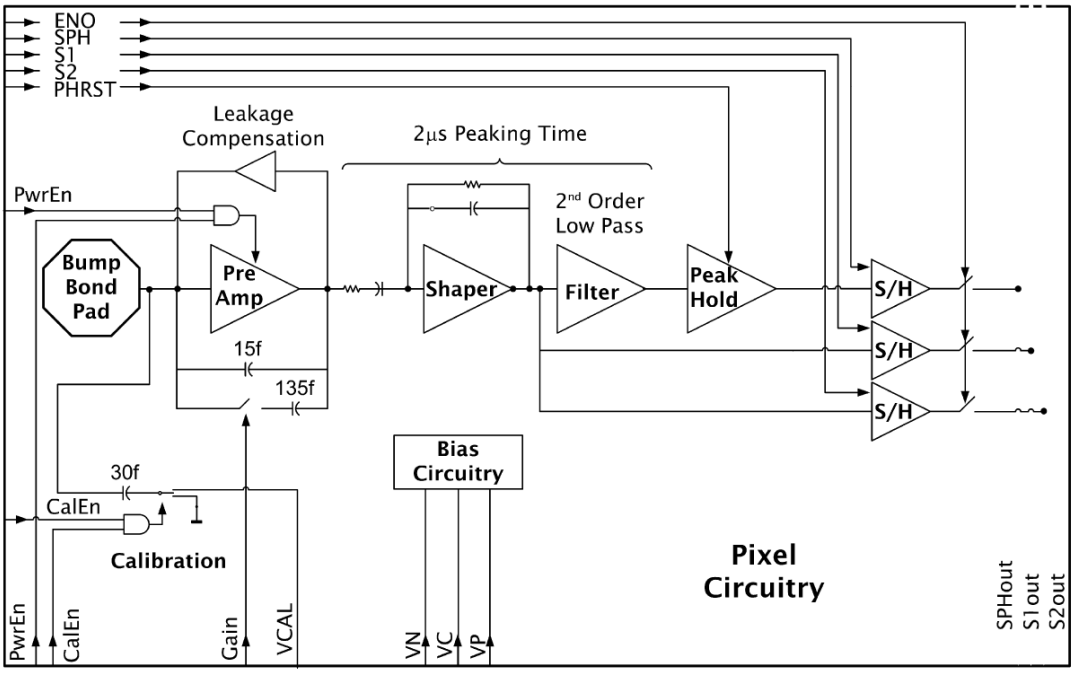

Figure 23. Block diagram of a pixel electronics of HEXITEC ASIC [129].

HEXITEC: The HEXITEC ASIC is designed by the Universities of Manchester, Durham, Surrey, Birkbeck college and STFC specifically to provide very good spectroscopy for every incident photon at the expense of speed of acquisition. The target applications are synchrotron diffraction, tomography experiments, and space science imaging which require very good energy resolution, and as a secondary requirement speed. The ASIC reads out all pixels of a programmed region of interest, what allows detector charge sharing and other correction algorithms to be investigated off-line. The pixel matrix consists of 20 x 20 pixel on a pitch of 250 μm first version, and a 80 x 80 pixel the latest. Each pixel contains a 52 μm bond pad which can be gold stud-bonded to a CZT detector. Charge is read out from each of the CZT detector pixels using a charge amplifier, which has a selectable range and a feedback circuit which compensates for detector leakage currents up to 50 pA. The output from each charge amplifier is filtered by a 2 μs peaking and a buffered peak hold circuit maintains the voltage at the peak of the shaped signal until it is read out [129].

TIMEPIX: TimePix family is developed together with MediPix family within the Medipix Collaborations by CERN and share the same detector layout geometry. TimePix ASICs have many similarities with MediPix ASICs counterparts in terms of pixel analog front-end and ASIC back-end. The major difference is that TimePix pixels can provide the time of arrival of the photons with an approximated precision of 1.6 ns, and they can be programmed to measure the time over threshold of the preamplifier pulse which is linearly dependent with the energy deposited by the photon thus obtaining the energy information for spectroscopy applications. TimePix ASIC was developed during the Medipix2 collaboration, while TimePix3 has been realized with Medipix3 Collaboration [122].

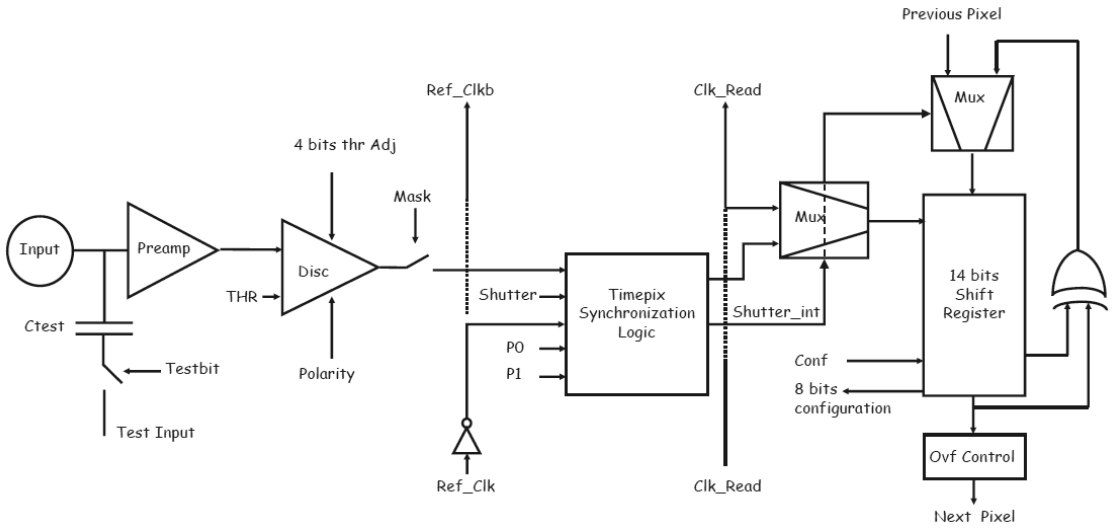

Figure 24. Timepix pixel's electronics block diagram [122].

FE-I4B/C: FE readout integrated circuits are developed within the FEI4 Collaboration with LBNL, NIKHEF, and SLAC centres among others as the series of integrated circuits for the Insertable B-Layer detector of ATLAS experiment at the LHC at CERN. Latest ASICs are FE-I4B and FE-I4C ASICs, which are upgrades of FE-I4A and former FE-I3 ASIC family. FE-I4 integrated circuit contains readout circuitry for 26880 hybrid pixels arranged in 80 columns on 250 μm pitch and 336 rows on 50 μm pitch. It is designed in a 130 nm feature size bulk

CMOS process. Figure 25 shows the block diagram of the analog pixel electronics. Each FE-I4 pixel contains an independent, free running amplification stage with adjustable shaping, followed by a discriminator with independently adjustable threshold. The chip keeps track of the firing time of each discriminator as well as the time over threshold (ToT) with 4-bit resolution, in counts of an externally supplied clock signal with a nominal period of 25 ns. The information from all discriminators firing is sent to the external controller upon request via LVDS serial communications at 160 Mbps rate [130].

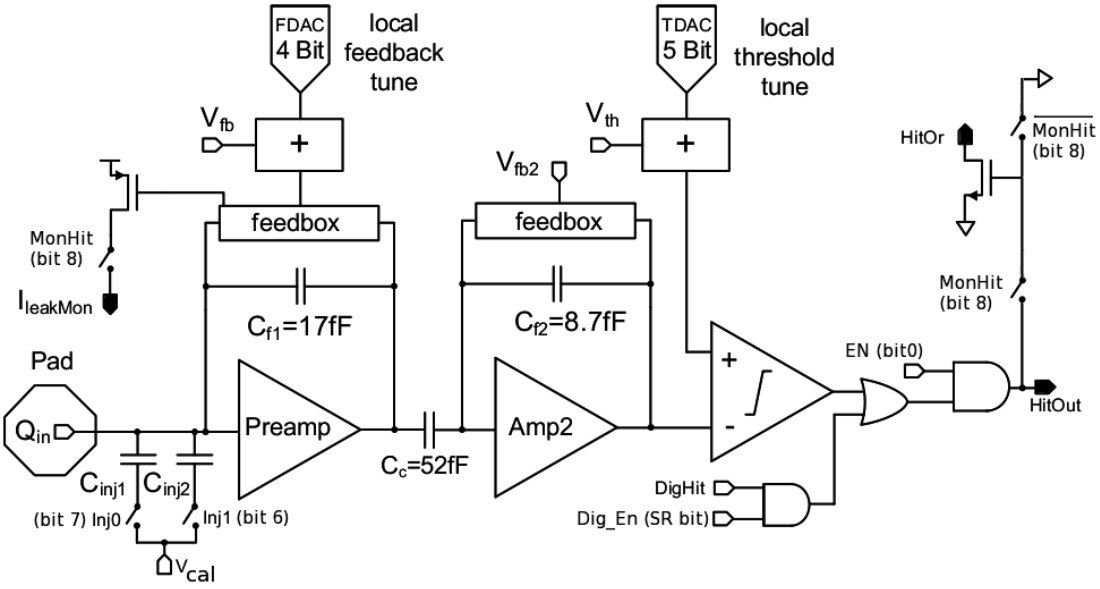

Figure 25. Analog pixel scheme diagram of FE-I4B ASIC [130].

IDeF-X HD: IDeF-X HD is a 32-channel analog front-end with self-triggering capability. The architecture of the analog channel includes a charge sensitive amplifier with a continuous reset system, a variable gain stage, a Pole-Zero cancellation stage, a variable shaping time second order low pass filter (RC^2 Filter), a baseline holder, a peak detector, and a discriminator. Individually in every channel, peak time can be tuned from 2.7 µs to 10.73 µs in 4-bit steps and energy thresholds can be set in each channel with in-channel 6-bit low power DAC. The channel power consumption is 800 µW and the dynamic range of the ASIC can be extended to nearly 1 MeV thanks to the in-channel variable gain amplifier. All digital circuits are implemented using a single event latchup (SEL) hardened library. IDeF-X HD ASIC was designed to build the Caliste detector module for high spectroscopy application [131,132].

5.3 Time of Flight Readout ASICs

In time-of-flight applications, the readout of the time stamp of photon interactions with excellent time resolution is necessary to match events and convert it into spatial precision. In the case of Time-of-Flight PET scanners, the energy deposited by the photons is also

needed with high resolution to discard photons with scattered flight direction prior to the detection. The most common energy measurement technique is time-over-threshold since usually they are designed to support high photon flux. Following three available time-of-flight readout ASIC families are detailed.

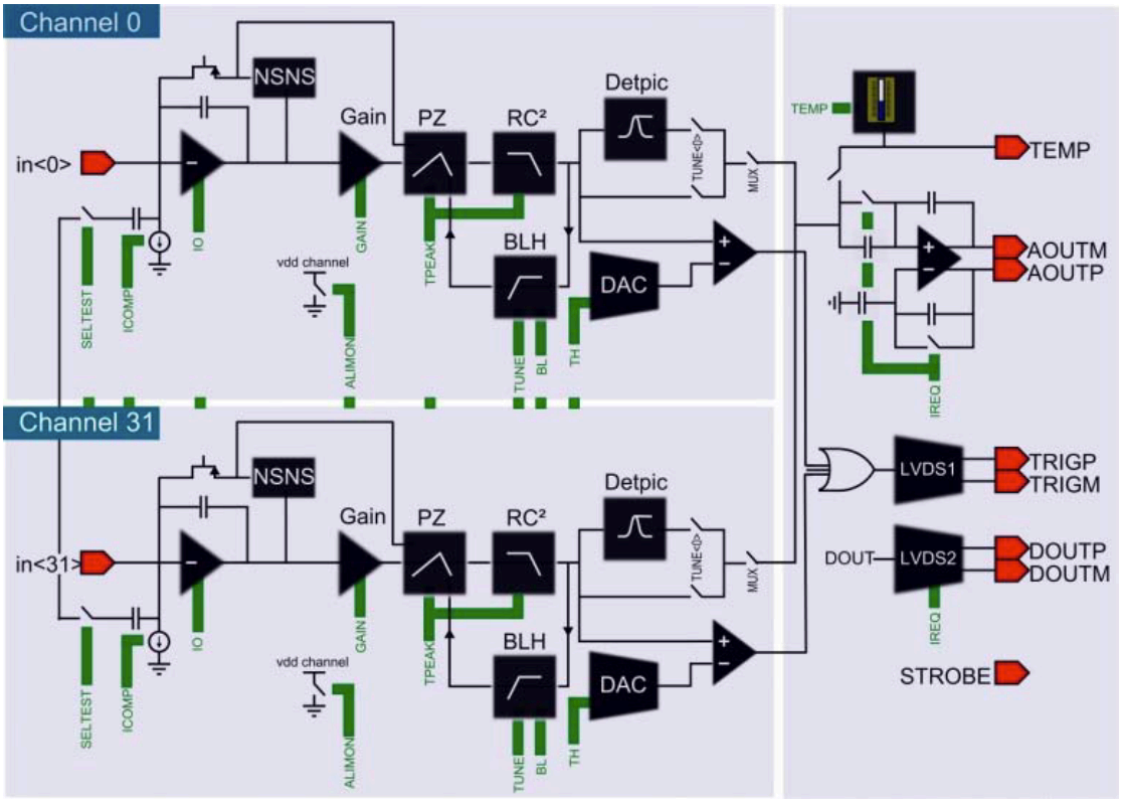

Figure 26. Block diagram of IDeF-X ASIC [131].

TRIROC: Triroc is the latest addition to SiPM readout ASICs family developed at Weeroc from the Omega microelectronics group of IN2P3/CNRS. This chip is developed under the framework TRIMAGE European project which is aimed for building a cost effective tri-modal PET-ToF/MR/EEG brain scan. To ensure the flexibility and compatibility with any SiPM in the market, the ASIC is designed to accept negative and positive polarity input signals. This 64-channel ASIC, is suitable for SiPM readout which requires high accuracy timing and charge measurements. Main features of Triroc includes high dynamic range ADC up to 2500 photoelectrons and TDC fine time binning of 40 ps. It is designed by using AMS 0.35 µm SiGe technology to achieve high speed front-end electronics with acceptable power consumption [133].

TOFPET2: TOFPET2 is a readout and digitization ASIC featuring low-noise and low-power for time-of flight (TOF) applications using SiPMs. The circuit is designed in UMC standard CMOS 110 nm technology, has 64 independent channels and is optimized for time-of-flight measurement in Positron Emission Tomography (TOF-PET). The input amplifier is a low impedance current conveyor based on a regulated common-gate topology. Each channel has quad-buffered analogue interpolation TDCs (time binning 30ps) and charge integration

ADCs with linear response at full scale (1500pC). The signal amplitude can also be derived from the measurement of time-over-threshold (ToT). The maximum event rate is 480kHz per channel, with up to 2MHz dark counts rejection [134].

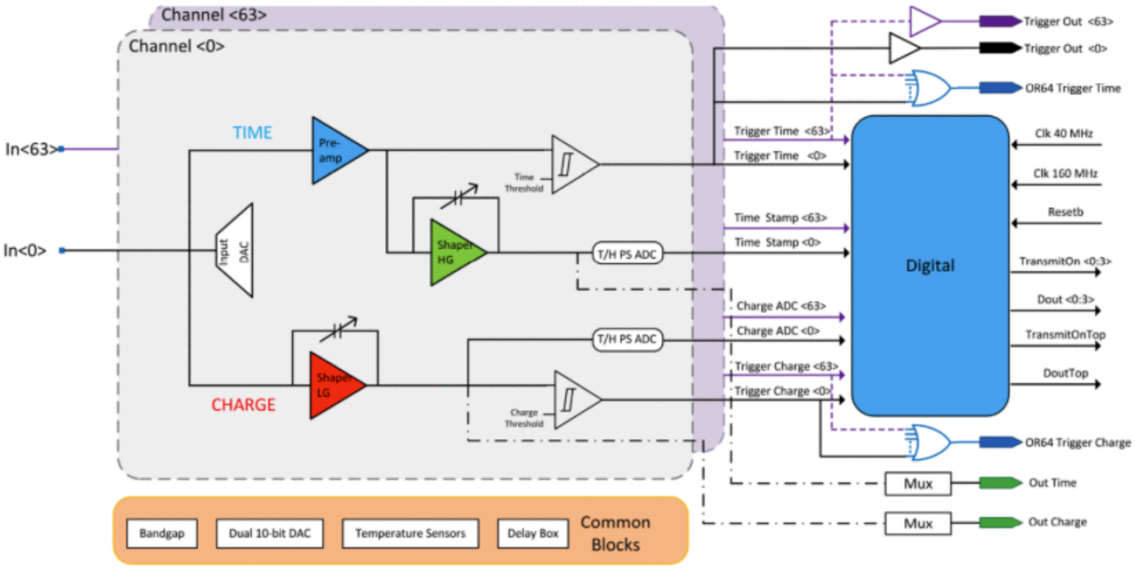

Figure 27. Block diagram of Triroc ASIC [133].

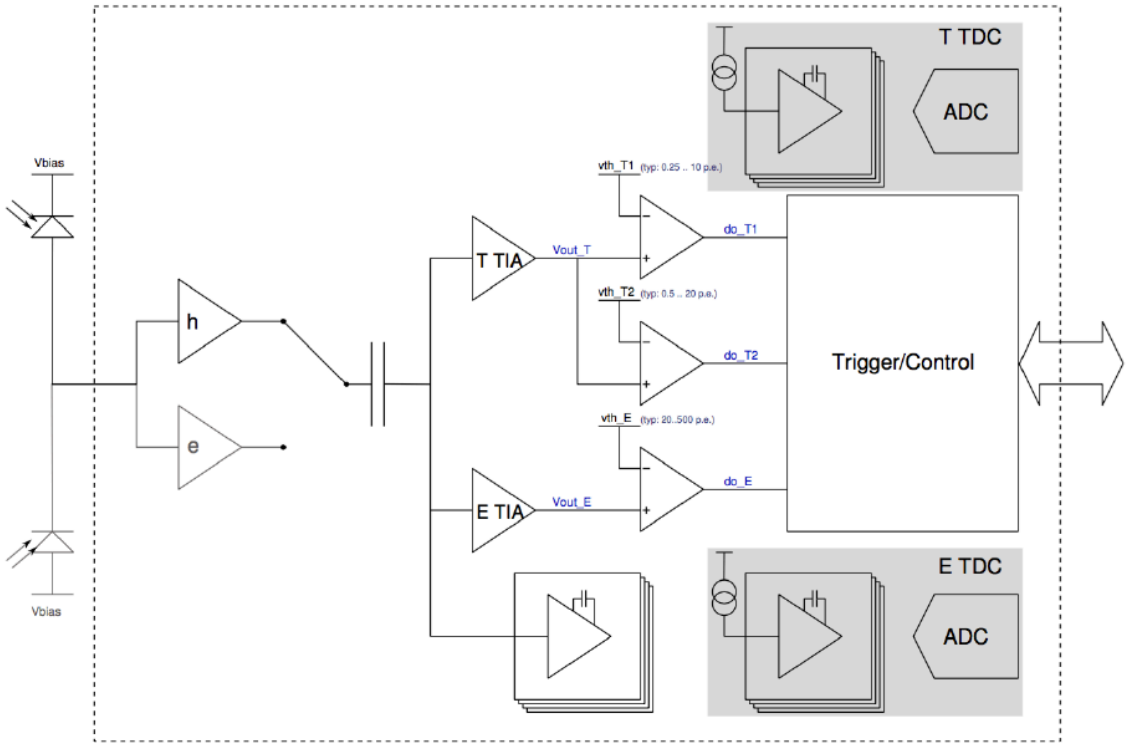

Figure 28. One channel pixel electronics block diagram of TOFPET2 ASIC [134].

PETIROC/CITIROC: Petiroc and Citiroc are the two latest ASIC from Weeroc dedicated to SiPM read-out. Petiroc is a 16-channel front-end ASIC designed to readout silicon photomultipliers (SiPMs) for particle time-of-flight measurement

applications. It combines a very fast and low-jitter trigger with an accurate charge measurement. Citiroc is a 32-channel front-end ASIC that allows triggering down to 1/3 pe and provides the charge measurement with a good noise rejection. Moreover, Citiroc outputs the 32-channel triggers with a high accuracy (100 ps). Each channel of both ASICs combines a trigger path with an accurate charge measurement path. An adjustment of the SiPM high voltage is possible using a channel-by-channel input DAC. That allows a fine SiPM gain and dark noise adjustment at the system level to correct for the non-uniformity of SiPMs. Timing measurement down to 16 ps RMS jitter for Petiroc and 100 ps RMS for Citiroc is possible along with 1% linearity energy measurement up to 2500 pe. The power consumption is around 3.5 mW/channel for Petiroc and 3 mW/channel for Citiroc, excluding ASICs outing buffer [135].

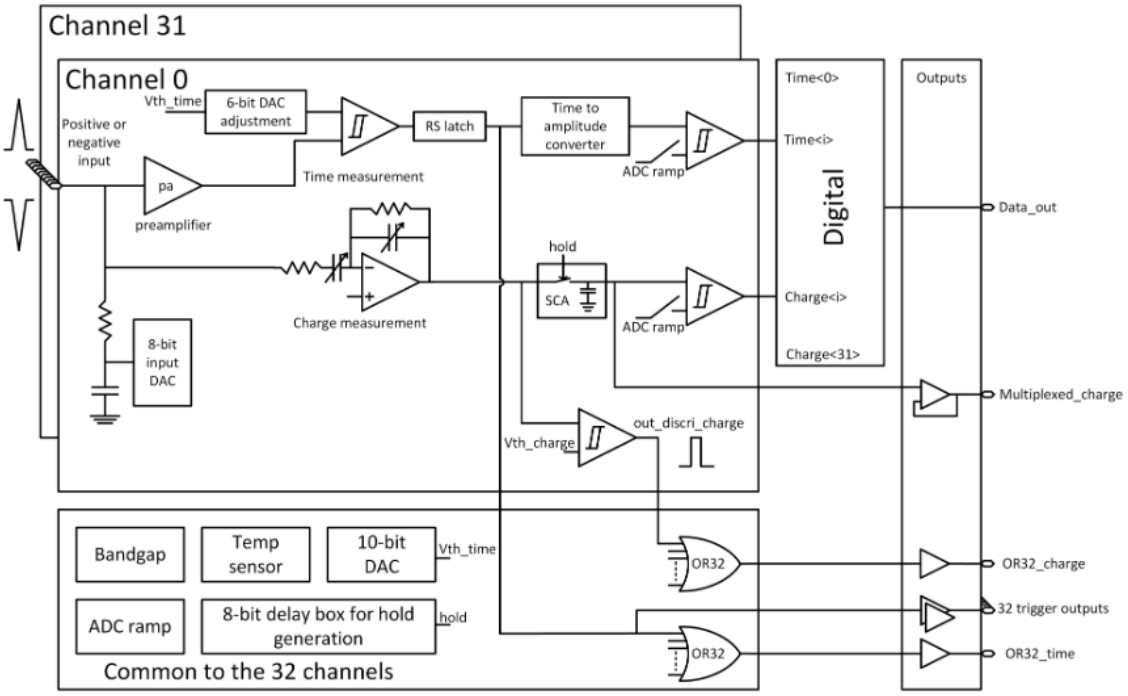

Figure 29. Block diagram of PETIROC-2A ASIC from Weeroc SAS [135].

Most of the ASICs presented above are used in commercial systems and cameras for applications from particle accelerators and radiation detection mapping in the International Space Station to X-Ray odontology scanners. Nevertheless, they are just a small sample of the wide variety of solutions available in the literature [136].

ASICs for PET applications must provide excellent energy resolution and precise time of arrival information simultaneously. Among the presented ASICs only those for Time of Flight applications provide time stamp and energy simultaneously. Nevertheless, they are designed to be connected by wire-bonding techniques to the SiPM arrays and they are not pixelated. Therefore, by the time that the design of the VIPPIX ASIC started, there was no

pixelated readout ASIC with excellent energy resolution (0.1 % RMS at 511 keV) and time stamp precision of few ns simultaneous measurement available.

The architecture of the new VIPPIX ASIC had to be designed to provide simultaneous measurement of the energy of the pixel where the photon interaction occurred, the position of the firing pixel, and the time of the arrival of the photon. The type of architecture and the specifications of the individual circuit blocks depend strongly on the requirements of the application, i.e., the flux of photon interaction per pixel, the detector's pixel size, thickness, bias voltage and expected leakage current, the minimum detectable energy, working temperature. Next section summarizes the specifications of the VIP PET scanner design and the derivations of the requirements of the readout electronics.

Chapter 6

Design of the VIPPIX ASIC

The specifications of the VIPPIX ASIC have been derived from the requirements of VIP PET scanner in terms of the operating conditions of the detector ring, and the geometrical and electrical specifications of the CdTe detectors. The derivation of the VIPPIX specs are divided into three categories: From geometrical specs of the CdTe Detectors, from electrical specs of the CdTe detectors, and from operating conditions of the VIP detector ring.

6.1 Specifications of VIPPIX ASIC from the operating conditions of the VIP detector ring

According to the expected simulated results of VIP scanner [148], the best counting signal to noise ratio of the VIP detector ring is obtained with 32 MBq distributed in a volume of approximately 6 litres for NEMA NU 2-2001 standard. The total sensitivity of the scanner is 14.37 cps/kBq which scaled to the optimum activity means a total number of hits of 460000 counts per second approximately in the full PET. Considering 6 million independent channels, we might expect one hit per pixel every 13 seconds, so approximately 8 hits per second in every detector. Clearly, with such a relaxed rate per pixel and per detector, the counting performance of the scanner is not limited by pile up but by the timing resolution of the time stamp, i.e. when three hits fall in the same time coincidence window and their energy does not sum up 511 keV, all three hits must be discarded, therefore the efficiency drops. When timing resolution improves, the width of the window is stretched so the number of discarded events decreases accordingly.

The desired working temperature range of the VIP CdTe detectors for high energy resolution and precise timing extends from -20 to 25 Celsius degree since much lower temperatures change electron and hole mobility in opposite directions (Figure 8) which smear energy and timing resolutions and higher temperatures prevent the CdTe detector to work with high electric field due to the extreme DC leakage current and the noise associated.

In hybrid detector technology where the solid-state detector is in direct contact with the pixelated readout ASIC, the temperature of the detector depends basically on the temperature of the room and the balance from the heat transfer from the ASIC and all cooling mechanisms (i.e., convection, conduction, radiation, etc.).

VIP detector modules are based on the stacking of multiple layers of hybrid detectors (VIPPIX ASIC + CdTe Detector) with no gap from module to module or between layers as shown in Figure 4. Therefore, the geometry of the VIP modules does not facilitate any conventional cooling mechanism and the heat dissipated by the ASIC is fully transferred to the detectors. The temperature of the system might increase dramatically in some regions inside the modules specially if the power consumption of the ASIC is not sufficiently low. Considering approximately 6.6 million equally distributed pixels in the detector ring, a power consumption of 1 mW per pixel will dissipate 6.6 kW in the complete scanner. Therefore, due to the expected very inefficient cooling of the VIP geometry, such pixel power consumption is not acceptable for this application. To keep the temperature of the detectors close to room temperature, the pixel's power consumption should be in the order of 100 μW.

6.2 Specifications of VIPPIX ASIC from the geometrical specifications of the CdTe detector

The CdTe detector used in the first prototype VIP scanner has a thickness of 2 mm, a size of 10.1 mm x 10.1 mm, and a pixelated anode side with 100 electrodes of 0.95 mm x 0.95 mm each. Note that the pixel size to detector thickness ratio is approximately ½ which contributes to the pixel effect as plotted in Figure 11.

CdTe detectors of 2 or more-millimetre thickness fill large detection volumes with high-Z material with reasonable small number of detectors. Therefore, for a fixed detection volume, one should work with thick semiconductor detectors to minimize the number of readout ASICs, i.e., lower power consumption, if energy and timing resolutions prevail. Unfortunately, the thicker the planar detector, the poorer energy and timing resolutions due to several factors: first, to generate the same electric field than with thinner detectors, scaled higher voltages must be provided to the electrodes of the detector which in occasions is not allowed by the complexity of the system; second, charge collection time scales with thickness, provided the same electric field is available inside the detector. Additionally, due to longer collection times, trapping and recombination reduce the collected charge and the percentage of charge losses depends on the depth-of-interaction; third, thicker detectors show larger pixel effect which decreases the time resolution of the detector since the velocity of the carriers depends dramatically on the depth-of-interaction as derived from Figure 11; and fourth, charge sharing among neighbour pixels increases with the detector thickness for a given pixel size and an electric field from cathode to anode.

Unlike with Silicon wafers, the fabrication of CdTe wafers is still very expensive since the process to achieve "defect-free" CdTe raw material is complex and the yield still low. Additionally, metal and passivation deposition and post-processing became challenging since the conductivity of the raw CdTe results altered and resistivity in the order of 10^9 Ohm·cm are needed for radiation detectors [137]. CdTe manufacturers, as Acrorad in Japan, offer 2-mm thickness detectors still with reasonable price and high purity, while they recommend 1-mm thickness if possible.

In the case of VIP PET design, having 1-mm thickness detectors would double the number of readout channels which is not desirable since it doubles the amount of dead material in the path of the photons (i.e., metal bumps, printed circuit board layers, glue layers) and sets the power consumption limit of every pixel to 50 μW or less.

The pixel size and the detector thickness define the capacitance of every pixel. This parameter is crucial for the design of the front-end electronics since KTC noise scales linearly. Additionally, the pixel capacitance lowers the bandwidth of the charge sensitive amplifier if not designed properly since it is connected directly into the driving terminals of the first amplification stage of an operational amplifier. Therefore, having a good model of the detector capacitance is mandatory for the optimization of the first amplification stage and the achievement of what is named “noise matching” [138].

6.3 Specifications of VIPPIX ASIC from the geometrical specifications of the CdTe detector

The spectroscopic performance and the timing performance of the hybrid detector, i.e. detector with readout ASIC, depend strongly on the leakage current of the semiconductor detector, the charge collection efficiency, the charge sharing among neighbour pixels, and the charge collection time. Additionally, it is well known that the polarization of the Schottky detectors set a limitation in the scan window since the DC bias applied to the detector should be reset to restore the zero-charge condition of the Schottky interface [98,99].

6.3.1 Architecture of the pixel front-end.

The architecture of the front-end electronics is determined by the application which in this case is characterized by the need to obtain excellent energy and time resolution. When charge collection time is well known and it doesn’t depend on the depth-of-interaction, the scheme based on “fast” shaping for the generation of the time stamp of the event and “slow” shaping for the acquisition of the energy deposition of Figure 22 shows excellent precision since preamplifier noise is filtered specifically in two different frequency bands. Planar silicon detectors show excellent performance with this approach since hole collection time doesn’t differ much from electron collection time at room temperature. [139].

Nevertheless, electron collection time in CdTe is one order of magnitude shorter than hole collection time. Therefore, two photon interactions with the same energy deposition but at two different depths inside the detector will show a different preamplifier output shape and the corresponding filtered shaper output and they will generate different trigger timing as shown in Figure 30. The difference in trigger timing is plot for electron and hole collection for different charge injection percentage (referred to full range injection) and different shaper peak time for an electron total collection time of 20 ns and a hole collection time of 220 ns. As expected specially for low energy deposition, different firing of the output trigger is obtained due to time walk for a given energy threshold in the discriminator.

Ideally, note that for the same energy deposition and triggering at the output pulse of the preamplifier a “time walk free” trigger can be obtained, provided the percentage of electron charge injection is higher than the energy threshold.

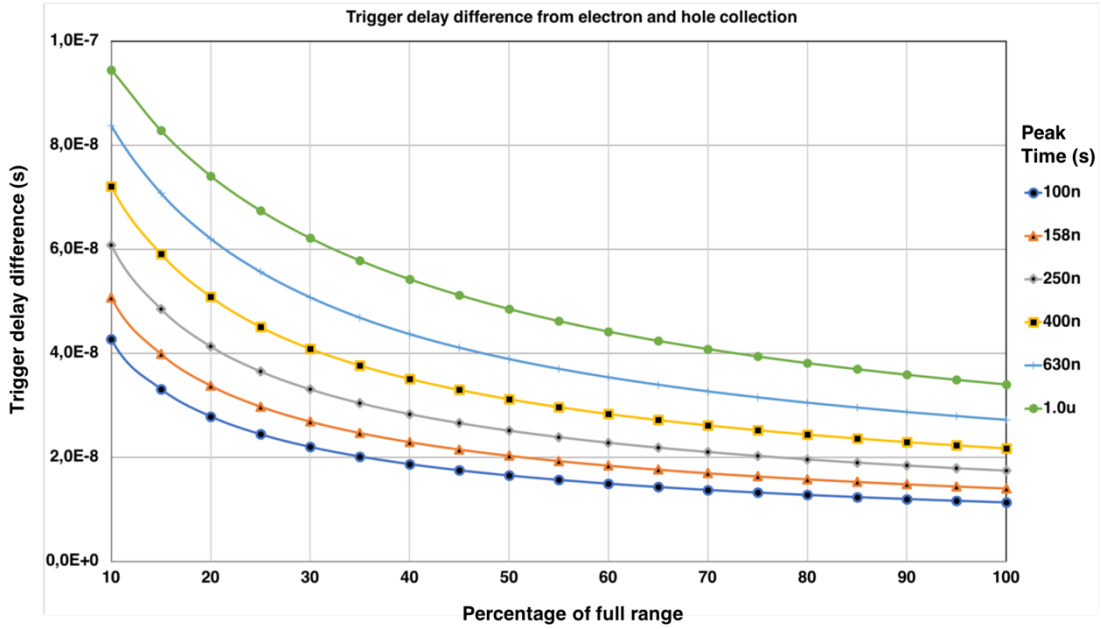

Figure 30. Difference in trigger time of electron and hole collection versus the percentage of full charge injection and different shaper's peak time based on simulations using ideal amplifiers.

6.3.2 Detector leakage compensation

Pixel detector's dark current must be provided by the first amplification stage of the readout electronics. Looking at Figure 16, one can realize that in absence of any leakage compensation feedback amplifier, the leakage current of the detector creates an offset at the output of the charge sensitive amplifier with a value equal to $R_{feedback} \cdot I_{leakage}$. This offset has two components: a DC shift and an induced AC noise. If high stability of the output voltage's DC component is required, as in the case of connecting the preamplifier to a pulse discriminator, a dynamic leakage compensation feedback circuit should be used as feedback resistor. The noise due to the leakage current can be filtered out by using a pulse shaper which acts as a band-pass filter that limits the bandwidth of the noise.

6.3.3 Preamplifier Baseline Restore Time

Ideally, when a current pulse is integrated in the feedback capacitor, charge must remain untouched until a certain reset procedure is applied to restore the zero-charge bias conditions. In this way, the output pulse height reflects exactly the injected charge. Unfortunately, any feedback circuit from the output of the preamplifier to the detector node will introduce a limited impedance so the integrating capacitor will discharge with time. Although best collection time of CdTe detectors can be in the order of few tens of ns, some charge is lost during the charge injection due to the limited feedback impedance and the associated baseline restore time. For constant current discharging feedback resistors, the percentage of charge lost during the rising edge depends linearly on the ratio of charge collection time and baseline restore time. Therefore, for a charge collection resolution of 0.1

%, the baseline restore time must be at least three orders of magnitude larger than the maximum charge collection time.

In the case of preamplifiers with dynamic leakage compensation circuits, the slope of the baseline restore is determined by the range of leakage current compensation [152]. Therefore, a first trade-off among the maximum leakage compensation, the stability of the preamplifier's DC output voltage, and the charge collection resolution must be decided.

6.3.4 Peak time of shaper

The peak time and the integrator-order of the pulse shaper define the noise rejection from the high frequency noise associated to the fast response of the preamplifier and the thermal noise of the detector capacitor, and from the flicker noise of the electronics associated to the DC and low frequency response of the preamplifier and leakage current. Pulse shaping works ideally when the input pulse follows a Heaviside function with zero rise time and infinite baseline restore time. Nevertheless, when the input pulse shows a triangular function, the time and the amplitude of the peak and the shape of the output pulse can differ dramatically from ideal. In first order of approximation, when the peak time of the shaper is one order of magnitude larger than the maximum collection time, and one order of magnitude smaller than the baseline restore time we can neglect the effects of limited timing. This condition sets the limits of the peak time of the shaper since the baseline restore time depends on the leakage current of the detector and the total charge collection time.

Despite absolute charge collection efficiency is never 100%, detectors and spectrometers demonstrate energy resolution better than trapping degradation since all measurements are normalized to the maximum charge collected. In the case of semiconductor detectors, this situation happens when a photon undergoes a pure photoelectric interaction close to cathode of the detector. Note that the uncertainty of the depth-of-interaction introduces three smearing mechanisms in the energy resolution: first, different charge collection efficiency at the level of the detector; second, degradation of the pulse height in the preamplifier; and third, different shape and peak amplitude in the shaper.

Additionally, events with the same energy but with different total collection time show different shaped pulse peak time. Therefore, a peak and detect circuit is necessary for high resolution readouts to latch on the peak value regardless the peak time.

6.4 Summary of article "Toward VIP-PIX: A Low Noise Readout ASIC for Pixelated CdTe Gamma-Ray Detectors for Use in the Next Generation of PET Scanners"

In this article, the architectures of the VIPPIX readout ASIC and the VIPPIX pixel electronics are introduced. The design of the different blocks of the pixel front-end electronics is detailed based on the requirements of the VIP PET scanner application. Additionally, the measurement results of each block separately and the analog front-end are presented. The successful results in terms of noise, linearity, time precision, and power consumption set the foundations of the pixel electronics of the 10 x 10 pixel-array readout ASIC.

6.4.1 Introduction to VIPPIX

Based on the extensively published excellent energy resolution of CdTe detectors (1-2% FWHM for 511 keV) and the low noise associated to small capacitance of pixelated thick detectors, excellent scatter rejection is expected in the PET scanner based on highly pixelated volume of CdTe detectors provided a low noise readout electronics.

Since the detector's dimensions and number of pixels were fixed (100 voxels of 1x1x2 mm^3), the area of the pixel electronics and the ASIC were 1x1 mm^2 and 10 x 12 mm^2 respectively, 100 mm^2 for the pixel matrix plus extra 20 mm^2 approximately for the ASIC back-end analog and digital electronics and Input/Output pads. Figure 31 illustrates the block diagram of the VIPPIX ASIC. The ASIC is composed of two well-differentiated parts, the pixel matrix where 100 independent pixel electronics are connected to the ASIC back-end electronics with three well-separated buses to avoid cross coupling among pixels: **Analog** supplies and references, **mixed-signal** supplies, and **digital** supplies and data lines. The ASIC back-end electronics includes a bandgap current reference, a temperature sensor, five buffered voltage DACs with 6-bit resolution, a TDC that provides the time stamp of the first fired trigger with sub-ns resolution, a chip ID, and a digital controlled that communicates with the external micro-controller or FPGA and manages the states machines of every pixel according to the operation mode. Voltage and current references are generated on chip with just one external resistor. Therefore, only supplies and digital control and data lines are connected to the mounting PCBs.

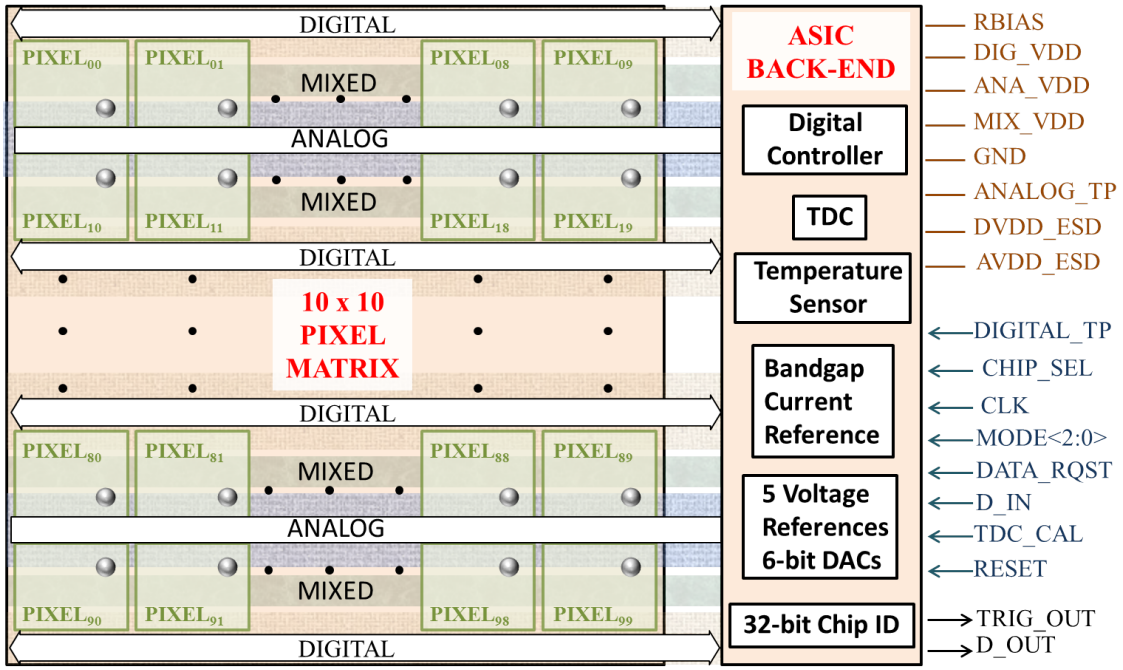

Figure 31. Block diagram of the VIPPIX ASIC.

The pixel electronics is illustrated in Figure 32. Pixels' front-end is composed of a preamplifier with programmable gain, baseline restore time, and leakage compensation

range, a charge injection test pulse circuit, a pulse shaper with tuneable peak time from 2 to 20 us, a peak and detect circuit, a 10-Bit successive approximation register ADC, and a discriminator with offset compensation with 7-Bit DAC resolution. Every circuit is provided with a reset input to provide a fast baseline restoring, specially the peak and detect circuit which can show a fall time of more than a second for full energy events. The Back-End electronics is purely digital and is composed of a 41-bit shift register with its corresponding 41-bit configuration shadow register to set all the tuning values of every analog block. Additionally, a simple state machine that controls the pulses of the ADC and the analog reset signals based on a dedicated clock input line completes the digital circuitry. The output trigger of every pixel is connected to the ASIC TDC and the digital controller such that the TDC will provide the timing and the trigger line will specify the fired pixel. The layout of the pixel was realized to match the analog, mixed-signal and digital bus distribution illustrated in Figure 31.

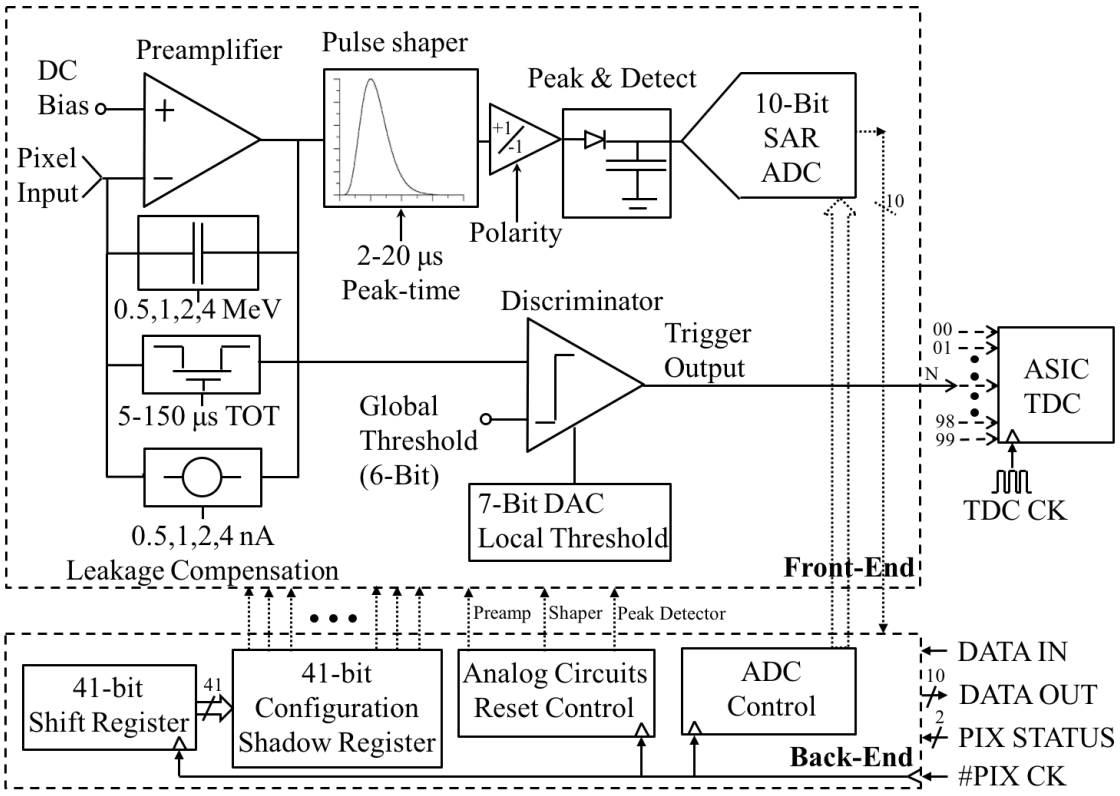

Figure 32. VIPPIX pixel electronics block diagram.

6.4.2 Measurement results

In this article, the results of the integrated pixel analog front-end, the pixel ADC, and analog front-end connected in a package to the ADC are presented. Multi-project wafer submissions with TSMC 250 nm CMOS process were used for VIPPIX test ASICs. Once diced, each individual circuit, i.e., pixel front-end and ADC, was packaged in a 48-pin CLCC chip carrier and tested in a dedicated testing PCB as shown in Figure 33. The pixel front-end was characterized with external test pulse signal with saw shape from a waveform generator with

0.1 % linearity for all dynamic range. The output signals of the preamplifier, the shaper, and the peak and detect circuit were buffered out and connected to the oscilloscope in high-impedance mode. Their behaviour was verified in terms of timing, peak amplitude, and peak to peak noise. Additionally, the time response of the discriminator with the amplitude of the test pulse was characterized with a 25 ps resolution counter and taking as reference the test pulse synchronization pulse.

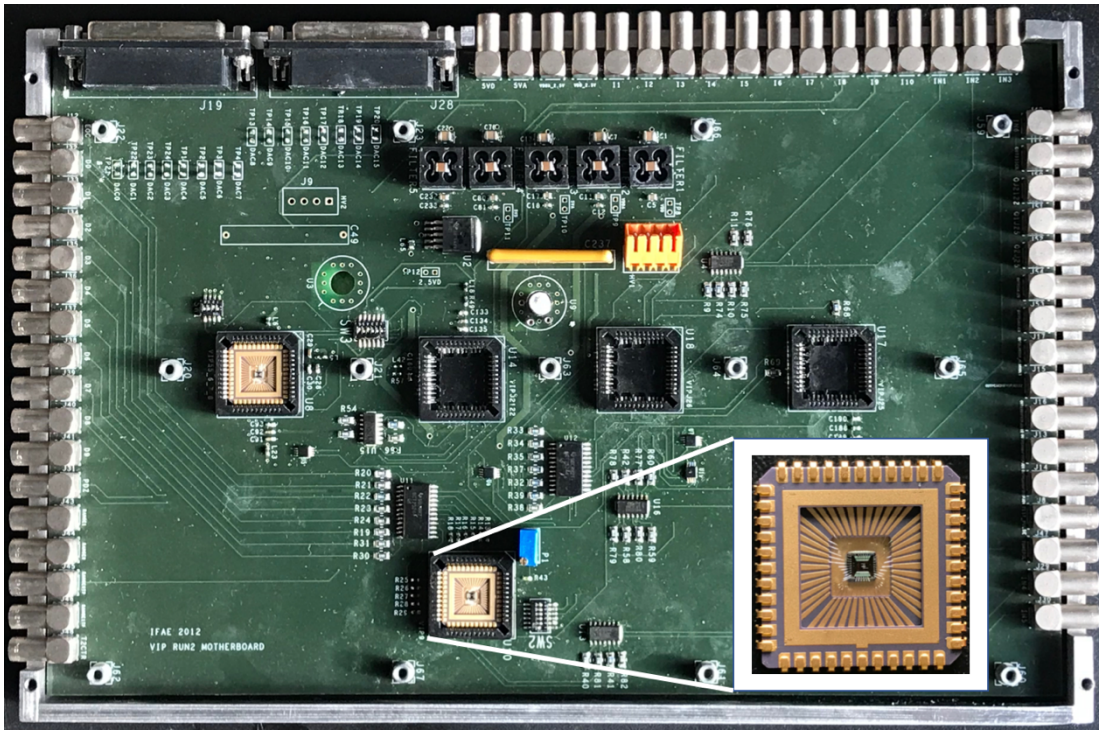

Figure 33. Testing PCB of VIPPIX individual parts and detailed photography of a packaged ADC in a 48-Pin CLCC chip carrier.

Table VII. Measurement results of individual parts of VIPPIX pixel front-end.

Input charge dynamic range	+/- 17 fC to +/- 70 fC
Gain for both polarities	10, 16, 20, and 40 mV/fC
Shaper peak time	4 to 16 μs
Peak-and-detect circuit discharge rate	160 μV/ms
Detector leakage compensation	Up to 10 nA per pixel
Minimum Threshold	6 keV
ENC @ 40 mV/fC (Pos/Neg Polarity)	98 e^- RMS / 107 e^- RMS
Discriminator jitter	< 10 ns for E > 20 keV
Supply Voltage	2.5 V
Preamplifier / Shaper	75 μW / 20 μW
Peak and hold / discriminator	20 μW / 35 μW
ADC / Total Power Consumption	50 μW / 200 μW
ADC conversion clock frequency	1 MHz
Analog front-end area	300 μm x 400 μm
ADC area	400 μm x 400 μm

To test the pixel ADC, an external FPGA was used to send the control signals to the ADC such the conversion clock and the start of conversion pulse, and to read out the data from the 10-bit bus when the End-of-Conversion pulse was triggered after the conversion. The linearity of the ADC was measured with an input DC signal from a 16-bit external DAC controlled with LABVIEW software from National Instruments.

Table VII summarizes the measurement results of the analog front-end, the analog to digital converter, and their combined response.

6.4.3 Conclusions

The fundamental circuits of a pixel readout electronics of a new readout ASIC for positron emission tomography scanners based on pixelated Cadmium Telluride detectors are presented. The architecture of the ASIC is based on a 10 x 10 pixel matrix of 1 mm^2 pixel size and back-end electronics including voltage and current references, digital to analog converters, a time to digital converter, a temperature sensor, and a digital controller.

The pixel analog front-end electronics comprises a preamplifier with leakage compensation, switchable feedback capacitor, and tuneable feedback resistor, a pulse shaper with adjustable peak time, a peak and detect circuit, a 10-bit ADC and a discriminator with offset compensation local DAC. To minimize the time dependency of the trigger delay with the depth of interaction, the discriminator is directly connected to the output pulse of the preamplifier. All circuits can be biased at different operating voltages to work with hole and electron charge collection indistinctly. Measurement results show an input referred noise of 98 e- RMS and 107 e- RMS for positive and negative polarity, a corresponding minimum trigger of 6 keV, and a trigger jitter below 10 ns for energy higher than 20 keV. The pixel electronics including the ADC consumes 200 μW from a single 2.5 V supply. Therefore, the pixel analog front-end achieved the requirements for the VIPPIX ASIC and it was going to be integrated with all digital pixel control circuit.

6.5 Summary of article “A 2D 4x4 Channel Readout ASIC for Pixelated CdTe Detectors for Medical Imaging Applications”

In this article the design and the measurement results of the successful integration of 16 pixels electronics in a 4x4 array with the additional circuits of the VIPPIX ASIC Back-End electronics are presented. Additionally, the first spectroscopy of ^{57}Co obtained with a bump-bonded 2-mm thickness CdTe pixelated detector with matching pixel dimensions is shown.

Based on the VIP PET scanner design, CdTe detectors are packaged and oriented with the electric field perpendicular to the direction of the photons. In this way, the probability of interaction is independent of the depth of interaction, or in other words, photon interactions have equal probability at different depth of the detector. Note that due to the limited mobility of holes and the pixel effect special design and calibration might be used in VIPPIX to avoid the degradation of the energy and timing resolution for all photon energies and directions.

VIP PET design requires excellent energy resolution to discard photons that underwent a Compton scattering prior to the detection and to obtain clean and precise images, i.e., to reduce dramatically the scatter fraction of the accepted events. The total

energy resolution of a hybrid detector has two main contributors: the intrinsic resolution of the collected charge in the detector, and the equivalent noise charge introduced by the front-end readout electronics which is defined commonly at the first stage. Since noise and resolution add in quadrature when they are uncorrelated, an electronic noise of one order of magnitude will be not relevant in the calculation of the detector resolution. Therefore, ideally an electronic noise equivalent to 0.1% FWHM resolution at 511 keV would represent a negligible part of a final 1% FWHM energy resolution of VIP PET. Such an electronic noise represents 48 e^- RMS assuming CdTe ionization energy. Such an ultra-low noise can be achieved by high consumption readouts with excellent cooling [140]. Unfortunately, VIPPIX pixel's power consumption is limited to 200 μW so the readout noise will be larger. A reasonable noise of 200 e^- RMS would represent just a 20 % of a total noise of 1% FWHM.

The paper is divided into two parts: a first part with the design and characterization of the pixel electronics and the pixel matrix, and a second one where the fundamental circuits of the VIPPIX ASIC are introduced and characterised.

6.5.1 VIPPIX ASIC and Pixel architecture

The architecture of the pixel was introduced in Figure 32. In VIPPIX pixel front-end, the output of the preamplifier is used as the input pulse of the discriminator. Such an unfiltered fast output of the preamplifier reduces the jitter of the trigger at the expenses of an increase in the minimum threshold due to a higher noise. Note that since we use a slow shaper for the energy measurement, an extra filtering and noise reduction is expected for the energy resolution. Therefore, in VIPPIX case we must refer to two different equivalent noise charge figures of merit: the ENC of the preamplifier which will be related to the jitter of the trigger, and the ENC of the energy path which will define the pixel readout energy resolution.

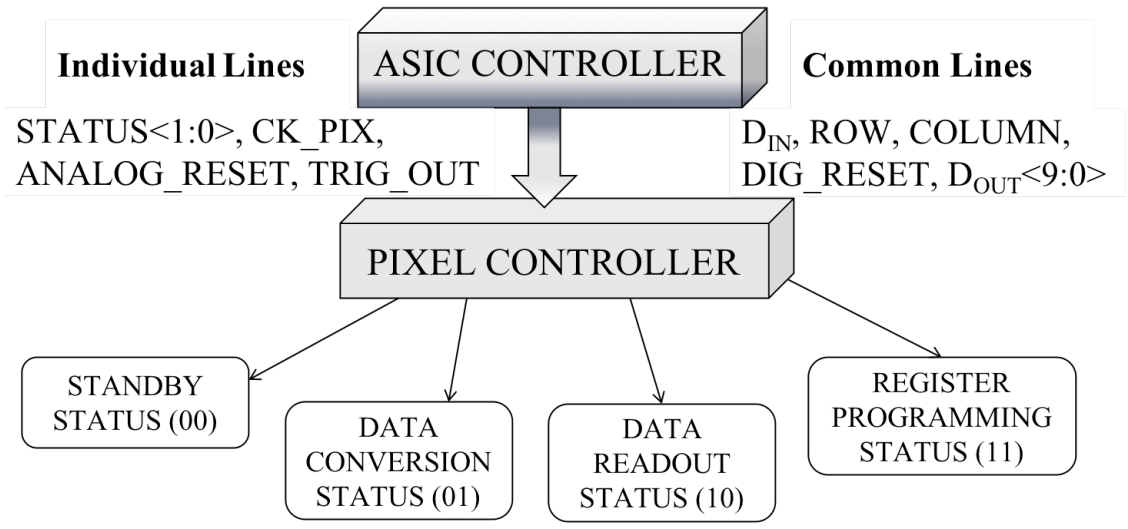

Figure 34. Operation modes and Input/Outputs of VIPPIX pixels.

The operation modes of the pixel are illustrated in Figure 34. The status of the pixel and the operation of the digital circuits is controlled by the ASIC digital controller with the following signals: a 2-bit status signal, a dedicated individual clock line, a pulse reset line, a row line, a column line, and a global digital reset signal. The pixel's standby mode is set by status '00'. Here the analog circuits are working in nominal conditions until a pulse is detected by the discriminator firing the trigger. At that moment, the ASIC controller changes the status of the pixel to conversion state (status = '01') and the ADC converts analog signal of the peak and detect circuit to digital peak value. By the time that the data is ready for readout, the status changes to '10', readout and analog reset mode. The configuration of the pixel is performed when the pixel is in '11' status and row and column are active. In that moment, the input data is synchronised with the pixel's clock line and data is dumped into the 41-bit shift register of the pixel. Once all pixels' shift register are programmed, the ASIC controller sends a Shadow Register Clock pulse to dump all data in the 41-bit shift registers into their corresponding Shadow registers.

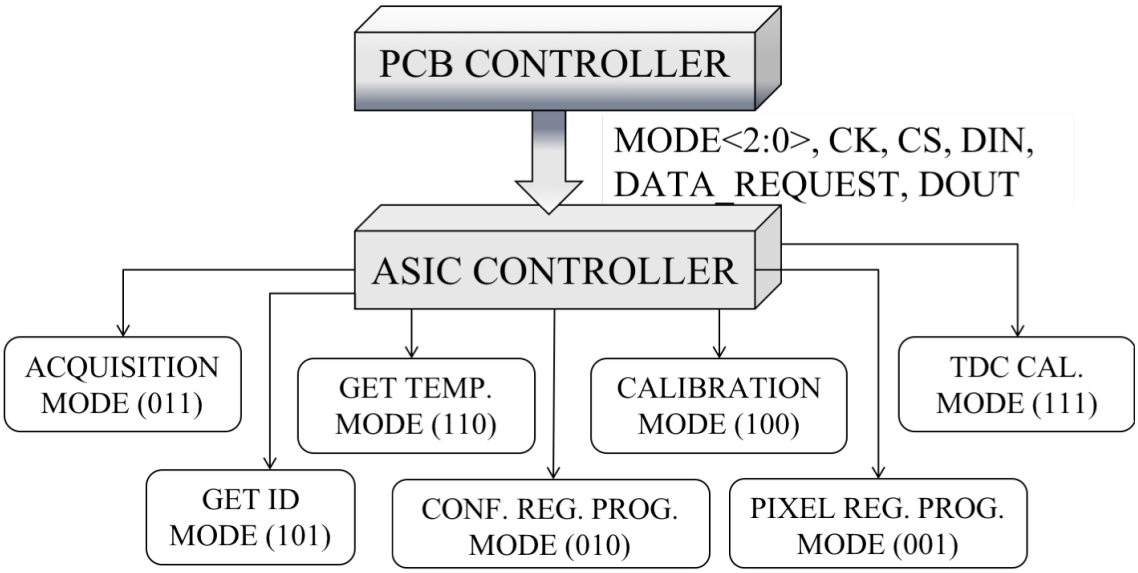

Figure 35. Operation modes and digital Input/Outputs of VIPPIX ASIC.

The architecture of the VIPPIX ASIC was introduced in the third article of section VI.4 and it is illustrated in Figure 31. It is worth to mention here that the final number of digital to analog converters in the Back-End Electronics was five instead of three since two extra voltage references were needed to separate top and bottom references of the ADCs from the minimum and maximum voltages of the analog circuits to ensure a non-zero DC offset of the digital values.

The VIPPIX ASIC is controlled by an external FPGA or a micro-controller which sets its operation mode and synchronises the data transmission and the configuration of the ASIC. Figure 35 illustrates the operation modes of the VIPPIX ASIC and the input/output signals.

6.5.2 Pixel electronics measurement results

A 4x4 pixel matrix with full back-end electronics was fabricated with TSMC 250 nm CMOS process. Therefore, the full integration of the pixel electronics and the autonomous control of the ASIC by the digital controller was realized and characterized. A total of five ASICs were tested completing the characterization of 80 independent pixels, five TDCs, five temperature sensors, and twenty-five 6-bit voltage DACs. The average power consumption of the pixels was 190 μW as shown in the individual characterization in the third article.

The pixel characterization is realized with three main tests: first, measurement of the noise levels of the preamplifier and the corresponding minimum threshold; second, the linearity and the energy resolution of the complete charge integration path; and third, the measurement of the trigger delay and jitter versus the amplitude of the input signal.

The noise of the channels has been characterized with an S-curve analysis realized with noise scans. White noise was assumed and the peak to peak noise measured to get the RMS noise level of every pixel. Minimum threshold is calculated as five times the RMS noise. An average minimum threshold of 5.3 keV is measured among 80 pixels. Considering Cadmium Telluride detectors this noise corresponds to 250 e- RMS as input referred noise charge.

The gain and linearity were evaluated with an external linear waveform generator and the internal test pulse capacitor to mimic the detector current pulses with different charge injection. The ASIC was set in acquisition mode and only self-triggered channels were digitized as working in nominal acquisition of PET events with a CdTe detector. Timing and energy was recorded and plotted. The linearity and the dispersion of the energy peak of 80 pixel's front-end electronics for positive polarity and negative polarity is reported. For negative polarity, a limited non-linearity along the full range up to few keV is observed. Offline amplitude compensation must be applied to achieve the energy resolution goal of 1 keV at FWHM. The peak dispersion shows an equivalent noise of 150 e^- RMS at zero charge injection and 220 e^- RMS at full charge injection. Such an increase in noise from small signal is due to the intrinsic non-linear performance of the tuning resistors of the pulse shaper and the peak and detect circuit.

The delay of the output trigger from the synchronization signal of the test pulse generator and the corresponding dispersion at FWHM, i.e., the jitter, are reported as well. Timing resolution gets worst in negative polarity due non-symmetric performance of the preamplifier and discriminator at different biasing conditions. The jitter is in any case below 10 ns for energies above 30 keV for both detector and electronic polarities which falls within the coincidence window required for PET events analysis.

6.5.3 Back-end circuits measurements

The design and the measurement results of the integrated time to digital converter and the temperature sensor are presented.

The architecture of the TDC is based on a first generation TDCs scheme composed of a pulse integrator and an analog to digital converter [141]. The time integrator is performed with a current pulse injected into an integrating capacitance. The peak of the voltage created

across the capacitor is then digitized. The dynamic range of the TDC is defined by the maximum width of the current pulse which is controlled by a defined clock period. In the case of VIPPIX, a 100 ns clock period and a 10-bit ADC are used to obtain a precision of 100 ps approximately.

The response of TDC was characterized with the same external counter with 25 ps resolution used for the jitter measurements. The synchronization of the ASIC input clock and the test pulse injection was necessary. The different TDC values where created by adjusting the synchronization delay. The measured sensitivity was 95.5 ps per ADC counts approximately. At full width half maximum, the TDC showed a resolution of 600 ps for close to 100 ns integration time. These results fulfil the requirements for PET scanners with highly pixelated detectors.

The temperature sensor is based on a constant-current forward-biased pn diode and a 10-bit SAR ADC. The voltage references of the ADC are optimized to increase the gain of the sensor. Measurements results show a gain of 0.4 degree per ADC count and a peak to peak dispersion smaller than one ADC count.

6.5.4 First spectroscopy results and conclusions

A hybrid detector composed of the 4x4 pixel matrix ASIC and a 2-mm thickness pixelated Schottky CdTe detector was packaged on a testing PCB as shown in Figure 36. The testing setup was introduced in a N^2 bath inside an industrial fridge at -10 Celsius degree and a ^{57}Co radioactive source was characterized resulting in a FWHM resolution of 3.6 % for the 122 keV peak.

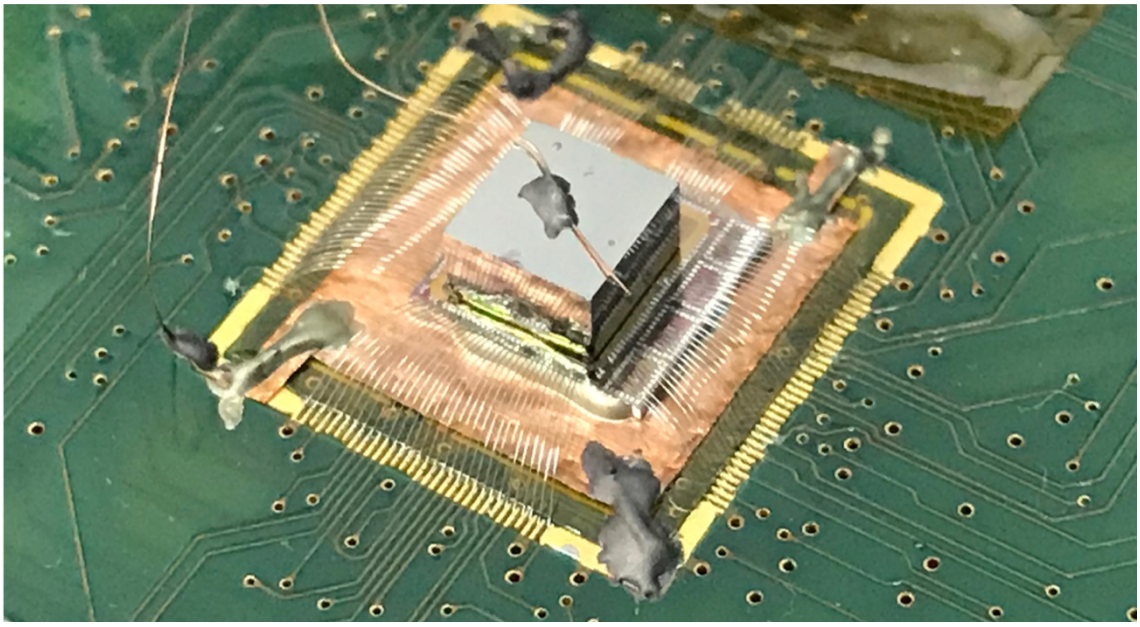

Figure 36. Photography of a hybrid pixelated CdTe detector on a VIPPIX 4x4 pixel matrix readout ASIC.

The performance of the VIPPIX pixel electronics, and the extra Back-End circuitry match the requirements for VIP PET scanner. Therefore, the full 10 x 10 pixel matrix readout ASIC could be based on the presented ASIC with no degradation of the signal quality since pixels are indeed independent readout circuits and the loading in the voltage and current references have been demonstrated in this work. Table VIII summarizes the performance of the 4x4 pixel matrix mini VIPPIX ASIC.

Table VIII. Specifications of the 4x4 pixel readout ASIC.

Input charge maximum range	+/- 17 fC to +/- 70 fC
Gain for both polarities	10, 16, 20, and 40 mV/fC
Detector leakage compensation	Dynamic up to 4 nA/pixel
Minimum threshold (from 80 pixels)	5.3 keV
ENC @ 40 mV/fC (positive polarity)	133 e^- RMS
ENC @ 40 mV/fC (negative polarity)	160 e^- RMS
Discriminator jitter	< 10ns for E > 25 keV
Supply Voltage	+2.5 V
Power consumption	190 μW / pixel
TDC resolution	95.5 ps/ADC count
TDC precision FWHM	600 ps
TDC power consumption	130 μW
Temperature sensor sensitivity	0.4 Celsius degrees
Temperature sensor consumption	60 μW

Chapter 7

Fabrication and assembly of VIP PET prototype

The VIP project was from its conception a complex endeavour due to the challenges in both levels, hardware with an ultra-low-power ASIC design, the packaging of hybrid detectors, the stacking of multiple hybrid detector layers, and the cooling of the system, and software with the challenges in the energy and timing reconstruction from raw data, and the image reconstruction of highly pixelated PET acquisitions.

Within VIP project, simultaneously with the development of VIPPIX ASIC, packaging techniques were optimized using mechanical samples, and image reconstruction algorithms were developed using simulated data from GAMOS. Additionally, in case of failure of the final ASIC, the analysis of using a commercial readout ASIC from the VATA family was demonstrated [142]. Also, due to the many potential applications of the highly-pixelated detector module, other medical imaging devices were predicted by simulations [143-145].

Once the successful integration of the VIPPIX pixel electronics with the rest of the back-end electronics was demonstrated, the full integration of the final VIPPIX ASIC was realized and sent for fabrication. Due to the size of the chip (10.25 mm x 13.10 mm) and the large number of ASICs needed to complete the VIP prototype, an engineering run with twelve wafers was fabricated using full-set of mask production. Figure 37 shows the photography of the VIPPIX ASIC with labels of the different parts and its layout. The wafers are fabricated as all previous prototypes in TSMC 250 nm CMOS technology with mixed-signal components such as metal-insulator-metal capacitors of 1 fF/ μm^2 [146]. The pixel matrix is provided of an extra row of pads that connect the guard ring of the detector to a low impedance voltage reference through one input pad of the ASIC.

Note that digital and analog buses are separated in the pixel matrix. All digital pulses are generated in the digital controller and distributed symmetrically to all columns from the top while analog voltage references and current reference lines are fed from the bottom of the ASIC to the matrix to avoid digital crossings. Additionally, extra care was taken to shield digital lines with ground lines on top to avoid the coupling of digital fast transitions through the electrode plates of the detector.

After it was confirmed the fully functionality of the VIPPIX ASIC, the second phase, the design, packaging, and the commissioning of the VIP PET prototype based on the hybrid CdTe detector with VIPPIX ASIC started Figure 38 details the flow diagram of the construction of the VIP PET scanner.

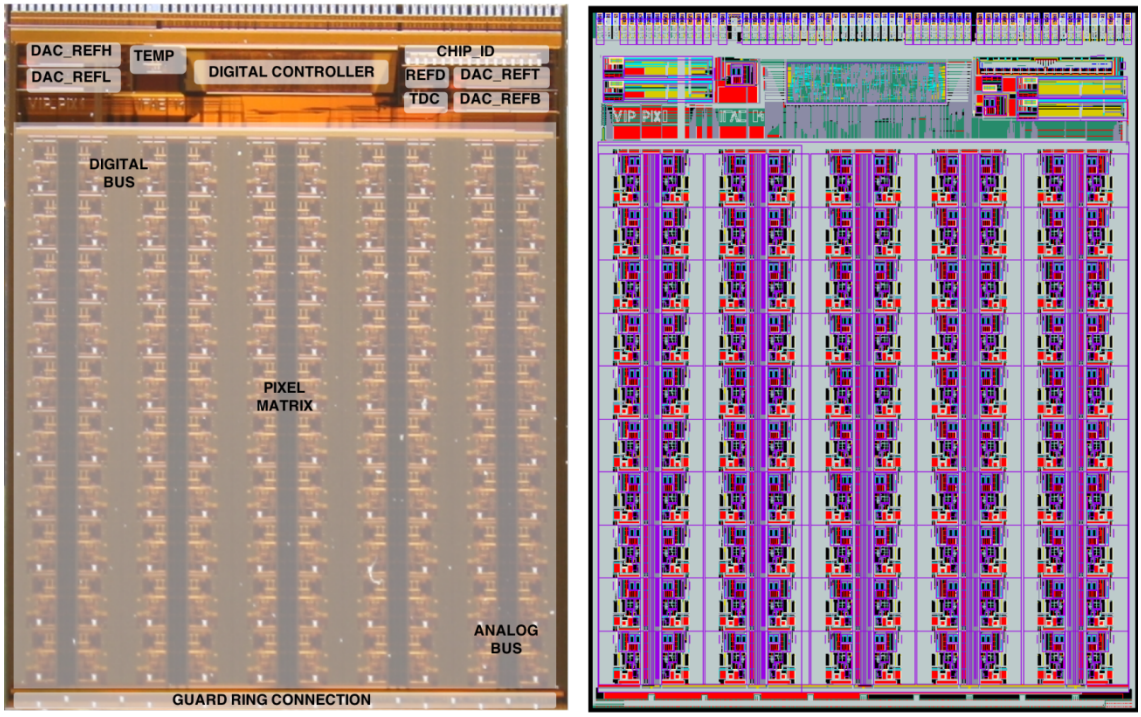

Figure 37. Illustrated photography of the VIPPIX ASIC and its layout.

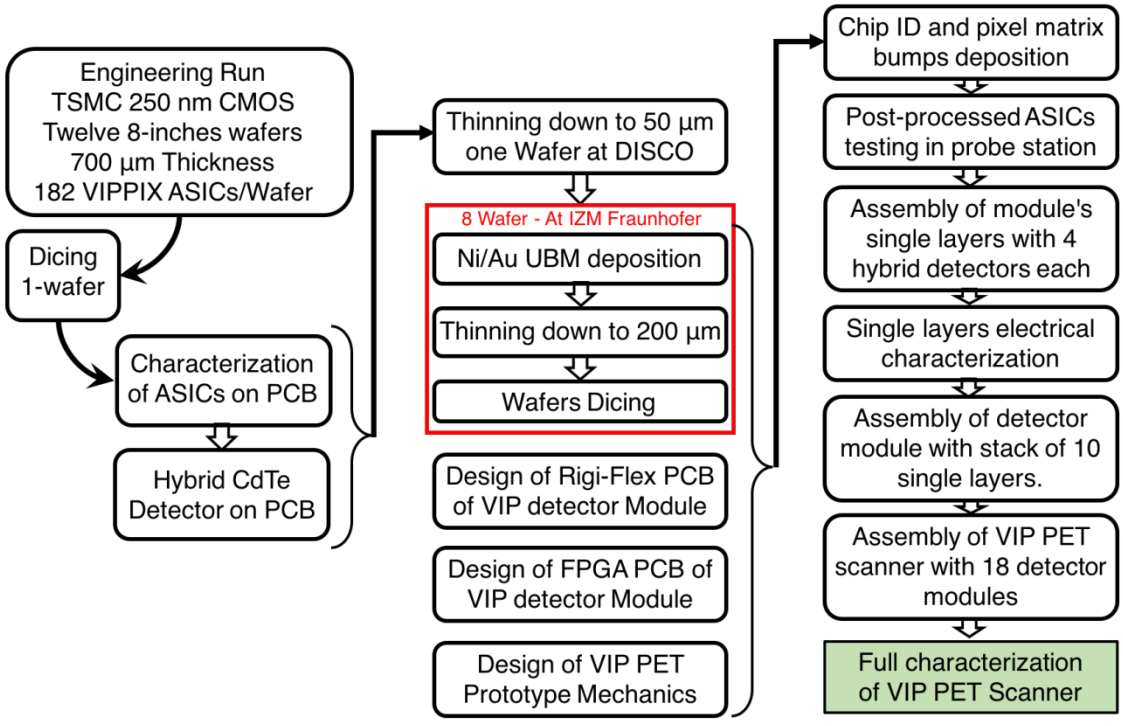

Figure 38. Flow diagram of the construction of the VIP PET scanner after the completion of the design of VIPPIX ASIC and the reception of 12 wafers from an engineering run from TSMC.

During the fabrication of the lithography masks and the 12 wafers of the engineering run, the mask of the CdTe detectors were designed. Figure 39 shows the layout with indications of the pixel and guard ring dimensions and the photography of the fabricated 10 x 10 pixel CdTe detector.

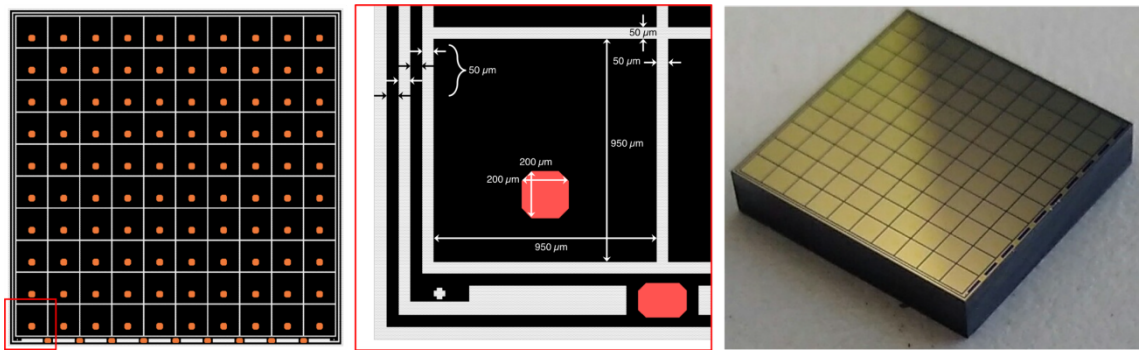

Figure 39. Layout and photography of the 10 x 10 pixel fabricated CdTe detector [150].

Once the twelve wafers were fabricated, one was sent to DISCO HI-TEC Europe GmbH for dicing the 182 useful VIPPIX ASICs that fit in each 8-inches wafer. Twenty ASICs were mounted on a testing PCB and their electrical characterization was performed to check all functionalities and the pixel energy and time resolution with high level of confidence. Additionally, five extra chips were post-processed with chemical gold deposition and bump-bonded to CdTe pixelated sensors. The performance of the pixels with the load of detector capacitance and possible couplings was characterized. Excellent and similar results were obtained with and without CdTe detector loading and leakage current. Therefore, since the results of the VIPPIX ASIC were satisfactory, the post-processing of the rest of the wafers, the design of the PCBs for the VIPPIX hybrid detectors, and the assembly of the VIP PET prototype could start.

Originally, grinding of the wafers down to 50 μm was planned to reduce the dead material of 700 μm ASIC thickness. For this reason, one wafer was sent to DISCO HI-TEC Europe GmbH for dicing and thinning down to 50 μm. Based on the difficulties during handling the wafer at our facilities and an unexpected residual layer deposited in the input/ouput pads of the ASICs, we decided to work with Fraunhofer IZM Institute were the complete post-processing of the wafers was performed. The under-ball-metal (UBM) mask was developed from the polyimide opening design of VIPPIX. The 60 μm diameter pixel input aluminium pad was enlarged to an hexagonal golden pad of 200 μm diameter for 250 μm diameter bumps in the detector bump-bonding process. The design and the manufacturing of the VIP module PCBs were also realized simultaneously.

The working principle of VIP PET is based on single layer independent operation and communications, i.e., every single layer of each of the 18 modules of the ring is provided with an FPGA that controls the four hybrid detectors in the layer. Therefore, the VIP detector ring prototype is based on 72000 pixels working independently controlled by 180 FPGAs that communicates with external controller synchronously when at least one hit occurs in one of the four detectors in its layer. To increase the yield of the gamma-ray detector module, every layer is composed of two well differentiated parts connected with a flat low-profile connector: a rigid-flex PCB where the four ASICs plus CdTe detectors are connected, and a rigid PCB

with the FPGA and proper DC filtering of supplies and detector's high voltage biasing voltage. Photography of the rigid-flex PCB with four mounted hybrid CdTe detectors and with naked VIPPIX ASICs (left) and the FPGA rigid PCB (right) are shown in Figure 40.

Once all ASICs needed for the prototype were post-processed and arrived to IFAE, their chip-ID was programmed. The chip-ID cell is based on 16 open-circuit pads with pull-up resistors. Shorting a pad to its corresponding ground pad with a solder ball writes "0" on that bit. Figure 41 shows the layout of the chip-ID cell (left) and the photography of four positions of a programmed chip-ID with two open circuits and two shorted pads for '1001' word. BiSn bumps of 80 μm diameter were deposited in house according to every ASIC's 16-bit chip-ID word. Due to the rectangular shape of VIPPIX, wafers contain 13 rows and 17 columns of useful ASICs. Therefore, the 16-bit chip-ID of the VIPPIX ASIC is encoded with wafer number (5 bits), row number (4 bits), and column number (5 bits), with extra two most significant bits for debugging purposes.

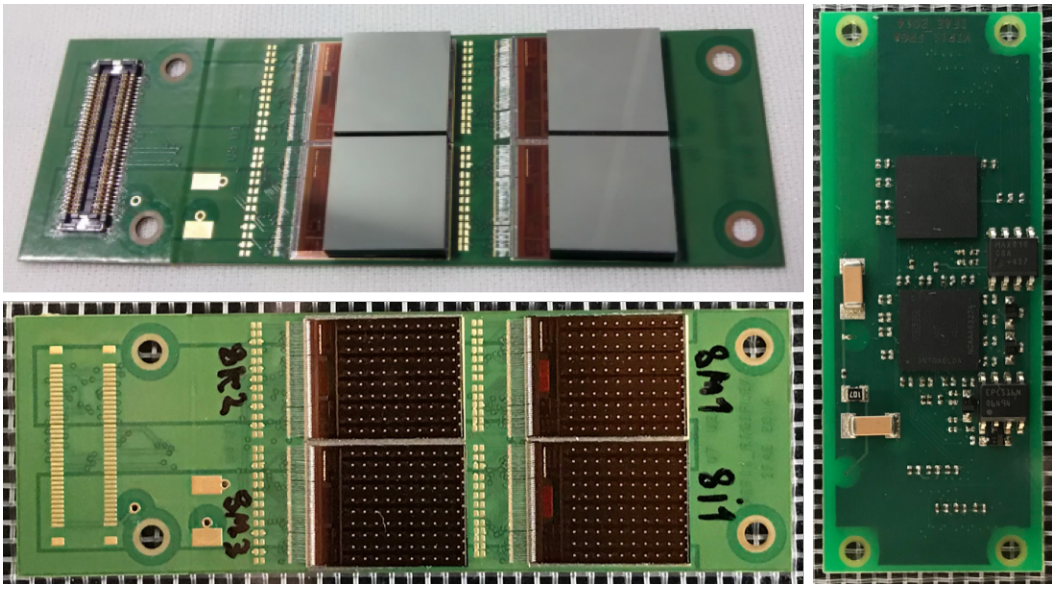

Figure 40. Rigid-flex PCB with 4 CdTe hybrid detectors based on pixelated CdTe bump-bonded to a VIPPIX ASIC (top-left), without CdTe detectors (bottom-left), and FPGA rigid-PCB (right).

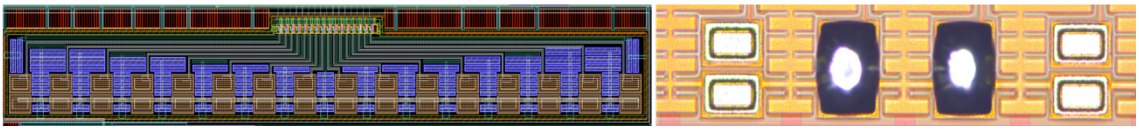

Figure 41. Layout of the 16-bit Chip-ID cell (left) and detailed photography of 4 bits with two open circuits and two shorted pads equivalent to '1001' (right).

After identification, all ASICs were characterized with a 50-pin probe designed to match the I/O pads of the chips. In order to classify their performance level, the DC power consumption, the pixels' noise level, and the functionality of pixels' ADCs, TDC, Temperature Sensor, and Digital controller were fully checked in every ASIC. Quality wafer maps as the

ones shown in Figure 42 were obtained and used for the selection of the best quality ASICs to produce the VIP detector modules.

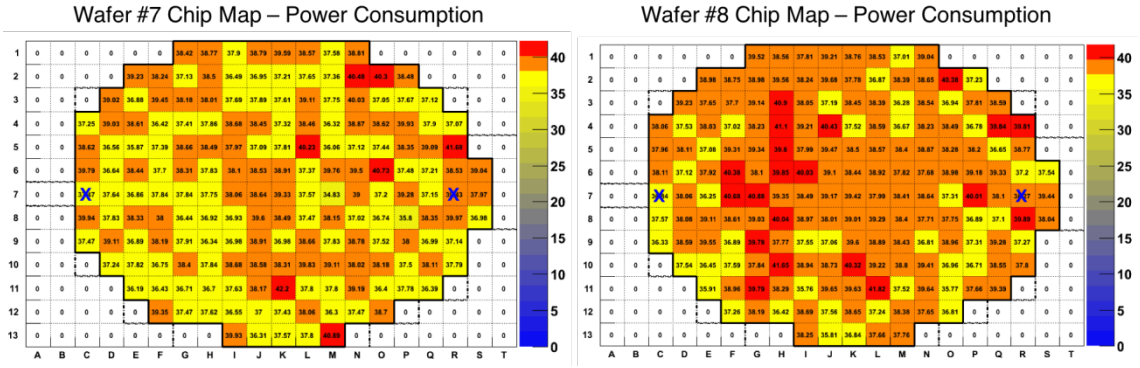

Figure 42. Quality wafer maps of ASIC total current consumption for wafer #7 and wafer #8 (all measurements are in mA).

VIP detectors were then bump-bonded to VIPPIX ASICs with BiSn bumps of 250 μm diameter as designed originally. Every 4 hybrid detectors were mounted in one single layer rigid-flex PCB (Figure 40 – left) by wire-bonding the input/output pads of the ASICs to the matching PCB lines. Every single layer was then characterized to identify possible malfunctions during the mounting process. Once ten layers were fully operative, a detector module with 10 single layers was assembled. Figure 43 shows a photography of the first finalized VIP detector module.

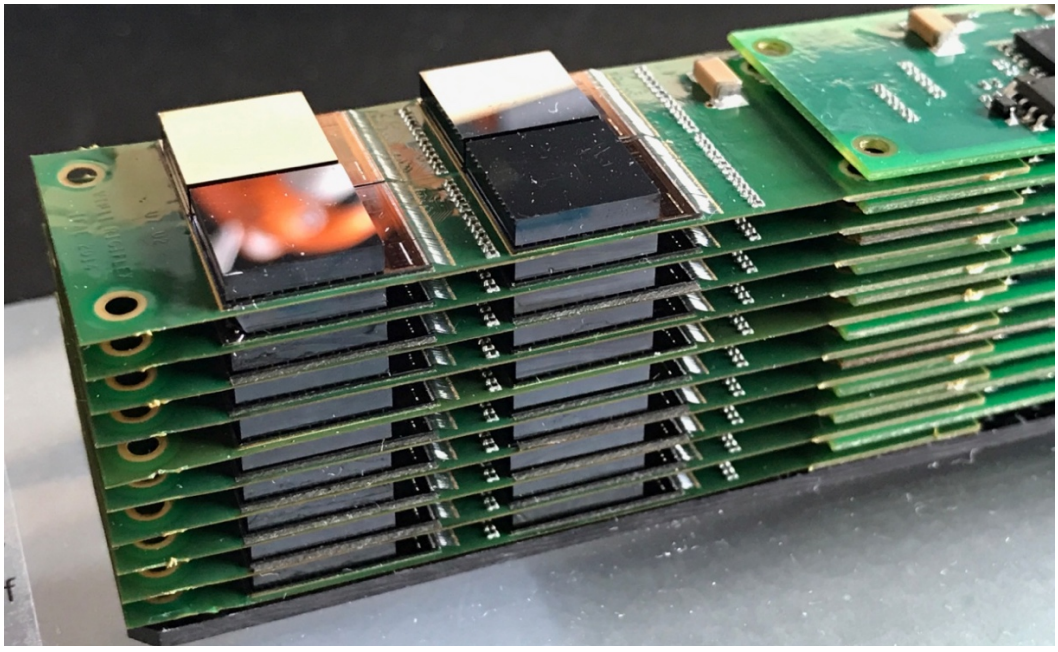

Figure 43. First assemble VIP detector module with 40 hybrid detectors and 4000 independent readout channels.

The VIP detector module is the main building block of the VIP PET ring. The mechanical engineers at IFAE realized the design of all different parts of the ring, including the cooling system based on mechanical and thermodynamic simulations. In Figure 44 we can observe a view of the 3D CAD model of the full ring structure and the module ring in perspective. The solid frame was fabricated with steering steel while all the walls, bottom and top covers were realized in Carbon fibre. The assembly of the full VIP PET ring was finalized in mid 2017. Figure 45 shows a photography of the completed VIP PET scanner prototype.

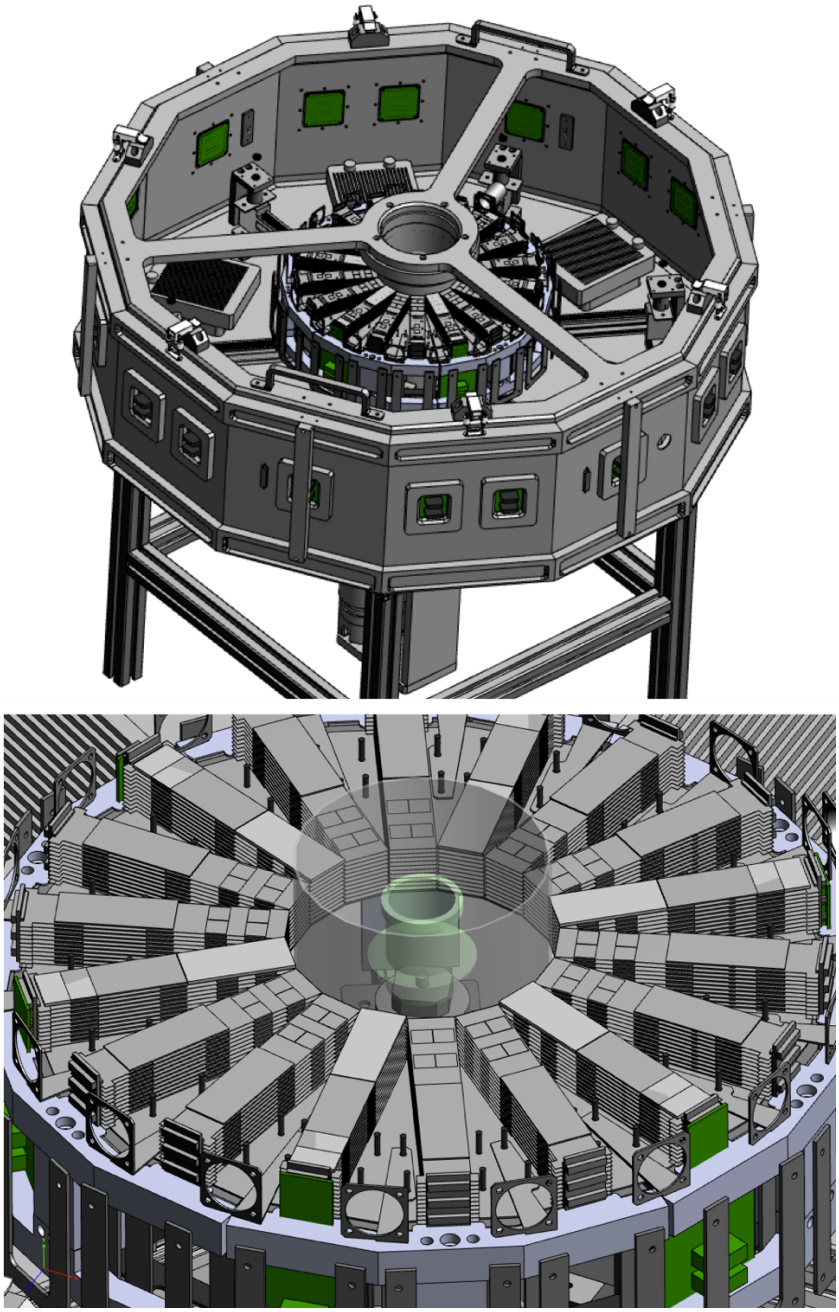

Figure 44. 3D CAD design of the full VIP PET scanner prototype and detail of the detector module ring.

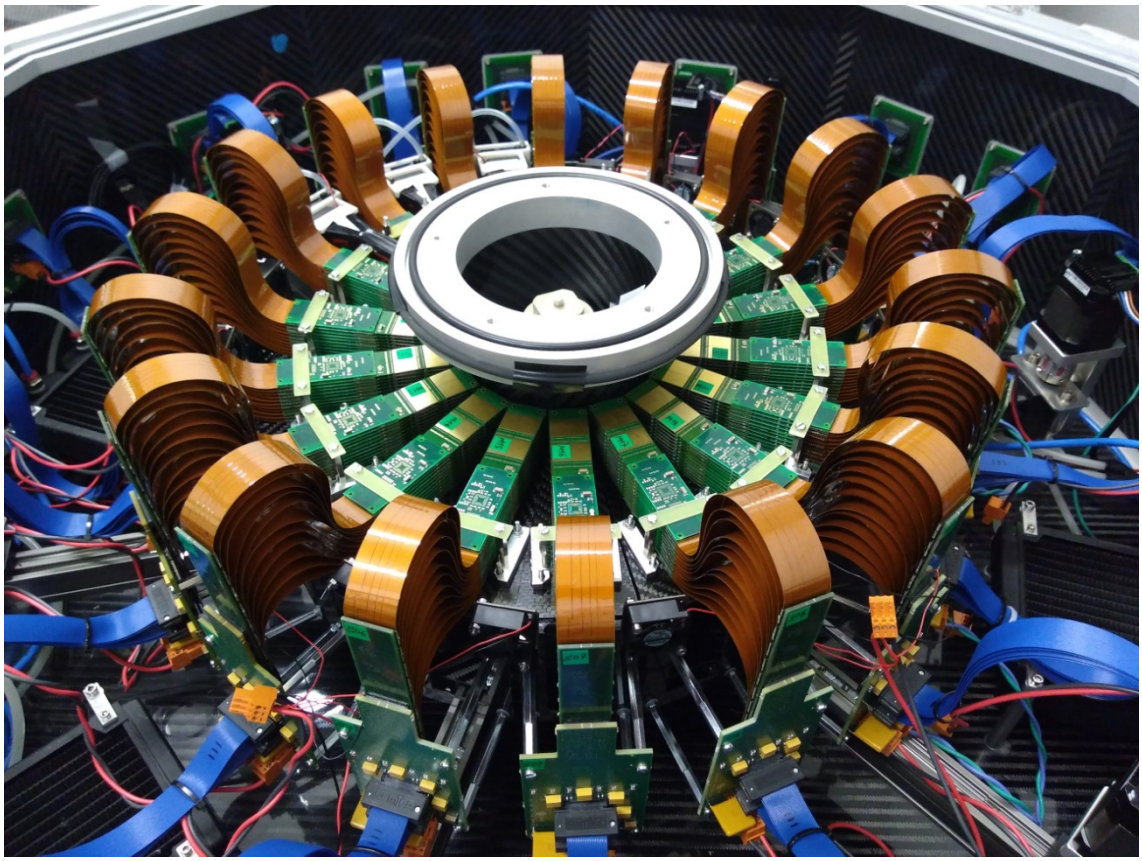

Figure 45. Photography of the completed VIP PET scanner. Walls, bottom and cover are made of Carbon fibre. Every single detector layer in every module is connected with a long flexible PCB to a vertical PCB where all buses are collected including the high voltage bias of the detectors. Modules can be placed at different radial position to characterize the performance with different field of view. The radial position for small animal PET scanners is shown.

The VIP PET scanner composes of 18 detector modules with a total of 180 FPGAs synchronized by the same time reference to provide coincidence timing recognition, and with 720 CdTe detectors biased at the same high voltage. Every module contains 4000 voxels of CdTe with independent readout electronics.

Once fabricated and characterized layer by layer in terms of functionality, the full VIP scanner must be equalized prior to image acquisitions to achieve the desired energy and timing resolution. The equalization procedure and the first achieved results of VIP PET prototype are presented in next section.

Chapter 8

Equalization and first results of the VIP detector module

The absolute gain of every pixel front-end electronics is randomly distributed across the pixel matrix and follows a Gaussian probability function since it depends mainly on the absolute value of the preamplifier's feedback capacitance which is geometrically dependent. In 2D imaging readout ASICs, especially in photon counting mode, the gain and the threshold energy of all pixels should be equalized to reduce the effective noise which can be analysed with flat image corrections. Nevertheless, for 3D position, energy, and time readouts as for VIP detectors, the performance of every pixel is analysed in calibrated independently.

Therefore, a pixel matrix could have a gain dispersion of 50 % and still obtain excellent individual spectroscopy provided the linearity curve of every pixel is properly characterized and calibrated with radioactive sources. Indeed, a proper calibration of all 72000 pixels with the peak energies of several radioactive sources must be performed after a first relative-linearity equalization procedure.

To perform such a first characterization of the linearity of the energy path readout electronics, every pixel of the VIPPIX ASIC is provided with two independent test pulse circuits. One based on internal current generation with a 5-bit current DAC and an external pulse width control, and another based on a test pulse capacitor that matches the feedback capacitor value of the preamplifier. The limited linearity of the internal current DAC was characterized using the analog test pulse circuit since the charge injection is based on a fixed capacitor value and an external waveform generator with typically 0.1 % linearity at full range.

The equalization algorithm for every pixel is represented in Figure 46. Initially, all pixels are set to minimum preamplifier pulse width and maximum shaper peak time. A very short baseline restore time of the preamplifier pulse is obtained with small equivalent feedback resistor what minimizes the output voltage offset due to detector leakage out of the leakage compensation range. When the leakage of the pixel detector is larger than the dynamic compensation range of a pixel, increasing the feedback resistivity moves the baseline of the preamplifier and increases the baseline restoring time non-linearly. Therefore, the pixel equalization process is performed in every leakage compensation range. By analysing the dynamics of the baseline offset with the feedback resistor at different leakage compensation range we can characterize the actual pixel detector's leakage current, and the proper compensation range can be selected.

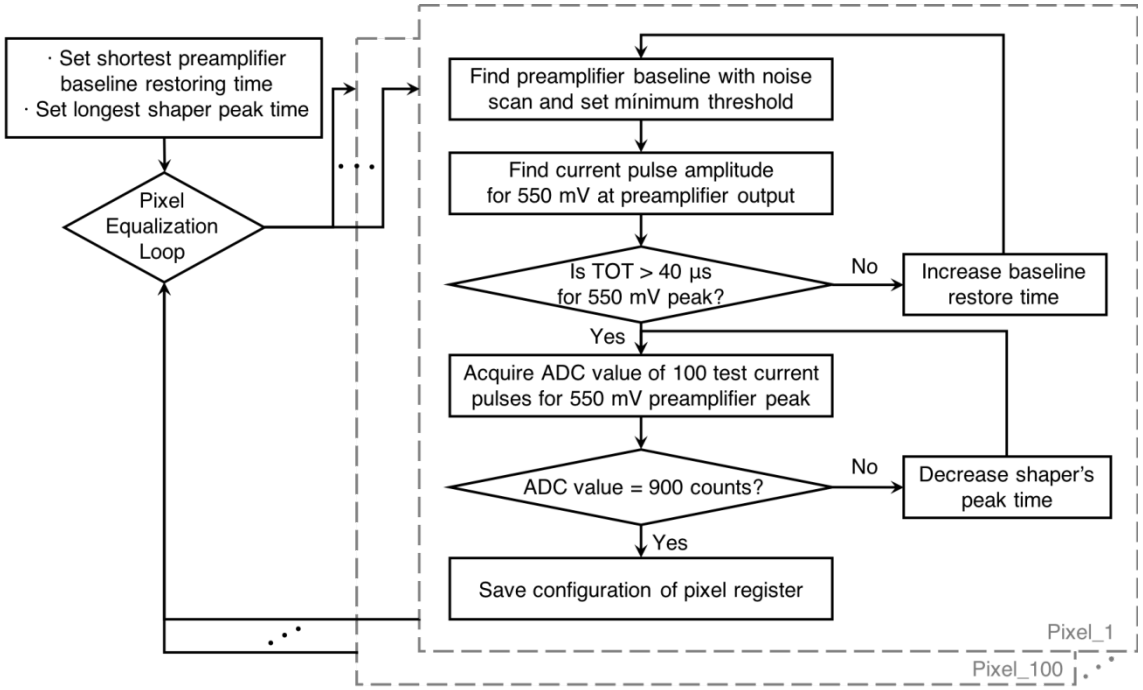

Figure 46. Flow diagram of the pixel's equalization algorithm.

The complete calibration of the PET scanner is realized in three phases: first, the equalization of all pixels is performed applying continuous high voltage bias to the detectors; second, long acquisitions with high voltage power cycles but without radioactive sources are taken to obtain the pedestal values of every pixel and to shut down those pixels which create sudden electrical discharge firing continuously the pixel acquisition procedure due to local defects inside the detector; and third, the spectroscopy of different radioactive sources is obtained to calibrate properly the linearity curve of every pixel. The radioactive isotopes used are Barium-133 (81 keV, 303 keV, and 356 keV), Cobalt-57 (122 keV and 136.5 keV), Americium-241 (59 keV), and Sodium-22 (511 keV). Due to the high stopping power of CdTe, small fraction of the photons of 59 keV, 80 keV, 122 keV and 136.5 keV don't reach the outer pixels of the detector ring. Therefore, the peaks above 300 keV are used to fit their response to the relative linearity curve obtained with internal test pulses.

The timing response of the pixels is also characterized versus the energy of the photon interaction. Once the absolute gain is calibrated, the delay of the trigger versus the equivalent energy of the injected test pulse is characterized to minimize the dispersion and improve the coincidence time window.

In the fifth and last article of this thesis, the first results of a part of the VIP PET scanner prototype are presented in terms of time resolution and energy resolution. Such a highly-pixelated detector volume with such an individual excellent energy resolution allows to reconstruct the peak of 511 keV of positron emission by summing two Compton interactions coming from a 511 keV photon.

8.1 Summary of article "First results of a highly granulated 3D CdTe detector module for PET"

In this article, we present the first experimental results of five fabricated VIP detector modules placed inside their PET ring positions in terms of energy resolution, coincidence time resolution, and spectroscopy. The original geometries of VIP PET ring, detector layer and detector modules are detailed in the first article of this dissertation. Nevertheless, since the fabricated detector modules differ from original specifications in terms of shape and number of CdTe detectors, they are described in detail. Additionally, the performance of the fabricated VIPPIX ASIC and the energy calibration of the hybrid detectors are discussed.

8.1.1 Materials and methods

As shown in Figure 39, the shape of the pixel matrix of the fabricated detectors is squared and not trapezoidal as originally designed for a seamless detector ring for higher detection efficiency. Square detectors will be useful for different geometries such as Compton Camera and Positron-emission mammography scanners [144,147]. The metallization profile of the fabricated Schottky detectors was Platinum (continuous electrode) – Cadmium Telluride (2 mm thickness) – Aluminium – Titanium – Gold – Nickel – Gold – Aluminium Nitride Passivation (pixel electrodes). Ti-Au-Ni-Au under ball metallization was necessary for bump-bonding process with BiSn solder balls. Pixelated matrix is surrounded by an electrically connected double guard ring. Due to Schottky interface polarization, power cycles of 90 seconds of data acquisition and 85 seconds of detector recombination must be used to keep detector's leakage current under control.

The VIPPIX ASIC of 10x10 pixel readout channels is presented and the pixel electronics and the back-end electronics are referred to the third and fourth article of this dissertation.

The detector module is based on the stack of 10 single layers with a 2 x 2 matrix of assemblies of CdTe detectors bump bonded to VIPPIX ASICs. Every ASIC is glued to the 255 μm thickness multilayer flex-PCB and its 50 input/output pads are wire-bonded to their matching golden lines as shown in Figure 40. The high voltage connection of detectors in layer n is provided by the flex-PCB bottom connection of layer n+1 via an electrically conductive 50 μm thickness double-sided tape. The stacked detector contains 4000 independent channels in a 2 cm x 2 cm x 2 cm volume what results in a true 3D detector with millimetre geometrical information of the impact points.

In this paper, the performance of 5 VIP modules distributed inside the PET ring as illustrated in Figure 47 is reported. Due to limited cooling efficiency, during operation the temperature of the detectors reach values larger than 35 Celsius degree so pixel's leakage current at voltages higher than 500 V was too large and the behaviour of the pixel detectors not under control. Therefore, power cycles to a minimum of -500 V (i.e. -250 V/mm) were used.

A Derenzo phantom filled with ^{22}Na and an activity of 550 kBq was used as radioactive source to characterize the trigger rate, energy resolution, coincidence timing resolution, and spectroscopic performance of the 5 modules. The analysis of data is performed offline since events are reported in list mode continuously during acquisition.

Every entry in the list contains the pixel ID, the energy deposited, and the time stamp. The pixel ID is used offline to locate the interaction 3D coordinate, the energy of the interaction plays a fundamental role in the classification of the events in pure 511 keV photoelectric, Compton scattering, or photoelectric of scattered photon, and the precise time stamp is necessary to match events from the same photon in case of Compton scattering, or from two back-to-back photons.

8.1.2 Results

The VIPPIX ASIC is fully functional, provides high energy resolution and sub-nanosecond TDC information of the trigger generation. Nevertheless, it suffers from some unexpected malfunctions such as that 5 % of the ADCs show a conversion problem and the corresponding pixel must be shutdown, or that unwanted coupling of digital pulses inside the pixel matrix to the detectors input pads set the minimum trigger threshold at 50 keV approximately. Additionally, the power consumption of the digital back-end working at 40 MHz represents 80 % of the consumption of the complete ASIC. Therefore, from 200 μW per pixel reported power consumption, an equivalent of 1 mW per channel is dissipated finally.

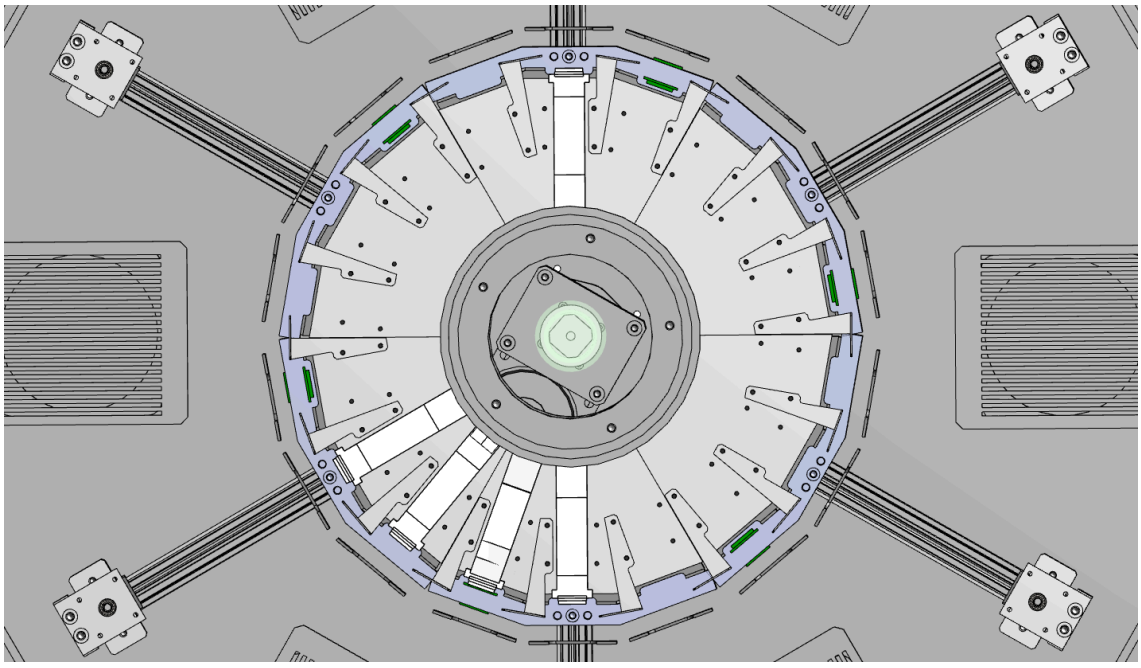

Figure 47. Distribution of the 5 VIP detector modules inside the VIP PET ring.

From 20000 pixels in the five modules, 89 % were fully operational so their energy and timing performance was characterized. Their linearity was calibrated using Barium-133 and Sodium-22 peaks and the average absolute gain was 0.7 keV per ADC count. The time coincidence resolution of positron emission back-to-back photons show a coincidence time resolution of 60 ns FWHM. The time coincidence resolution of photons that underwent

Compton scattering larger than 200 keV is 70 ns FWHM. Such large window is due to a very low detector's biasing voltage and the effect of small pixel geometry.

The spectroscopy of ^{22}Na is obtained with pure photoelectric in coincidence and with Compton plus photoelectric coincidence events. A resolution of the 511 keV peak of 2.2 % FWHM and 3.2 % FWHM was obtained with detector bias of -250 V/mm, 2 mm thickness detectors, and 30 Celsius degree average temperature.

8.1.3 Conclusions and future work

The energy resolution, coincidence time resolution, and spectroscopy results of five VIP detector modules are reported. The fabricated modules differ from original trapezoidal design due to budget limitations and strategic decision to use the same detector technology for a prototype of a Compton Camera and a Positron Emission Mammography scanner. First spectroscopy results show an energy resolution at minimum biasing voltage of -250 V/mm of 2.2 % FWHM for 511 keV peaks of Sodium-22 radioactive source. A 3.2 % FWHM resolution is obtained by summing two hits with one Compton scattering interaction. This feature is a consequence of the high granularity detector and the individual excellent energy resolution of every pixel and enables the implementation of Compton cameras.

The coincidence time resolution of 511 keV photons undergoing a photoelectric interaction is 60 ns FWHM. Such a long coincidence window is due to the detectors dynamics, specifically the long collection times of holes at -250 V/mm and additionally the loss of induced electric field due to the pixel effect.

Based on the excellent performance in terms of energy and spatial resolution, and based on the low activity of the radioactive Derenzo phantom, the VIP PET scanner prototype should be able to reconstruct the small-animal PET phantom and to see the 0.75 mm diameter rods with few millions PET coincidences. Since the full PET prototype has been completed, image quality characterization will be reported in VIP's project next publication.

Chapter 9

Conclusions and future work

The main and most relevant conclusion of this work is that a PET scanner prototype based on pixelated CdTe detectors and dedicated readout ASICs has been successfully fabricated from the conceptual idea until its characterization with radioactive sources. In the original proposal of VIP pathfinder project two detector modules were proposed as final deliverable. Instead, a full ring with eighteen modules but with smaller number of layers and detectors in each module has been produced.

To achieve these results, several challenges have been faced and overcome in the past years. At the level of software, three main algorithms have been developed successfully: the equalization and characterization procedure of the pixelated PET, the coincidence hits identification algorithms, and the image reconstruction algorithms.

From a hardware perspective, the VIP PET scanner is based on four main components: pixelated CdTe detectors, pixelated readout ASICs, packaging and external digital control, and mechanics and cooling systems. Among the four components, to develop from the conceptual design to the wafer fabrication an application specific integrated circuit of the complexity and size of VIPPIX takes the highest risk due to the large amount of needed resources. Therefore, having a successful ASIC meant already by itself a big success for the project.

In this dissertation, the most relevant publications of the development and characterization of the VIP detector technology are presented. First, the PET ring has been simulated following international standards for brain and whole-body PET scanners as well as for small-animal PET prototypes. The simulated performance shows that VIP PET is closer to the resolution limits of positron emission tomography than any commercially available or published PET scanner. Such feature is accomplished by having more than 6 million detector voxels of CdTe with excellent spectral resolution and precise time stamp generation.

Using CdTe detectors provides excellent sensitivity which combined with the very low noise in the “Line of Response” identification reduces dramatically the number of million coincidences necessary for a high-quality image generation. A direct consequence is the flexibility for medical doctors either to reduce the radiopharmaceutical intake dose and to use current scanning times (up to 90 minutes for whole body scan), or to reduce to tens of seconds the scanning time with the activity of 31.6 MBq in the human brain.

The performance of CdTe detectors depends strongly on the thickness of the detector, the applied bias voltage, and the temperature. Experimental results of 2 mm thickness detectors working in optimum bias and temperature conditions show a spectral resolution of 1.6 % FWHM and 6 ns FWHM time coincidence resolution of 511 keV photopeak of Sodium-22 radioactive source. These results were used in the simulations of the VIP PET scanner as an upper limit of the performance of the detector.

Instead of commercial electronics, the VIP detectors should be readout with a dedicated and pixelated readout ASIC. Commercial spectroscopic readout ASICs don't focus in timing, and time of flight ASICs don't offer excellent energy resolution either. Therefore, the design of VIPPIX ASIC combined features of both applications, spectroscopy and time stamp precision measurement for PET, Compton Camera, and PEM applications based on pixelated CdTe detectors.

The presented VIPPIX ASIC is composed of a 10 x 10 pixel array, a global time to digital converter, 5 voltage DACs, a temperature compensated current generator, a temperature sensor, a 16-bit chip ID, and a global digital controller. The pixel electronics work with both biasing polarities of the detector and include a preamplifier with dynamic leakage compensation circuit and baseline restoring feedback active resistor, a pulse shaper, a peak and detect circuit, a pulse discriminator with offset compensation, a 10-bit digital to analog converter and a local digital controller.

Every pixel electronics is optimized for pixelated CdTe detectors. Since the charge collection efficiency of the detector depends on several factors, the architecture of the pixel was chosen to minimize their effect in the spectral and timing resolution. Most of the integrating, shaping, and dynamic features of the pixel are adjustable to find the optimum working point and to offer the best performance for every biasing condition of the detector. An equalization and calibration procedure have been developed, and it is implemented in the measurement protocol. For every detector condition, i.e. working temperature and biasing voltage of the detector, the VIPPIX ASIC must be optimized prior to data acquisition. Due to the independent performance of every pixel, such optimization procedure can be realized in parallel for all channels of the VIP ring.

The results of the front-end electronics and a small 4x4 pixel array mini-VIPPIX prototype were published prior to the fabrication of the VIPPIX ASIC and have been presented here. Based on the successful performance of the prototypes, twelve wafers of VIPPIX have been fabricated and properly characterized on wafer. Among all the available chips, 720 have been used to build the detector modules of the VIP PET prototype.

The energy resolution, time coincidence resolution, and spectroscopy performance of five detector modules with 4000 pixels per module have been characterized with Sodium-22 radioactive source after their equalization and calibration with other radioactive sources were applied and they are presented here. Due to the power consumption of the VIPPIX ASICs plus the FPGAs and a limited cooling efficiency of the PET structure, detectors operated at 35 Celsius degree average. Consequently, reduced biasing voltage of -500 V were used to keep the leakage of the detectors within the compensation limits of VIPPIX pixel electronics. Unfortunately, working with such low bias voltage limited the charge collection efficiency and timing precision of the Cadmium Telluride detectors.

Around 18000 pixels out of the 20000 were fully operative. This number means a 90 % yield approximately. VIPPIX's ADC design has a bug related to fabrication process which disables 5% of the ADCs in the chip on average. The other 5 % of dead channels is a result of a combination of failures in the packaging process of every layer, and a limited number of

pixels were the leakage current of the detector increased out of control during operation, so they had to be disabled.

The published performance shows an energy resolution of 2.2 % FWHM for the Sodium-22 peak at 511 keV for PET coincidences based on individual performance of 18000 pixel detectors at -500 V and 35 Celsius degree on average. Since VIP's pixel detector shows such an excellent energy resolution, detecting photons that underwent one Compton interaction inside the detector volume is possible. By summing the energy of Compton – PET coincidence events the peak of 511 keV is reconstructed with a resolution of 3.2 % FWHM. The degradation of the signal to noise ratio comes naturally from the noise propagation summing individual pixel detector energies.

Although 2.2 % FWHM is already an excellent resolution, there is still room to improve. Detectors can be biased at higher voltage to improve charge collection efficiency, especially holes collection. If detector bias can't be increased, the limitations of charge collection efficiency can be compensated by measuring the depth of interaction inside the detectors. Additionally, the charge sharing among adjacent pixels can be compensated by summing their energies offline. This feature was already implemented in the VIPPIX ASIC so for every detected event, the chip provides the energy of the central pixel and the adjacent ones. Unfortunately, due to a malfunction in the reset procedure of the non-triggered pixels, the energy of the surrounding pixels is corrupted and can't be used to compensate charge sharing in the current VIPPIX design.

The timing performance of coincidence detection is also published. For PET coincidence events, the system shows a resolution of 60 ns FWHM. This result differs dramatically from the performance presented in the second article of this thesis with a planar CdTe detector biased at -2000 V at -8 Celsius degree where it was claimed 6 ns FWHM coincidence time resolution. Such a big discrepancy triggered the alarm of a possible problem in the pixel front-end electronics. Indeed, a dramatic increase of the rise time of the preamplifier caused by the post-processing to the wafers was discovered. The rise time of preamplifiers without UBM deposition was shorter than 200 ns whereas for those with 200 μm golden pads at the input signal it increased to 1000 ns approximately.

The timing performance of the VIPPIX pixel matrix shows a coincidence resolution of 12 ns FWHM when test pulses of different amplitude but the same injection time are used. Therefore, spreading to 60 ns might be caused by the uncertainty induced by the depth of interaction combined with the low detector bias voltage. Further debugging and dedicated test setup is necessary to clarify the wide uncertainty time window of actual VIP PET. Despite the low timing resolution of actual VIP detector, the full detection ring is ready to acquire PET images using a Derenzo phantom filled with 22Na according to NEMA NU 4-2008 since the activity levels are well below the limitation imposed by the 60 ns FWHM coincidence time resolution.

A summary of the published results presented in this thesis is in Table IX.

Table IX. Summary of the published results of VIPPIX ASIC and VIP detector module.

Simulated Results of VIP Brain PET Scanner for NEMA NU 2-2001	
Scatter Fraction (%)	3.95
Noise equivalent count rate peak (kcps)	122
Noise equivalent count peak activity (MBq)	31.6
Radial, Tangential, and Axial resolution at 100 mm radial position (mm)	0.7, 0.9, 1.9
Sensitivity (cps/kBq)	14.37

Simulated Results of VIP Brain PET Scanner for NEMA NU 4-2008	
Scatter Fraction (%)	0.73
Noise equivalent count rate peak (kcps)	908
Noise equivalent count peak activity (MBq)	54.9
Radial, Tangential, and Axial resolution at 100 mm radial position (mm)	0.6, 1.4, 1.5
Image Recovery Coefficients for 1mm, 2mm, 3mm diameter rods in water	0.09, 0.32, 0.58
Flat Image uniformity minimum, maximum, and mean in water	0, 1.2, 0.798
Cold regions filled with water spill-over-ratio in water surrounding	0.168
Measured Performance of a 4x4x2 mm^3 CdTe detector at -8 Celsius degree and -2000V	
Energy resolution for 511 keV peak of Na^{22} source (% FWHM)	1.2
Coincidence time resolution for 511 keV photons of Na22 (ns FWHM)	6.0
Specifications and measured performance of the VIPPIX ASIC	
Matrix size (pixels)	10 x 10
Pixel size (mm^2)	1 x 1
Pixel double polarity input dynamic range (fC)	17, 35, 70, 140
Pixel pulse shaping time (us)	2 – 20
Pixel dynamic leakage compensation ranges (nA)	0.5, 1, 2, 4
Pixel energy conversion equivalent noise charge (e- RMS) (pos, neg)	133, 160
Pixel minimum threshold energy (keV)	5.3
Pixel jitter for energy higher than 25 keV (ns)	< 10
Pixel power consumption (uW)	190
Global TDC precision (ps / ADC count)	95.5
Global TDC full range (ns)	100
Global TDC resolution (ps FWHM)	600
Temperature sensor sensitivity (Celsius degree)	0.4
ASIC maximum hit rate (Hz)	6000
ASIC supply voltage (V)	+2.5
ASIC total power consumption (mW)	100
ASIC total size (mm^2)	10.2 x 13.1
Average resolution of 122 keV ^{57}Co peak with 100-pixel VIP Cadmium Telluride detector biased at -1000 V at room temperature [151]	3.23 % FWHM
Specifications of VIP PET ring	
Number of detector modules	18
Number of layers / module	10
Number of hybrid detectors / layer	4
Inner radius (mm) / Axial field of view (mm)	65 / 27
Calibrated pixel gain (measured with 17838 pixels) (keV/ADC count)	0.7
Minimum threshold energy (keV)	50
Energy resolution of 511 keV peak of two full photoelectric at room temperature and at 250 V/mm	2.2 % FWHM
Energy resolution of 511 keV peak with 1 Compton + 1 Photoelectric at room temperature and at 250 V/mm	3.2 % FWHM
Coincidence time resolution of full photoelectric photons at room temperature and at 250 V/mm	60 ns FWHM
Coincidence time resolution of 1 Compton + 1 Photoelectric total 511 keV at room temperature and at 250 V/mm	70 ns FWHM

Future work

As mentioned above, the VIP PET ring prototype has been fabricated and assembled completely. Therefore, the next step is to perform image quality tests based on the international standards for human brain PET diameter and for small-animal PET diameter. For that purpose, a point like source phantom has been designed and acquired, and will be used to characterize the spatial resolution of the detector ring.

Thought the published results are excellent for a first prototype device, they differ from the expected original specifications. Therefore, several actions are needed using the actual prototype to investigate the origin of the actual limitations:

- A revision of the equalization algorithm is necessary since the baseline drift due to large detector's leakage current is included only partially in the current procedure.
- A coincidence setup with the energy and timing readout from the cathode must be implemented to calibrate the depth of interaction and correct for the charge collection energy and time limitations.
- A setup based on a single detector and a sub-mm spot flashing laser is needed to test the reset functionality and the limitation of adjacent channels energy sum.

The architecture of VIPPIX pixel front-end needs to be revised for a future VIPPIX_2 ASIC according to the following requirements:

- The performance of the energy and the trigger generation should be independent of the leakage current of the detector.
- The input stage should be redesigned for 1 pF detector capacitance and should consume most of the power consumption of the complete pixel electronics since energy resolution and time resolution depend mostly on its performance. Considering the total ASIC power dissipation, the equivalent pixel's power consumption should be reduced to 50 μW.
- The depth-of-interaction must be measured in every pixel for every event to improve timing and energy resolution.
- The architecture and the design of the SAR ADCs should be redesigned to increase the robustness against process and temperature variations.
- The ASIC digital controller needs updates to lower the power consumption and the ASIC dead time.

Additionally, at least two extra articles will be published in the coming months. One with the energy and time coincidence results of the full PET ring and the image quality characterization, and another with the full characterization of the VIPPIX ASIC.

Bibliography

[1] Online Resource: http://cordis.europa.eu/project/rcn/94710_es.html

[2] Online Resource: http://www.vip-erc.com/pet.html

[3] Valk, P.E., et al., eds. "*Positron Emission Tomography. Basic Science and Clinical Practice*". 2003, Springer: Heidelberg.

[4] ME Phelps. "*Molecular imaging with positron emission tomography*". Annual Review of Nuclear and Particle Science. 2002; 52: 303-338

[5] KA Wood, PJ Hoskin, MI Saunders. *"Positron Emission Tomography in Oncology: A Review".* Clinical Oncology. 2007 19: 237-255.

[6] Gutfilen, B., Valentini, G., "*Radiopharmaceuticals in Nuclear Medicine: Recent Developments for SPECT and PET Studies*," BioMed Research International Volume 2014, Article ID 426892, 3 pp.

[7] Weber, D, Eckerman, K, Dillman, L et al, "*MIRD (Radionuclide Data and Decay Schemes)"* . in: Society of Nuclear Medicine, New York; 1989:447.

[8] S. R. Cherry, J. A. Sorenson, and M. E. Phelps. "*Physics in nuclear medicine"*. Saunders, 3rd edition, 2003

[9] S. DeBenedetti, C. E. Cowan, W. R. Konneker, and H. Primako, "*On the angular distribution of two-photon annihilation radiation"*, Physical Review, 77(2):205 212, January 1950.

[10] Suleman, S. "*Update on time-of-flight PET imaging*", Journal of Nuclear Medicine, 2015 January; 56(1): 98-105. doi:10.2967/jnumed.114.145029

[11] Defrise, M., A. Geissbuhler, and D.W. Townsend, "*A performance study of 3D reconstruction algorithms for positron emission tomography"*. Phys Med Biol, 1994. 39: p. 305-320.

[12] Hudson, H.M. and R.S. Larkin, "*Accelerated image reconstruction using ordered subsets of projection data"*. IEEE Trans Med Imag, 1994. 13: p. 601-609.

[13] Fessler, J.A., "*Penalized weighted least squares image reconstruction for positron emission tomography"*. IEEE Trans Med Imag, 1994. 13: p. 290-300.

[14] D. L. Bailey, D. W. Townsend, P. E. Valk, and M. N. Maisey, editors. "*Positron Emission Tomography". Basic Sciences*. Springer-Verlag, 2005.

[15] Muehllehner, G., J.S. Karp, and S. Surti, "Design considerations for PET scanners". Q J Nucl Med, 2002. 46(1): p. 16-23.

[16] Zanzonico, P., "*Positron Emission Tomography: A Review of Basic Principles, Scanner Design and Performance, and Current Systems*," Seminars in Nuclear Medicine, Vol XXXIV, No 2 (April), 2004: pp 87-11

[17] Griffeth, L. K., "*Use of PET/CT scanning in cancer patients: technical and practical considerations*," BUMC Proceedings 2005;18:321-330.

[18] Saha, G.B., "*Basics of PET Imaging*," Physics, Chemistry, and Regulations 2010, XIV, 241 pp. Springer

[19] Bruyant, P.P., "Analytic and iterative reconstruction algorithms in SPECT," J. Nucl. Med. 2002; 43: 1343 - 1358.

[20] PE Kinahan and JG Rogers, "*Analytic 3D Image Reconstruction Using All Detected Events*" IEEE Trans. Nucl. Sci. 36(1), 1990, pp. 964-968.
[21] Defrise, M., Kinahan, P.E., Townsend, D.W., Michel, C., Sibomana, M., Newport, D.F., "*Exact and approximate rebinning algorithms for 3D-PET data*" IEEE Trans. Med. Imag. 16(2), 1997, pp. 145-158.
[22] Online Resource: https://www.dicomstandard.org
[23] Tavernier, S., "*Experimental Techniques in Nuclear and Particle Physics*," Springer 2010, IX, 306 p.
[24] Saha, G.B., "*Basics of PET Imaging. Physics, Chemistry, and Regulations*," Springer 2010, XIV, 241 p.
[25] Wagner, H.N. Jr., "*A brief history of positron emission tomography (PET)*," Semin. Nucl. Med. 1998 Jul; 28(3): pp. 213 – 220.
[26] Hutton, B.F., "*The origins of SPECT and SPECT/CT*," Eur. J. Nucl. Med. Mol. Imaging, 2014 May; 41 Suppl 1: S3 – 16.
[27] Lewellen, T.K., "*Recent developments in PET detector technology*," Phys. Med. Biol. 2008 Sep 7; 53(17); pp. 287 – 317.
[28] Lecoq, P., "*Development of new scintillators for medical applications*," Nucl. Instr. and Meth. In Phys. Res. A: Accelerators, Spectrometers, Detectors and Associated Equipment, Vol. 809, 11 Feb 2016, pp. 130 – 139.
[29] Lecoq, P., Gektin, A., Korzhik, M., "*Inorganic Scintillators for Detector Systems: Physical Properties and Crystal Engineering*," Springer, Nov 25, 2016 – Science – 408 p.
[30] Glenn F. Knoll. *"Radiation Detection and Measurement"*. Wiley, third edition, 2000.
[31] Derenzo S, Weber M, Moses W, Dujardin C. *"Measurements of the Intrinsic Rise Times of Common Inorganic Scintillators."* IEEE Trans. Nucl. Sci. 2000;47:860–864.
[32] Virginia Ch. Spanoudaki and Craig S. Levin. "*Photo-detectors for time of fight positron emission tomography (ToF-PET)"*. Sensors, 10(11): pp. 10484-10505, 2010.
[33] Charles L. Melcher. "*Scintillation crystals for PET"*. Journal of Nuclear Medicine, 41(6): pp. 1051-1055, 2000.
[34] Yand, Y., et al., "*A Prototype High-Resolution Small-Animal PET Scanner Dedicated to Mouse Brain Imaging*," J. Nucl. Med. 2016 Jul; 57(7): 1130:5.
[35] González, A. J., et al., "*Next generation of the Albira small animal PET based on high density SiPM arrays*," IEEE Nucl. Sci. Symp. Conference Record, 2015.
[36] Marcinkowski, R., Mollet, P., Van Holen, R., Vandenberghe, S., "*Sub-millimetre DOI detector based on monolithic LYSO and digital SiPM for a dedicated small-animal PET system*," Phys. Med. Biol., 2016 Mar. 7; 61(5): pp. 2196 – 2212.
[37] Nabet, B., "*Photodetectors: Materials, Devices and Applications*," Woodhead Publishing, Oct 24, 2015 – Science – 550 p.
[38] Koppens, F.H.L., et al., "*Photodetectors based on graphene, other two-dimensional material and hybrid systems*," Nat Nano 9, 2014, pp. 780 – 793.
[39] Roger Lecomte. "*Novel detector technology for clinical PET"*. European Journal of Nuclear Medicine and Molecular Imaging, 36(1): pp. 69-85, 2009. ISSN 1619-7070.
[40] Spanoudaki, Virginia Ch., and Craig S. Levin. *"Photo-Detectors for Time of Flight Positron Emission Tomography (ToF-PET)."* Sensors (Basel, Switzerland) 10.11 (2010): pp. 10484–10505.
[41] R.A. Yotter and D.M. Wilson. *"A review of photodetectors for sensing light emitting reporters in biological systems"*. Sensors Journal, IEEE, 3(3): pp. 288-303, June 2003.
[42] A. Osovizky, et al., "*Scintillation light readout using silicon photomultiplier - review and experimental results.*" In Nuclear Science Symposium Conference Record, IEEE, pp. 2482-2483, Oct 2008.
[43] Slomka, P.J., Pan, T., Germano, G., "*Recent Advances and Future Progress in PET Instrumentation,"* Semin Nucl Med, 2016 Jan; 46(1); pp. 5 – 19.
[44] Russell, J., Cohn, R., "*Avalanche Photodiode*," Book on Demand, 2012, 86 p.

[45] Foster, M.A., "*Silicon Photomultipliers in Radiation Sensing Applications*," University of Southampton, 2010.
[46] Casey, M., Burbar, Z., Rothfuss, H., Panin, V., Bharkhada, D., "*A next generation SiPM based PET/CT system with improved time and spatial resolution*," J Nucl Med, May 1, 2017 vol. 58 no. supplement 1, 1332.
[47] Huber, J.S., Moses, W.W., Andreaco, M.S., Petterson, O., "*An LSO Scintillator Array for a PET Detector Module with Depth of Interaction Measurement*", IEEE Transactions on Nuclear Science, Vol. 48-3, 2001, pp. 684 – 688.
[48] Online Resource: http://medicalphysicsweb.org/cws/article/research/41040
[49] Lee YS., et al.,"*Performance measurement of PSF modeling reconstruction (True X) on Siemens Biograph TruePoint TrueV PET/CT*," Ann. Nucl. Med. 2014 May; 28(4): 340-8.
[50] Surti, S., et al., "*Performance of Philips Gemini TF PET/CT Scanner with Special Consideration for Its Time-of-Flight Imaging Capabilities*," J. Nucl. Med. March 2007 vol. 48 no. 3, pp. 471 - 480.
[51] De Ponti, E., et al., "*Performance measurements for the PET/CT Discovery-600 using NEMA NU 2-2007 standards*," Medical Physics, 38(2): 968-74, Feb. 2011.
[52] Online Resource: https://www.crystals.saint-gobain.com
[53] Moses W.W., "*Time of flight PET revisited.*", IEEE Trans. Nuc. Sci., 2003; 50 pp. 1325-1330.
[54] Online Resource: https://www.usa.philips.com/healthcare/product/HC459800473361/time-of-flight-pet-imaging-software
[55] McKay, K. G., "*Electron-Hole Production in Germanium by Alpha-Particles*," Phys. Rev. 84, 829, Nov. 1951
[56] Tavernier S., Gektin, A., Grinyov, B., Moses, W.W., *"Radiation Detectors for Medical Applications."*, Springer Science & Business Media. 20 Jun. 2006
[57] Fano, U., *"Ionization Yield of Radiations. II. The Fluctuations of the Number of Ions"*. Physical Review, 1947, 72 (1): 26.
[58] Redus, R.H., J.A. Pantazis, A.C. Huber, V.T. Jordanov, J. Butler, B. Apotovsky, *"Fano Factor Determination for CZT*", in Material Research Society Symposium Proceedings: Semiconductors for Room- Temperature Radiation Detector Applications II, Vol 487, p.101-107, December 1997. (eds. R.B. James, et. al.)
[59] Leo, W.R. (1987). *"Techniques for Nuclear and Particle Physics Experiments: An How-to Approach."* Springer-Verlag. pp. 109–125. ISBN 3-540-17386-2.
[60] Shrestha, S., et al., *"High-performance direct conversion X-ray detectors based on sintered hybrid lead triiodide perovskite wafers."* Nature Photonics 11, 436-440 (2017)
[61] Hitomi, k., Shoji, T., Ishii, K., *"Advances in TlBr detector development,"* Journal of Crystal Growth, Volume 379, 2013, pp. 93-98.
[62] Online Resource: http://www.amptek.com
[63] Online Resource: http://www.ortec-online.com
[64] Online Resource: http://www.amscins.com
[65] Online Resource: http://www.canberra.com
[66] Harkness, L., et al., "*Semiconductor detectors for Compton imaging in nuclear medicine*," Journal of Instrumentation 2012, 7 – CO1004.
[67] Pinsky, L.S., et al., "*Preparing for the first Medipix detectors in space*," Aerospace Conference, 2012 IEEE.
[68] Morimoto, Y., et al., *"Development of a 3D brain PET scanner using CdTe semiconductor detectors and its first clinical application,"* IEEE Transactions on Nuclear Science 2011,58 (5).
[69] Vaska, P., et al., *"A prototype CZT-based PET scanner for high resolution mouse brain imaging,"* 2007 IEEE Nuclear Science Symposium Conference Record, pp. 3816-3819.

[70] XCOM: Photon Cross Sections Database. Available online at website (http://physics.nist.gov/PhysRefData/Xcom/Text/XCOM.htm) (Most recent access on January 2018)

[71] Ishii, K., et al., *"First achievement of less than 1 mm FWHM resolution in practical semiconductor animal PET scanner,"* Nucl. Instrum. Methods Phys. Res. A 576, pp. 435 – 440.

[72] Mitchell GS, Sinha S, Stickel JR, Bowen SL, Cirignano LJ, Dokhale P, Kim H, Shah K, and Cherry SR (2008) *"CdTe strip detector characterization for high resolution small animal PET."* IEEE Trans Nucl Sci 55: 870–876.

[73] Park S-J, Rogers WL and Clinthorne NH (2007) *"Design of a very high-resolution small animal PET scanner using a silicon scatter detector."* Phys Med Biol 52: 4653–4677.

[74] Boston HC, Boston AJ, Cooper RJ, Cresswell J, Grint AN, Mather AR, Nolan PJ, Scraggs DP, Turk G, Hall CJ, Lazarus I, Berry A, Beveridge T, Gillam J, and Lewis R (2007) *"Characterization of the SmartPET planar Germanium detectors."* Nucl Instrum Methods Phys Res A 579: 104–107.

[75] Auricchio, N., et al., *"Characterization of Silicon Detectors for the SiliPET Project: A Small Animal PET Scanner Based on Stacks of Silicon Detectors,"* IEEE Transactions on Nuclear Science 11/2010, 57(5-57), pp. 2424 – 2436.

[76] Del Guerra, A., Bartoli, A., Belcari, N., Herbert, D., Larobina, M., *"Performance evaluation of the fully engineered YAP-(S)PET scanner for small animal imaging,"* Nuclear Science Symposium Conference Record, 2004 IEEE, 11/2004.

[77] Schäfers, K.P., Reader, A.J., Kriens, M., Knoess, C., Schober, O., Schäfers, M., *"Performance evaluation of the 32-module quadHIDAC small-animal PET scanner,"* J. Nucl. Med. 2005 Jun; 46(6): pp. 996-1004.

[78] Weber, S., et al., *"Evaluation of the TierPET system,"* IEEE Tran. Nucl. Sci. Vol. 46(4), 1999, pp. 1177 – 1183.

[79] Sempere Roldan, P., et al., *"Raytest ClearPETTM, a new generation small animal PET scanner,"* Nucl. Inst. and Methods in Physics Research A 571 (2007), pp. 498 – 501.

[80] Wang, Y., Seide, J., Tsui, B.M.W., Vaquero, J.J., Pomper, M.G., *"Performance Evaluation of the GE Healthcare eXplore VISTA Dual-Ring Small-Animal PET Scanner,"* J. Nucl. Med. November 2006, 47, pp. 1891 – 1900.

[81] Su Kim, J., et al., *"Performance Measurement of the microPET Focus 120 Scanner,"* J. Nucl. Med. 2007; 48: pp. 1527 – 1535.

[82] Yang, Y., Tai, Y.C., Siegel, S., Newport, D.F., Bai, B., Li, Q., Leahy, R.M., Cherry, S.R., *"Optimization and performance evaluation of the microPET II scanner for in vivo small-animal imaging,"* Phys. Med. Biol. 2004 June 21; 49(12): pp. 2527 – 2545.

[83] Chmeissani, M., Arce, P., Cañadas, M., "*Modeling and Simulation of PET scanner Based on Pixelated Solid-State Detector*," 2009 IEEE Nucl. Sci. Symp. Conf. Record, pp. 3496 – 3502.

[84] Arlt, R., Rundquist, D.E., "*Room temperature semiconductor detectors for safeguards measurements*," Nuclear Instruments and Methods in Physics Research Section A Accelerators Spectrometers Detectors and Associated Equipment, Oct 1996, 380(1):455 – 461.

[85] Cherry, S.R., Sorenson, J.A., Phelps, M.E., "*Interaction of Radiation with Matter, In Physics in Nuclear Medicine (Fourth Edition), - Chapter 6*," W.B. Saunders, Philadelphia, 2012, Pages 63-85.

[86] Arce, P., et al., "*GAMOS: A framework to do Geant4 simulations in different physics fields with an user-friendly interface*,", Nucl. Inst. Meth. Phys. Res. A. 2013.

[87] Nat. Electr. Manufact. Assoc. "*Performance measurements of positron emission tomographs*," NEMA Standards Pub. NU 2-2001.

[88] Nat. Electr. Manufact. Assoc. "*Performance measurements for small animal positron emission tomographs*," NEMA Standards Pub. NU 4-2008.

[89] Arino, G., Chmeissani, M., Puigdengoles, C., De Lorenzo, G., Diener, R., Arce, P., Cabruja, E., Calderon, Y., Canadas, M., Kolstein, M., Macias-Montero, J.G., Martinez, R., Mikhaylova, E., Ozsahin, I., Uzun, D., "*Characterization of CdTe detector for use in PET*," IEEE Nucl. Sci. Symp. Conf. Rec., 2011, pp. 4598 – 4603.

[90] Ariño, G., Chmeissani, M., De Lorenzo, G., Puigdengoles, C., Cabruja, E., Calderon, Y., Kolstein, M., Macias-Montero, J.G., Martinez, R., Mikhaylova, E., Uzun, D., "*Energy and coincidence time resolution measurements of CdTe detectors for PET*," Journal of Instrumentation, Feb 2013, Vol. 8.

[91] Kolstein, M., Chmeissani, M., "*Using Compton scattering for random coincidence rejection*," Journal of Instrumentation, Dec. 2016, Vol. 11(12), pp. C12017.

[92] de Jong, H.W., van Velden, F.H., Kloet, R.W., Buijs, F.L., Boellaard, R., Lammertsma, A.A., "*Performance evaluation of the ECAT HRRT: An LSO-LYSO double layer high resolution, high sensitivity scanner*," Phys. Med. Biol.2007; 52: 1505.

[93] Takahashi, T., Paul, B., Hirose, K., Matsumoto, C., Ohno, R., Ozaki, T., Mori, K., Tomita, Y., "*High-resolution Schottky CdTe diode for hard X-ray and gamma-ray astronomy*," Nucl. Instr. Meth., vol. A436, pp. 111 – 119, 1999.

[94] Artl, R., Ivanov, V., Khusainov, A., "*Advances in High-Resolution CdTe and Large Volume CdZnTe Detectors*," Proc. SPIE, vol. 3115, pp. 76 – 89, 1994.

[95] Niraula, M., Mochizuki, D., Aoki, T., Hatanaka, Y., Tomita, Y., Nihashi, T., "*Improved spectrometric perfomance of CdTe radiation detectors in a p-i-n design*," Appl. Phys. Lett., vol. 75, 15, pp. 2322 – 2324, 1999.

[96] Online webpage: http://www.acrorad.com

[97] Serreze, H.B., Entine, G., Bell, R.O., Wald, F.V., "*Advances in CdTe Gamma-ray Detectors*," IEEE Trans. Nucl. Sci., vol. 21, pp. 404 – 406, 1974.

[98] Bell, R.O., Entine, G., Serreze, H.B., "*Time-dependent Polarization of CdTe Gamma-ray Detectors*," Nucl. Instr. And Meth., 117, pp. 267 – 271, 1974.

[99] Malm, H.L., Martini, M., "*Polarization Phenomena in CdTe Nuclear Radiation Detectors*," IEEE Trans. Nucl. Sci., vol. 21, pp. 322 – 330, 1974

[100] Lachish, U., "*Driving spectral resolution to the noise limit in semiconductor gamma detector arrays*,", IEEE Trans. Nucl. Sci. 2001, 48(3), pp. 520 – 523.

[101] Uxa, S., Grill, R., Belas, E., *"Evaluation of the mobility-lifetime product in CdTe and CdZnTe detectors by the transient-current technique,"* Journal of Applied Physics 114, 094511 (2013).

[102] E. Gaubas, T. Ceponis, J. Pavlov, A. Baskevicius. *"Profiling of the injected charge drift current transients by cross-sectional scanning technique."* Journal of Applied Physics 115:5, 054509 (2014).

[103] Yunpeng Ling, Jiahua Min, Xiaoyan Liang, Jijun Zhang, Liuqing Yang, Ying Zhang, Ming Li, Zhaoxin Liu, Linjun Wang. *"Carrier transport performance of Cd0.9Zn0.1Te detector by direct current photoconductive technology."* Journal of Applied Physics 121:3, 034502 (2017).

[104] A. Musiienko, R. Grill, J. Pekárek, E. Belas, P. Praus, J. Pipek, V. Dědič, H. Elhadidy. *"Characterization of polarizing semiconductor radiation detectors by laser-induced transient currents."* Applied Physics Letters 111:8, 082103, (2017).

[105] Suzuki, K., Seto, S., Sawada, T., Imai, K., "*Carrier Transport Properties of HPB CdZnTe and THM CdTe:C1*," IEEE Trans. Nucl. Sci., Vol. 49, No. 3, June 2002, pp. 1287 – 1291.

[106] Niraula, M., et al., "*Characterization of CdTe/n+-Si Heterojunction Diodes for Nuclear Radiation Detectors*," IEEE Trans. Nucl. Sci., Vol. 54-4, Aug. 2007, pp. 817 – 820.

[107] Kolstein, M., Arino-Estrada, G., Chmeissani, M., De Lorenzo, G., "*Simulation of charge transport in pixelated CdTe*," Journal of Instrumentation, Vol. 9, C12027.

[108] Del Sordo, S., Abbene, L., Caroli, E., Mancini, A.M., Zappettini, A., Ubertini, P., "*Progress in the Development of CdTe and CdZnTe Semiconductor Radiation Detectors for Astrophysical and Medical Applications*," Sensors 2009, 9, pp. 3491 – 3526.

[109] Arino-Estrada, G., et al, "*Characterization of CdTe detector for use in PET*," IEEE Nuc. Sci. Symp. Conf. Record, 2011.
[110] Arino-Estrada, G., et al., "*Characterization of a module with pixelated CdTe detectors for possible PET, PEM, and a Compton camera applications*," Journal of Instr., Vol. 9, May 2014.
[111] Giboni, K.L., et al., "*Coincidence timing of Schottky CdTe detectors for tomographic imaging*," Nucl. Instrum. Meth. A. 2000; 450:307.
[112] Baldazzi, G., et al., "*A radiation detection system for high-energy computerized tomography using CdZnTe detector*,", IEEE Trans. Nucl. Sci. 1995; 42:575.
[113] Eisen, Y., et al., "*CdTe and CdZnTe gamma ray detector for medical and industrial imaging system*," Nucl. Instrum. Meth. A. 1999; 428:158.
[114] Scheiber, C., "*CdTe and CdZnTe detectors in nuclear medicine*," Nucl. Instrum. Meth. A. 2000; 448:513.
[115] Bertulocci, E., et al., "*Timing properties of CdZnTe detectors for positron emission tomography*," Nucl. Instrum. Meth. 1997; 400:107
[116] Barber, H.B., "*Applications of semiconductor detectors to nuclear medicine*," Nucl. Instrum. Meth. A. 1999; 436:102.
[117] Online Resource: http://www.amptek.com
[118] Spieler, H., "*Semiconductor Detector Systems*," OUP Oxford, Aug 25, 2005.
[119] Shao, Y., et al., "*Measurement of coincidence timing resolution with CdTe detectors*," Proc. SPIE, 2000, 4142:254
[120] Amrami, R., et al., "*Timing performance of pixelated CdZnTe detectors*," Nucl. Instrum. Meth. A. 2001; 458:772.
[121] Okada, Y., et al., "*CdTe and CdZnTe detectors for timing measurements*," IEEE Trans. Nucl. Sci. 2002; 4:2429.
[122] Online Resource: http://medipix.web.cern.ch
[123] Pangaud, P., et al., "*XPAD3-S: A fast hybrid pixel readout chip for X-ray synchrotron facilities*," Nuclear Instruments and Methods in Physics Research Section A Accelerators Spectrometers Detectors and Associated Equipment June 2008, 591(1): pp. 159 – 162.
[124] Loeliger, T., Bronnimann, C., Donath, T., Schneebeli, M., Schnyder, R., Trub, P., "*The New PILATUS3 ASIC with Instant Retrigger Capability*," IEEE Proceedings of the Nuclear Science Symposium and Medical Imaging Conference (NSS/MIC), 2012, pp. 610 – 615.
[125] Online Resource: https://www.psi.ch/detectors/detectors-group
[126] Steadman, R., Herrmann, C., Livne, A., "*ChromAIX2: A large area, high count-rate energy-resolving photon counting ASIC for a Spectral CT Prototype*," Nuclear Instruments and Methods in Physics Research Section A: Accelerators, Spectrometers, Detectors and Associated Equipment, Volume 862, 2017, pp. 18-24.
[127] Macias-Montero, J.G., et al., "*ERICA: an energy resolving photon counting readout ASIC for X-ray in-line cameras*," Journal of Instrumentation, Volume 11, Issue 12, pp. C12027 (2016)
[128] Online Resource: http://ideas.no/ideas-ic-products/
[129] Jones, L., et al., "*HEXITED ASIC – a pixelated readout chip for CZT detectors*," Nuclear Instruments and Methods in Physics Research A 604 (2009) 34 – 37.
[130] Aad, G., et al., "*ATLAS pixel detector electronics and sensors*," Journal of Instrumentation, Volume 3, July 2008 P07007.
[131] Lugiez, F., et al., "*IDeF-X V1.1: Performances of a New CMOS 16 Channels Analogue Readout ASIC for Cd(Zn)Te detectors*," Proc. IEEE NSS-MIC conf. rec. 2006, pp. 841 – 844.
[132] Meuris, A., et al., "*Micro hard-X ray camera: from Caliste 64 to Caliste 256*," IEEE Transactions on Nuclear Science, 2009, Vol. 56, Issue 4, Part:1, pp. 1835 – 1841.
[133] Ahmad, S., et al., "*Triroc: A Multi-Channel SiPM Read-Out ASIC for PET/PET-ToF Application*," IEEE Transactions on Nuclear Science, Vol. 62, No. 3, June 2015, pp. 664 – 668.

[134] Di Francesco, A., et al., "*TOFPET2: a high-performance ASIC for time and amplitude measurements of SiPM signals in time-of-flight applications*," 2016 Journal of Instrumentation, Volume 11, C03042.
[135] Fleury, J., et al., "*Petiroc and Citiroc: front-end ASICs for SiPM read-out and ToF applications*," Journal of Instrumentation, Volume 9, January 2014.
[136] Ballabriga, R., et al., "*Review of hybrid pixel detector readout ASICs for spectroscopic X-ray imaging*," Journal of Instrumentation, Volume 11, P01007.
[137] Shiraki, H., et al., "*Improvement of the productivity in the THM growth of CdTe single crystal as nuclear radiation detectors*," IEEE Transactions on Nuclear Science (2009), 56, pp. 1717 – 1723.
[138] Turchetta, R., "*Analog Electronics for Radiation Detection*," CRC Press, Dec 21, 2017 – Technology & Engineering – 290 pp.
[139] Linhart, V., et al., "*Spectroscopy study of imaging devices based on silicon Pixel Array Detector coupled to VATAGP7 read-out chips*," Journal of Instrumentation 6, 2010, C01092.
[140] Atkin, E., Levin, V., Malankin, E., Shumikhin, V., "*Development of a low-noise readout ASIC for Silicon Drift Detectors in high energy resolution X-ray spectrometry*," Journal of Instrumentation, Volume 12, March 2017.
[141] Henzler, S., "*Time-to-Digital Converters*," Springer Series in Advanced Microelectronics 29, 2010. Chapter 2.
[142] Ariño-Estrada, G., et al., "*Characterization of a module with pixelated CdTe detectors for possible PET, PEM, and Compton camera applications*," Journal of Instrumentation, Volume 9, 2014.
[143] Kolstein, M., Chmeissani, M., "*Using triple gamma coincidences with a pixelated semiconductor Compton-PET scanner: a simulation study*," Journal of Instrumentation, Volume 11, January 2016.
[144] Calderon, Y., Chmeissani, M., Kolstein, M., De Lorenzo, G., "*Evaluation of Compton gamma camera prototype based on pixelated CdTe detectors*," Journal of Instrumentation, Volume 9, 2014.
[145] Kolstein, M., Chmeissani, M., "*Simulation of Positron Emission Mammography Imaging with Pixelated Cdte*," Springer International Publishing - Proceedings IWDM 13th international workshop, 2016.
[146] Online Resource: https://www.mosis.com/vendors/view/tsmc/025
[147] MacDonald, L., et al., "*Clinical imaging characteristics of the positron emission mammography camera: PEM Flex Solo II*," J. Nucl. Med. 50 1666, 2009.
[148] Mikhaylova, E.,, et al., "*Simulation of the Expected Performance of a Seamless Scanner for Brain PET Based on Highly Pixelated CdTe Detectors*," IEEE Transaction on Medical Imaging, vol. 33, No. 2, February 2014, pp. 332 – 339.
[149] Arino-Estrada, G., "*Characterization of a pixel CdTe detector for nuclear medicine imaging*," Ph.D. Thesis, 2015, http://catalegclassic.uab.cat/record=b1947677~S1*cat
[150] Chmeissani, M., et al., "*First results of a highly granulated 3D CdTe detector module for PET*," Phys. Med. Biol. 63, 2018, 025032.
[151] Ariño-Estrada, G., "*Characterization of a Pixel CdTe Detector for Nuclear Medicine Imaging*," Ph.D. Thesis, UAB, April 2015.
[152] Macias-Montero, J.G., et al.,"*Toward VIP-PIX: A Low Noise Readout ASIC for Pixelated CdTe Gamma-Ray Detectors for Use in the Next Generation of PET Scanners*," IEEE Trans. Nucl. Sci. Vol. 60, No. 4, Aug. 2013, pp. 2898 – 2904.

Appendix

Collection of papers

Title: Simulation of the Expected Performance of a Seamless Scanner for Brain PET Based on Highly Pixelated CdTe Detectors

Authors: Ekaterina Mikhayolva[1], Gianluca De Lorenzo[1], Mokhtar Chmeissani[1], Machiel Kolstein[1], Mario Cañadas[2], Pedro Arce[2], Yonatan Calderón[1], Dilber Uzun[1], Gerard Ariño[1], José Gabriel Macías Montero[1], Ricardo Martínez[3], Carles Puigdengoles[1], Enric Cabruja[3].

[1] Institut de Física d'Altes Energies (IFAE)
[2] Centro de Investigaciones Energéticas, Medioambientales y Tecnológicas (CIEMAT)
[3] Institut de Microelectrònica de Barcelona – Centre Nacional de Microelectrònica (IMB-CNM (CSIC))

Journal: IEEE Transactions on Medical Imaging, Vol.33, No 2
Date: February 2014
DOI: 10.1109/TMI.2013.2284657

Title: Energy and coincidence time resolution measurements of CdTe detectors for PET

Authors: Gerard Ariño[1], Mokhtar Chmeissani[1], Gianluca De Lorenzo[1], Carles Puigdengoles[1], Yonatan Calderón[1], Machiel Kolstein[1], José Gabriel Macías Montero[1], Ricardo Martínez[2], Ekaterina Mikhayolva[1], Dilber Uzun[1].

[1] Institut de Física d'Altes Energies (IFAE)
[2] Institut de Microelectrònica de Barcelona – Centre Nacional de Microelectrònica (IMB-CNM (CSIC))

Journal: Journal of Instrumentation
Date: February 2013
DOI: 10.1088/1748-0221/8/02/C02015

Title: Toward VIP-PIX: A Low Noise Readout ASIC for Pixelated CdTe Gamma-Ray Detectors for Use in the Next Generation of PET Scanners

Authors: José Gabriel Macías Montero[1], Maher Sarraj[2], Mokhtar Chmeissani[1], Carles Puigdengoles[1], Gianluca De Lorenzo[1], Ricardo Martínez[3].

[1] Institut de Física d'Altes Energies (IFAE)
[2] Texas Instruments Incorporated (Dallas, TX, USA)
[3] Institut de Microelectrònica de Barcelona – Centre Nacional de Microelectrònica (IMB-CNM (CSIC))

Journal: IEEE Transactions on Nuclear Science, Vol.60, No 4
Date: August 2013
DOI: 10.1109/TNS.2013.2270115

Title: A 2D 4x4 Channel Readout ASIC for Pixelated CdTe Detectors for Medical Imaging Applications

Authors: José Gabriel Macías Montero[1], Maher Sarraj[2], Mokhtar Chmeissani[1], Ricardo Martínez[3], Carles Puigdengoles[1].

[1] Institut de Física d'Altes Energies (IFAE)
[2] Texas Instruments Incorporated (Dallas, TX, USA)
[3] Institut de Microelectrònica de Barcelona – Centre Nacional de Microelectrònica (IMB-CNM (CSIC))

Journal: IEEE Transactions on Nuclear Science, Vol.62, No 5
Date: October 2015
DOI: 10.1109/TNS.2015.2465377

Title: Firsts results of a highly granulated 3D CdTe detector module for PET

Authors: Mokhtar Chmeissani[1], Machiel Kolstein[1], José Gabriel Macías Montero[1], Carles Puigdengoles[1], Jorge García[1], Xavier Prats[1], Ricardo Martínez[3],

[1] Institut de Física d'Altes Energies (IFAE)
[2] Institut de Microelectrònica de Barcelona – Centre Nacional de Microelectrònica (IMB-CNM (CSIC))

Journal: Physics in Medicine & Biology, Vol.63
Date: January 2018
DOI: 10.1088/1361-6560/aaa44c

In this thesis, an application specific integrated circuit (ASIC) to readout high-density and highly-granulated Cadmium Telluride detector for a novel PET scanner design is presented. The research presented here was realized within the framework of *Voxel Imaging PET pathfinder* ERC project to develop detector modules for PET applications. The VIP PET scanner is based on the stacking of CdTe detectors pixelated into arrays of 10 x 10 voxels of 1 mm x 1 mm x 2 mm size connected to pixelated readout ASICs. More than 6 million voxels provide independently the energy and the time stamp of every photon interaction. The architecture of the VIPPIX ASIC is based on an array of 10 x 10 independent pixels connected to a global controller and to a time to digital converter (TDC). Every pixel electronics includes a preamplifier with detector's leakage compensation, a pulse shaper, a peak-and-detect circuit, a 10-bit analog-to-digital converter, a discriminator, and a local digital controller. The measured equivalent noise charge of the pixels is 150 e- RMS and the resolution of the TDC is 600 ps FWHM. Connected to the CdTe pixelated detectors, the performance of approximately 18000 pixels shows an energy resolution of 2.2 % FWHM for 511 keV photopeak at -250 V/mm detector bias and room temperature. The new PET design based on pixelated CdTe detectors using VIPPIX readout ASICs has been successfully fabricated, and is ready for image acquisition.

UNIVERSITAT DE BARCELONA